

Alma Mater Studiorum – Università di Bologna

DOTTORATO DI RICERCA IN

Ingegneria Civile, Chimica, Ambientale e dei Materiali

Ciclo XXX

Settore Concorsuale: 08/B2

Settore Scientifico Disciplinare: ICAR/08

HOMOGENIZATION OF NONLINEAR COMPOSITES FOR MULTISCALE
ANALYSIS

Presentata da: Federica Covezzi

Coordinatore Dottorato

Supervisore

Prof. Luca Vittuari

Prof. Stefano de Miranda

Esame finale anno 2018

To Alessandra.
What I achieve is what we achieve.
Together, always.

ABSTRACT

A composite is a material made out of two or more constituents (phases) combined together in order to achieve desirable mechanical or thermal properties. Such innovative materials have been widely used in a large variety of engineering fields in the past decades. The design of a composite structure requires the resolution of a multiscale problem that involves a macroscale (i.e. the structural scale) and a microscale. The latter plays a crucial role in the determination of the material behavior at the macroscale, especially when dealing with constituents characterized by nonlinearities. For this reason, numerical tools are required in order to design composite structures by taking into account of their microstructure. These tools need to provide an accurate yet efficient solution in terms of time and memory requirements, due to the large number of internal variables of the problem. This issue is addressed by different methods that overcome this problem by reducing the number of internal variables. Within this framework, this thesis focuses on the development of a new homogenization technique named Mixed TFA (MxTFA) in order to solve the homogenization problem for nonlinear composites. This technique is based on a mixed-stress variational approach involving self-equilibrated stresses and plastic multiplier as independent variables on the Reference Volume Element (RVE). The MxTFA is developed for the case of elastoplasticity and viscoplasticity, and it is implemented into a multiscale analysis for nonlinear composites. Numerical results show the efficiency of the presented techniques, both at microscale and at macroscale level.

PUBLICATIONS

Some ideas and figures have appeared previously in the following publications:

- (i) Covezzi, F. and de Miranda, S. and Marfia, S. and Sacco, E., "Complementary formulation of the TFA for the elasto-plastic analysis of composites". *Composite Structures* 156 (2016), pp. 93-100, DOI: <http://dx.doi.org/10.1016/j.compstruct.2016.01.094>.
- (ii) Covezzi, F. and de Miranda, S. and Marfia, S. and Sacco, E., "A homogenization technique for elasto-plastic composites". *EC-COMAS Congress 2016 - Proceedings of the 7th European Congress on Computational Methods in Applied Sciences and Engineering 2* (2016), pp. 2316-2322, DOI: [10.7712/100016.1961.11479](http://dx.doi.org/10.7712/100016.1961.11479).
- (iii) Covezzi, F. and de Miranda, S. and Marfia, S. and Sacco, E., "Homogenization of elastic-viscoplastic composites by the Mixed TFA". *Comp. Meth. in Appl. Mech. and Eng.* 318 (2017), pp. 701-723, DOI: <http://dx.doi.org/10.1016/j.cma.2017.02.009>.
- (iv) Covezzi, F. and de Miranda, S. and Fritzen, F. and Marfia, S. and Sacco, E., "Comparison of reduced order homogenization techniques: pRBMOR, NUTFA and MxTFA". *Meccanica* In press (2018).
- (v) Covezzi, F. and de Miranda, S. and Marfia, S. and Sacco, E., "Multiscale analysis of nonlinear composites via a mixed reduced order formulation". *Composite Structures* Submitted (2018).

ACKNOWLEDGEMENTS

Firstly, I would like to express my gratitude to my advisor Prof. Stefano de Miranda for the continuous support, for his patience and trust in me. My sincere thanks also goes to my co-advisors Prof. Elio Sacco and Prof. Sonia Marfia: their expertise and advices were very valuable to my research.

I also thank Dr. Felix Fritzen, who provided me the opportunity to join his research group as visiting PhD student, for the stimulating discussions.

A sincere thanks goes to my LAMC mates for all the fun and the support we have had in the last four years.

Last but not the least, I would like to thank my family and Federico for supporting me throughout these years.

CONTENTS

1	INTRODUCTION	1
2	MULTISCALE PROBLEMS: GENERAL CONSIDERATIONS	5
2.1	Multiscale problem	5
2.2	Micromechanical problem	7
2.3	Homogenization problem	8
2.4	Transformation Field Analysis	14
2.4.1	Local and overall fields	15
2.4.2	Pre-analyses	16
2.4.3	Evolution problem	16
3	MIXED TRANSFORMATION FIELD ANALYSIS (MXTFA)	17
3.1	Main idea	17
3.1.1	Numerical procedure	21
3.2	MxTFA in Elasto-plasticity	23
3.2.1	Homogenization in elasto-plasticity	23
3.2.2	Computational homogenization technique	25
3.2.3	Numerical Results	27
3.3	MxTFA in Viscoplasticity	37
3.3.1	Elastic-viscoplastic constitutive model	37
3.3.2	Computational homogenization technique	39
3.3.3	Numerical procedure	40
3.3.4	Numerical results	40
4	COMPARISON BETWEEN NTFA-BASED MODEL ORDER REDUCTION TECHNIQUES	55
4.1	Comparison criteria	55
4.2	The pRBMOR	56
4.2.1	Mode selection	56
4.2.2	Pre-analyses	57
4.2.3	Evolution of reduced degrees of freedom	57
4.2.4	Effective stress computation	59
4.3	The NUTFA	59
4.3.1	Mode selection	59
4.3.2	Pre-analyses	60
4.3.3	Evolution of reduced degrees of freedom	60
4.3.4	Effective stress computation	61
4.4	The MxTFA	62
4.4.1	Mode selection	62
4.4.2	Effective stress computation	63
4.5	Comparison: inelastic modes of pRBMOR, NUTFA and MxTFA	63
4.6	Numerical Applications	65
4.6.1	Ceramic inclusion in viscoplastic matrix	67
5	MULTISCALE ANALYSIS VIA MXTFA	77

5.1	Microscale: MxTFA	77
5.1.1	Algorithmic tangent stiffness	77
5.2	Multiscale procedure	78
5.3	Numerical Results	79
5.3.1	UC analysis	80
5.3.2	Multiscale analysis	84
6	SUMMARY AND CONCLUSIONS	95
	 BIBLIOGRAPHY	 99

LIST OF FIGURES

Figure 1	Multiscale problem.	6
Figure 2	Homogenization methods: classification.	9
Figure 3	Comparison of effective Young's modulus for different methods as function of the volume fraction c - (a) $E_1 = 420\text{GPa}$, (b) $E_1 = 1050\text{GPa}$, (c) $E_1 = 2100\text{GPa}$	12
Figure 4	Prediction of the effective Young's modulus for different concentrations c and different stiffness ratios E_I/E_M	13
Figure 5	Schematic diagram of the FE^2 model.	14
Figure 6	TFA - Pre-analyses (Offline phase).	16
Figure 7	MxTFA: RVE partitioning into subsets.	18
Figure 8	MxTFA: Graphical representation of the procedure.	23
Figure 9	Test 1 - (a) Geometry of the UC, (b) UC FE discretization.	29
Figure 10	Test 1 - Subset subdivision: (a) 4 subsets, (b) 6 subsets, (c) 8 subsets.	29
Figure 11	Test 1 - Mechanical response of the UC subjected to uniaxial loading.	30
Figure 12	Test 1 - Mechanical response of the UC subjected to biaxial loading: (a) mechanical response in x_1 -direction, (b) mechanical response in x_2 -direction.	32
Figure 13	Test 2 - Geometry of the UC (a) and subset discretization (b)	33
Figure 14	Test 2 - Mechanical response of the UC subjected to uniaxial loading.	33
Figure 15	Test 2 - Mechanical response of the UC subjected to biaxial loading.	34
Figure 16	Test 2 - Subsets configurations.	35
Figure 17	Test 2 - $\bar{\sigma}_{22}$ for the homogenization analyses.	36
Figure 18	Test 2 - Error convergence.	36
Figure 19	Test 1 - Mechanical response of the UC subjected to uniaxial loading: (a) $\epsilon = 1$ Perić, (b) $\epsilon = 0.1$ Perić, (c) $\epsilon = 0.1$ Perzyna.	43
Figure 20	Test 1- Comparison between strain maps coming from FEA and MxTFA.	45
Figure 21	Test 1- Average stress evaluation using different approaches.	46
Figure 22	Test 2 - Problem geometry.	47

Figure 23	Test 2 - (a) Finite element mesh for reference solution and pre-analyses, (b) Subset discretization.	47
Figure 24	Test 2 - Mechanical response of the UC subjected to uniaxial loading.	48
Figure 25	Test 2 - Mechanical response of the UC and the two phases subjected to uniaxial loading ($\epsilon = 0.2$).	49
Figure 26	Test 2 - Contour maps of stress [GPa] for $\epsilon = 0.2$	50
Figure 27	Test 2 - Contour maps of inelastic strain for $\epsilon = 0.2$	51
Figure 28	Test 2 - Local error maps of the stress [GPa] and inelastic strain, $\epsilon = 0.2$	52
Figure 29	Test 2 - Strain distribution.	52
Figure 30	Test 2 - Mechanical response of the UC subjected to a uniaxial loading history.	53
Figure 31	Test 2 - Mechanical response of the UC subjected to a bi-axial loading history: (a) mechanical response in x_1 -direction; (b) mechanical response in x_2 -direction.	53
Figure 32	pRBMOR- Pre analyses.	57
Figure 33	Inclusion matrix material - (a) RVE, (b) norm of the first plastic strain mode (c) stress components 22 and 33 of the induced self-equilibrated stress field for the example of Section 4.6.	58
Figure 34	NUTFA- Pre analyses.	61
Figure 35	Unit cell made of elastic inclusion and plastic matrix (one eighth): (a) FE discretization; (b) NUTFA subset partitioning; (c) MxTFA subset partitioning.	67
Figure 36	Load case 1: Comparison of the results between the FE and the model order reduction methods (pRBMOR, NUTFA and MxTFA) in terms of effective response (left) and corresponding deviator (right)	70
Figure 37	Load case 2: Comparison of the results between the FE and the model order reduction methods (pRBMOR, NUTFA and MxTFA) in terms of effective response (left) and corresponding deviatoric components (right)	72
Figure 38	Load case 3 - Comparison of the results between the FE and the model order reduction methods (pRBMOR and MxTFA) in terms of effective response.	73

Figure 39	Load case 3 - Local distribution of stress component σ_{11} [MPa] at $t = 2s$: (a) FEA, (b) MxTFA and (c) pRB MOR.	73
Figure 40	Load case 3 - Local distribution of stress component σ_{12} [MPa] at $t = 2s$: (a) FEA, (b) MxTFA and (c) pRB MOR	74
Figure 41	Load case 3 - Local distribution of inelastic strain component π_{11} at $t = 2s$: (a) FEA, (b) MxTFA and (c) pRB MOR	74
Figure 42	Load case 3 - Local distribution of inelastic strain component π_{12} at $t = 2s$: (a) FEA, (b) MxTFA and (c) pRB MOR	75
Figure 43	Load case 4: Comparison of the normal components between the FE and the model order reduction methods (pRB MOR and MxTFA) in terms of effective response (left) and corresponding deviatoric part (right).	76
Figure 44	Load case 4: Comparison of the shear components between the FE and the model order reduction methods (pRB MOR and MxTFA).	76
Figure 45	Multiscale Procedure: Graphical representation of the Online phase.	79
Figure 46	Microstructure A - Geometry and subset partitioning.	80
Figure 47	Microstructure B - Geometry and subset partitioning.	81
Figure 48	Stress prediction - (a) Microstructure A: $\bar{\sigma}_{11}$ [GPa], (b) Microstructure A: $\bar{\sigma}_{22}$ [GPa], (c) Microstructure B: $\bar{\sigma}_{11}$ [GPa], (d) Microstructure B: $\bar{\sigma}_{22}$ [GPa].	82
Figure 49	UC analysis - Mechanical response under loading/unloading of Table 23: (a) Microstructure A, (b) Microstructure B.	83
Figure 50	Square tube.	85
Figure 51	Square tube - (a) Problem geometry, (b) MS structural discretization.	85
Figure 52	Square tube - Load/displacement curve.	86
Figure 53	Square tube - Rate dependency: comparison between loading at different rates $\dot{q}_1 = 1.28$ and $\dot{q}_2 = 0.64$ [kN/mm s].	86
Figure 54	Square tube - Equivalent Stress [GPa]: (a) Load Step A ($q = 0.32$ kN/mm loading phase), (b) Load Step B ($q = 0.64$ kN/mm), (c) Load Step C ($q = 0.32$ kN/mm unloading phase).	87

Figure 55	Square tube - Equivalent plastic strain : (a) Load Step A ($q = 0.32$ kN/mm loading phase), (b) Load Step B ($q = 0.64$ kN/mm), (c) Load Step C ($q = 0.32$ kN/mm unloading phase).	87
Figure 56	Perforated plate - (a) Problem geometry, (b) Structural discretization.	90
Figure 57	Perforated plate - force/displacement curve.	90
Figure 58	Perforated plate - Stress Components of the 4 integration points (intp) for Element 1: (a) $\bar{\sigma}_{11}$, (b) $\bar{\sigma}_{22}$, (c) $\bar{\sigma}_{12}$	91
Figure 59	Perforated plate - Stress Components of the 4 integration points (intp) for Element 121: (a) $\bar{\sigma}_{11}$, (b) $\bar{\sigma}_{22}$, (c) $\bar{\sigma}_{12}$	92
Figure 60	Perforated plate - Load Step A ($\bar{u}^* = 0.1$ mm): Macro equivalent stress [MPa] and Micro stresses $\sigma^* = \sigma/Q_A$	93
Figure 61	Perforated plate - Load Step B ($\bar{u}^* = 0.2$ mm): Macro equivalent stress [MPa] and Micro stresses $\sigma^* = \sigma/Q_B$	93
Figure 62	Perforated plate - Load Step A ($\bar{u}^* = 0.1$ mm): Micro - Macro Inelastic Strain.	94
Figure 63	Perforated plate - Load Step B ($\bar{u}^* = 0.2$ mm): Micro - Macro Inelastic Strain.	94

LIST OF TABLES

Table 1	Test 1 - Material properties of the constituents.	29
Table 2	Test 1 - Uniaxial loading: final value of the average stress.	30
Table 3	Test 1 - Biaxial loading: final value of the average stresses in x_1 - and x_2 -direction.	31
Table 4	Material properties of the constituents.	31
Table 5	Uniaxial loading: final value of the average stress.	34
Table 6	Test 2 - Biaxial loading: final value of the average stress.	34
Table 7	Test 2 - Homogenization analyses: final value of the average stress.	35
Table 8	Test 1 - Material properties of the constituents.	41
Table 9	Test 1 - Final value of the average stress $\bar{\sigma}_{11}$ [MPa] for uniaxial loading condition; (a) $\epsilon = 1$ Perić model, (b) $\epsilon = 0.1$ Perić model, (c) $\epsilon = 0.1$ Perzyna model.	44
Table 10	Test 2 - Material properties for the constituents.	47
Table 11	Test 2 - Final value of the average stress $\bar{\sigma}_{22}$ [GPa] for uniaxial loading condition.	48
Table 12	Test 2 - Loading history along x_1 - axis.	50
Table 13	Test 2 - Biaxial loading history.	51
Table 14	Schematic comparison of the three methods.	66
Table 15	Pros and Cons in the offline and online phase.	66
Table 16	Material properties of the constituents.	67
Table 17	Load case 1 (LC-1) (data cf. [30], LC-2 for the 3D UC).	70
Table 18	Load case 2 (LC-2) (data cf. [30], LC-3 for the 3D UC).	71
Table 19	Load case 3 (LC-3).	72
Table 20	Load case 4 (LC-4).	75
Table 21	Microstructure A - Material properties for the constituents.	80
Table 22	Microstructure B - Material properties for the constituents.	81
Table 23	Load case for Microstructure A and B.	82
Table 24	Properties of the micromechanical finite element discretization (Nonlinear Finite Element structural Analysis (NFEA)).	85

ACRONYMS

FE	Finite Elements
FEA	Finite Element Analysis
FEAP	Finite Element Analysis Program
GSM	Generalized Standard Materials
MxTFA	Mixed TFA
NFEA	Nonlinear Finite Element structural Analysis
NTFA	Nonuniform TFA
NUTFA	New Nonuniform TFA
pRB MOR	potential Reduced Basis Model Order Reduction
PWUTFA	Piecewise Uniform TFA
POD	Proper Orthogonal Decomposition
ROM	Reduced Order Model
ROMs	Reduced Order Models
RVE	Reference Volume Element
SVE	Statistical Volume Element
TFA	Transformation Field Analysis
LH	Linear Hardening
LIN	linear
QUAD	quadratic
LC	Load Case
UC	Unit Cell

INTRODUCTION

In the last decades, the use of composite materials has widely increased in many engineering applications. A composite is a material made out of two or more constituents (phases) combined together in order to achieve desirable mechanical or thermal properties. These materials are valued in many industrial fields, where properties such as the weight to strength ratio are often the driving force. The mechanical analysis of composite structures during the design process requires the resolution of a multiscale problem: while at the design scale (or macroscale) the material is considered as homogeneous, at the microscale it is characterized by a heterogeneous microstructure that significantly affects the behavior of the material at the macroscale. For this reason, a deep understanding of the micromechanical problem can help to improve the efficiency of these materials. The prediction of the structural response of a linear (thermo-) elastic heterogeneous material is well understood, but this is often not sufficient. In fact, the behavior of the constituents can be highly nonlinear: they can be characterized by nonlinear effects such as damage, fracture, plasticity and viscosity. In particular, composites with metal [2] or polymer [32] matrices show significant viscoplastic effects that cannot be neglected.

These phenomena need to be properly modeled in order to accurately describe the response of the material at the microscale, since it will also affect the nonlinearities occurring at the macroscale. This leads to the need of reliable design tools that are able to predict the overall behavior of the material at the macroscale by accounting also for its microstructure. When employing a nonlinear FEA in the analysis of composite structures, a discretization at least as fine as the size of the heterogeneities is required. This path cannot be pursued because of memory space and CPU time requirements. One can then follow two approaches:

- **Phenomenological approach:** is used to obtain a constitutive law for the material from experimental observation. The main advantage is that these models can be easily integrated into traditional finite element computations and are numerically inexpensive. On the other side, these models are unable to account into detail for some phenomena such as microscopic interactions.
- **Multiscale approach:** both the microscale and the macroscale problems are solved. The main advantage of these methods is that the constitutive problem is solved at the microscale and

therefore the macroscopic constitutive equations are no longer necessary.

In the framework of multiscale approaches, when the problem is solved using nonlinear finite elements both at the material and at the structural level, i.e. a FE^2 multiscale scheme (e.g. [22, 31]) is adopted, the large number of history variables can induce high computational burden resulting in excessive computing time and memory requirements. In order to obtain an efficient numerical tool, while reducing the number of history variables, analytical or approximated nonlinear homogenization techniques can be adopted to derive the nonlinear overall response of the composite materials. The latter belong to the class of Reduced Order Models (ROMs). ROMs have received a lot of attention in the literature lately. Both the mathematical and the engineering community have been active in developing new algorithms that all seek two main objectives:

*Reduced Order
Models (ROMs)*

- the reduction of the computing time
- savings in storage and processing memory.

A rather recent review article is e.g. due to [5] and an introductory textbook was published by [57]. Basically in all ROMs approaches a natural choice is made for the quantity that is reduced: the primary unknown is approximated. For example, in dynamic problems, truncated eigenmodes of the displacement field of structures were used since the 1960s [e.g., 14, 33]. In transient thermal problems spectral decomposition can be used in order to provide modes for the temperature. Among these techniques, an interesting and effective approach is the TFA, initially introduced by Dvorak [17]. This approach explicitly avoids a parameterization of the microscopic displacement field which is the primary unknown of the micromechanical problem, but it starts from a parameterization of an internal state variable. According to Dvorak, the TFA represents an elegant way for reducing the number of internal variables by considering the microscopic field of internal variables to be suitably approximated. Nonlinearities that may arise inside the material are described by means of the inelastic strain. The interest for the TFA approach has increased in the last decades due to the simplicity and efficiency of this technique in reproducing the nonlinear overall response of heterogeneous materials.

Various TFA-based schemes were proposed, differing mainly in the assumption on the inelastic strain distribution and in the evolution of the internal variables.

TFA schemes based on the assumptions of uniform inelastic strains and periodicity conditions have been successfully used to study different nonlinear micromechanical problems, e.g. to investigate the response of the Shape Memory Alloy composite [45]. Dvorak and Bahei-El-Din [18] proposed a Piecewise Uniform TFA (PWUTFA) approach

considering the subdivision of each material phase into subsets, thus assuming a piecewise uniform inelastic strain distribution. The approach was adopted for evaluating the response of inelastic composites, with elastic-plastic, viscoplastic, or viscoelastic phases. This enhancement enabled to improve the description of the inelastic strain field but induced an increment of the complexity of the technique with respect to the original approach. Chaboche et al. [10] proposed a PWUTFA technique to study the effects of viscoplasticity and to derive the nonlinear behavior of damaging composites. The PWUTFA approach was also adopted to study masonry materials [60] and extended also to Cosserat continuum [1]. Suquet [65] demonstrated that the TFA and PWUTFA techniques could lead to too stiff predictions. Michel and Suquet [47, 48] proposed a Nonuniform TFA (NTFA) formulation, in order to improve the representation of the inelastic strain field. They considered the inelastic strain field as the superposition of functions, called inelastic modes, that are determined numerically by analyzing the response of the composite subjected to monotone loading paths. An alternative approach in order to compute the overall properties of nonlinear inelastic composites, based on the minimization of an incremental energy function considering an implicit time-discretization scheme, was proposed by Lahellec and Suquet [42]; they proved that this approach is equivalent to the TFA with a nonuniform eigenstrain field [48]. Many researchers adopted the NTFA approach proposed in [47] to study the response of nonlinear composites. In particular, Franciosi and Berbenni [24, 25] extended the original formulation to the modeling of heterogeneous crystal and poly-crystal plasticity, Roussette et al. [59] to the study of composites with elastic-viscoplastic and porous elastic-viscoplastic constituents, Fritzen and Böhlke [26, 27] to the three-dimensional analysis of micro-heterogeneous materials and Jiang et al. [40] to the analyses of porous materials. Marfia and Sacco [46] presented a nonuniform TFA procedure for the multiscale analysis of periodic masonry, considering a piecewise bilinear distribution of the inelastic strain. This procedure was formulated in a more general context by Sepe et al. [61] who proposed a New Nonuniform TFA (NUTFA) approach for studying composites with plastic and shape memory alloy constituents. This approach differs from the one proposed by Michel and Suquet [47] for two fundamental aspects: the approximation of the inelastic strains and the evaluation of the evolution of the internal variables. Fritzen and Leuschner [29] and Fritzen et al. [28] proposed a nonuniform TFA, based on the one presented in [47], considering a different way to compute the evolution of the internal variables within a mixed incremental variational approach in the framework of Generalised Standard Materials. Fritzen et al. [30] presented a comparison of the NTFA-based techniques proposed in [28, 29, 61].

Although many efforts have been done in order to improve the TFA approach, two key aspects of TFA are still object of research:

- the approximation of the inelastic field
- evolution of the reduced coefficients.

Both aspects are directly related to the number of internal variables.

*Mixed
Transformation Field
Analysis (MxTFA)*

Within the framework of reduced order homogenization methods based on the TFA approach, this work is devoted to the development of a new ROM for the analysis of nonlinear composites in order to improve those two aspects. This new technique is named Mixed TFA (MxTFA). An alternative and innovative way for representing the inelastic strain field is achieved representing the stress field and the plastic multiplier in the RVE. In particular, motivated by very good results obtained in stress recovery techniques based on the weak enforcement of the compatibility condition [4, 9, 16, 67], here the problem is formulated following a complementary approach. The response of the composite material is studied dividing its Reference Volume Element (RVE) into subdomains (subsets). The main idea (and the innovation of this technique) is to approximate the inelastic strain on the basis of a representation of the stress field and of the plastic multiplier on each subdomain, by means of the equations ruling the constitutive laws. This choice is motivated by the fact that the stress field becomes the reduced variable so that its accuracy can be directly prescribed by assigning a proper approximation. Moreover the number of variables is reduced, as the inelastic strain is derived by the stress parameters. An innovative procedure to solve the evolution equations is introduced, where the evolution laws are formulated by means of a mixed-stress approach leading to new variational equations.

The choice of a mixed-stress approach for the evolution law is motivated by the fact that it can reduce the classical stiffening effect of the homogenized material, occurring when TFA-based techniques are adopted.

This thesis is organized as follows. The basic theory of the underlying problems is briefly revised in Chapter 2. Chapter 3 is devoted to the MxTFA: the governing equations as well as the numerical procedure are discussed in Section 3.1. The analysis of nonlinear composites in the framework of elasto-plasticity is discussed in 3.2, while the case of viscoplastic materials is discussed in 3.3, together with numerical results assessing the accuracy of the presented techniques. In Chapter 4 a comparative study is presented, where the MxTFA is compared with other two reduced order models, assessing similarities and differences in the three formulations. The results of the three techniques are also compared on the 3D analysis of a viscoplastic composite. Chapter 5 is devoted to the multiscale analysis employing the MxTFA.

MULTISCALE PROBLEMS: GENERAL CONSIDERATIONS

This Chapter addresses the concept of multiscale problem, together with a review of some homogenization methods that can be found in the literature. The focus is on Reduced Order Models (ROMs), belonging to the class of semi-hybrid methods. These methods aim at the resolution of a reduced micromechanical problem. Among them, Transformation Field Analysis (TFA) techniques are considered, where the reduced variable is the inelastic strain.

2.1 MULTISCALE PROBLEM

In the discussion of the overall mechanical properties of a heterogeneous medium, two or more scales coexist. Here two scales are assumed, termed macroscopic and microscopic scale respectively. The macroscale is the structural scale, at which the material can be considered as homogeneous and its behavior is described by effective (or overall) properties. The microscale is the scale at which the material exhibits its microstructure characterized by different phases, each of them with a different constitutive behavior. In addition, the microscale and the macroscale are characterized by different length scales: the macroscale dimension λ_{macro} is the structural dimension, while the microscale dimension λ_{micro} is the typical scale of the heterogeneities. It is assumed that $\lambda_{\text{macro}} \gg \lambda_{\text{micro}}$ and that also the mechanical fields at the two scales admit different fluctuation lengths accordingly. Under these conditions, the scale separation hypothesis holds. Under the hypothesis of scale separation, it is possible to derive the effective properties of a composite medium if a Reference Volume Element (RVE) can be defined for the composite. The RVE, represents a Statistically Homogeneous Medium, i.e. it behaves as a homogeneous material at the macroscale [37, 39]. Once the RVE is defined, the macroscopic mechanical quantities that are assumed to be additive functions can be obtained by averaging the corresponding microscopic ones over the RVE occupying a volume Ω and characterized by different phases.

*Reference Volume
Element (RVE)*

For each RVE, the generic macroscopic quantity $\bar{\bullet}$ is obtained from the microscopic one \bullet as:

$$\bar{\bullet} = \langle \bullet \rangle = \frac{1}{\Omega} \int_{\Omega} (\bullet) \, d\Omega. \quad (1)$$

being $c^m = \frac{\Omega^m}{\Omega}$ the volume fraction of the single phase m . It should be emphasized that Eq. (1) holds in absence of voids or cracks. In

periodic media, the Unit Cell (UC) plays the role of the RVE. In case of random microstructures, the Statistical Volume Element (SVE) is analyzed instead of the RVE. Mathematical tools for the characterization of random microstructures are presented in [52].

Two-scale problem

Given a composite body $\bar{\Omega}$, a RVE is associated to each material point at the macroscopic scale \bar{x} , as shown in Fig. 1.

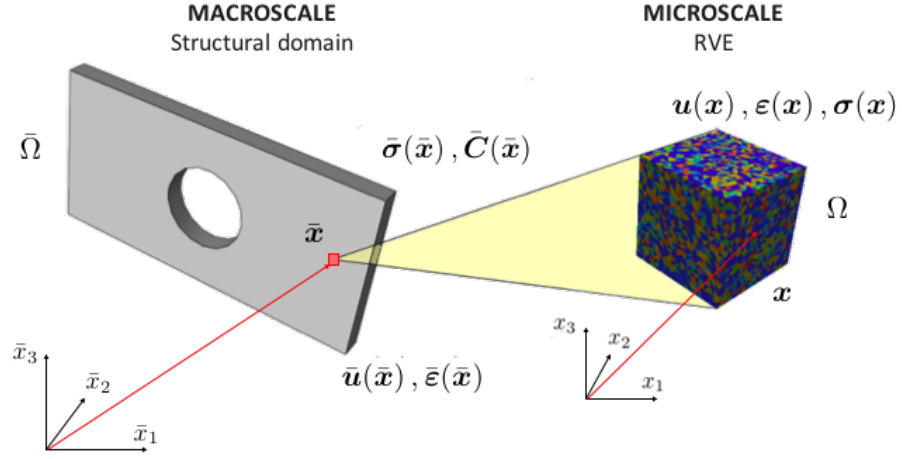


Figure 1: Multiscale problem.

The resolution of the structural problem for $\bar{\Omega}$ adopting a multiscale technique is detailed in the following, in a framework of small strains. The mechanical response of the at the macroscale is described by the (effective) fields that are overlined. In order to take into account for the heterogeneous microstructure of $\bar{\Omega}$ in the evaluation of its effective mechanical properties, a RVE Ω is identified. At the microscale the material is heterogeneous and its mechanical response is described by the fields that are not overlined. A continuum mechanical description is used on both scales, i.e. at both scales the stresses ($\bar{\boldsymbol{\sigma}}$ and $\boldsymbol{\sigma}$) and the strains ($\bar{\boldsymbol{\varepsilon}}$ and $\boldsymbol{\varepsilon}$) need to be asserted. At the macroscale, the BVP that need to be solved involves compatibility and equilibrium equations only:

$$\bar{\boldsymbol{\varepsilon}} = \mathbf{D}\bar{\mathbf{u}} \quad (2)$$

$$\mathbf{D}^T \bar{\boldsymbol{\sigma}} = -\mathbf{f}, \quad (3)$$

where \mathbf{D} and \mathbf{D}^T are the compatibility and equilibrium operators respectively, $\bar{\boldsymbol{\varepsilon}}$ and $\bar{\boldsymbol{\sigma}}$ the macro strain and stresses, $\bar{\mathbf{u}}$ is the macroscopic displacement vector and \mathbf{f} is the vector of body forces. In order to solve the problem (2)-(3), boundary conditions are required. As known in solid mechanics, they can be:

- Dirichlet boundary conditions: prescribed value of the displacements (or strains),
- Neumann boundary conditions: prescribed value of tractions,

- Mixed boundary conditions: a combination of the above.

No relation between the effective stress $\bar{\sigma}$ and effective strain $\bar{\varepsilon}$ is derived at this scale. In fact, the constitutive problem is solved at the microscale only, and the effective constitutive relation is obtained via homogenization.

2.2 MICROMECHANICAL PROBLEM

Once the RVE Ω is determined for every macroscopic point $\bar{\mathbf{x}}$ of the structural body $\bar{\Omega}$, the following BVP has to be solved (neglecting body forces):

$$\boldsymbol{\varepsilon} = \mathbf{D}\mathbf{u} \quad (4)$$

$$\mathbf{D}^\top \boldsymbol{\sigma} = \mathbf{o} \quad (5)$$

$$\boldsymbol{\sigma} = \mathcal{F}(\boldsymbol{\varepsilon}) \quad (6)$$

$$\langle \boldsymbol{\sigma} \rangle = \bar{\boldsymbol{\sigma}} \quad (7)$$

$$\langle \boldsymbol{\varepsilon} \rangle = \bar{\boldsymbol{\varepsilon}}. \quad (8)$$

In the above equations, $\boldsymbol{\sigma}$ and $\boldsymbol{\varepsilon}$ are the microscopic stress and strain tensors respectively, while \mathbf{u} is the displacement vector. The latter is represented as the sum of two contributions:

$$\mathbf{u}(\boldsymbol{\chi}) = \bar{\boldsymbol{\varepsilon}} \boldsymbol{\chi} + \tilde{\mathbf{u}}(\boldsymbol{\chi}), \quad (9)$$

where the first term is the contribution due to the applied average strain field $\bar{\boldsymbol{\varepsilon}}$ coming from the macroscale and $\tilde{\mathbf{u}}$ is the perturbed displacement field. From Eqs. (9) and (4) it results that the local strain is split into an average and a fluctuating term accordingly:

$$\boldsymbol{\varepsilon}(\boldsymbol{\chi}) = \bar{\boldsymbol{\varepsilon}} + \tilde{\boldsymbol{\varepsilon}}(\boldsymbol{\chi}), \quad (10)$$

being $\tilde{\boldsymbol{\varepsilon}}$ the perturbation strain characterized by zero mean, due to the fact that the microscopic fields oscillations are not perceived at the macroscopic scale (scale separation hypothesis):

$$\langle \tilde{\boldsymbol{\varepsilon}} \rangle = \mathbf{o}. \quad (11)$$

These decompositions were initially proposed by [64] and then developed by Swan [66] for the homogenization of inelastic periodic composites. It should be emphasized the use of the superposition principle in (9) and (10) limits the analysis to small-strain problems. The above problem is ill-posed due to the absence of suitable boundary conditions on the RVE boundary $\partial\Omega$. Proper boundary conditions have to be imposed, in order to properly represent the in-situ state of the RVE inside the material (i.e. in order to reproduce statistical homogeneous fields), taking into account for the interactions produced inside the composite internal structure. In particular, the boundary

Boundary conditions

conditions should provide stress σ and strain ε fields whose averages are the macrostresses $\bar{\sigma}$ and macrostrains $\bar{\varepsilon}$, respectively. In case of Dirichlet boundary conditions, they are uniform strains (linear displacements), while uniform tractions are imposed in case of Neumann conditions [34, 38]. In case of a given macroscopic strain $\bar{\varepsilon}$, linear displacements (i.e. uniform strains $\bar{\varepsilon}$) can be prescribed at the boundaries $\partial\Omega$:

$$\mathbf{u}(\mathbf{x}) = \bar{\varepsilon} \mathbf{x}, \quad \forall \mathbf{x} \in \partial\Omega. \quad (12)$$

This boundary condition ensures $\langle \varepsilon \rangle = \bar{\varepsilon}$. Alternatively, uniform tractions can be applied to the boundary:

$$\mathbf{t}(\mathbf{x}) = \bar{\sigma} \cdot \mathbf{n}(\mathbf{x}), \quad \forall \mathbf{x} \in \partial\Omega, \quad (13)$$

ensuring the fulfillment of $\langle \sigma \rangle = \bar{\sigma}$.

Once the above conditions are specified, the localization problem is well posed and the equality of virtual works (or Hill-Mandel condition [37]) holds:

$$\langle \sigma : \varepsilon \rangle = \langle \sigma \rangle : \langle \varepsilon \rangle = \bar{\sigma} : \bar{\varepsilon}. \quad (14)$$

This equality is independent on the constitutive law and states that the average of the microscopic work equals the macroscopic work.

2.3 HOMOGENIZATION PROBLEM

Homogenization aims at the determination of the constitutive relation between the effective properties, i. e. the effective constitutive law for the heterogeneous material. Assuming a linear elastic material behavior for sake of simplicity, the effective constitutive behavior reads as:

$$\bar{\sigma}(\bar{\mathbf{x}}) = \bar{\mathbf{C}}(\bar{\mathbf{x}}) \bar{\varepsilon}(\bar{\mathbf{x}}) \quad (15)$$

$$\bar{\varepsilon}(\bar{\mathbf{x}}) = \bar{\mathbf{S}}(\bar{\mathbf{x}}) \bar{\sigma}(\bar{\mathbf{x}}), \quad (16)$$

where $\bar{\mathbf{C}}$ and $\bar{\mathbf{S}}$ are the effective elastic stiffness and compliance tensors respectively. In a framework of isothermal, elastic deformation, the local problem (4)-(8) is a linear problem, that allows the definition of the localization tensors:

$$\begin{aligned} \sigma(\mathbf{x}) &= \mathbf{B}(\mathbf{x}) \bar{\sigma} \\ \varepsilon(\mathbf{x}) &= \mathbf{L}(\mathbf{x}) \bar{\varepsilon}. \end{aligned} \quad (17)$$

It can be easily shown that the effective moduli can be determined from the strain or stress localization tensors:

$$\bar{\mathbf{C}} = \langle \mathbf{C} \mathbf{L} \rangle, \quad (18)$$

$$\bar{\mathbf{S}} = \langle \mathbf{S} \mathbf{B} \rangle. \quad (19)$$

In the literature, different homogenization methods were developed for the evaluation of the effective constitutive behavior. They can mainly be subdivided into (semi)-analytical methods, computational methods and hybrid methods, as reported in Fig. 2.

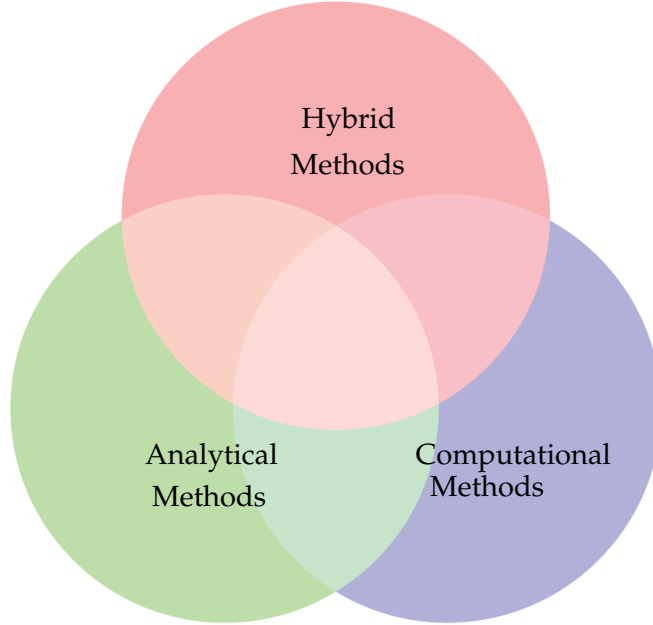


Figure 2: Homogenization methods: classification.

Semi-analytical methods replace the localization tensors (17) by means of analytical expressions. Since their evaluation is generally out of reach for these methods, their phase-average \bar{n} is generally derived. In addition, the microscopic fields are not derived, that means that the micromechanical problem (5)-(8) is not solved by these methods. A sub-class of analytical methods is able to provide some bounds and estimates for the effective behavior based on some variational considerations. Among them, assuming a uniform distribution of the applied strain/stress, Voigt [68] and Reuss [58] determined an estimate for the effective elastic stiffness and compliance tensors respectively, as weighted mean of the phase m stiffness \mathbf{C}^m or compliance \mathbf{S}^m respectively:

*Semi-analytical
methods*

$$\mathbf{C}_V = \sum_{m=1}^M c^m \mathbf{C}^m, \quad \mathbf{S}_V = \mathbf{C}_V^{-1} \quad (20)$$

and

$$\mathbf{S}_R = \sum_{m=1}^M c^m \mathbf{S}^m, \quad \mathbf{C}_R = \mathbf{S}_R^{-1}, \quad (21)$$

where Ω^m is the phase volume, $c^m = \frac{\Omega^m}{\Omega}$ is the phase volume fraction, M is the total number of phases and $\mathbf{C}_V, \mathbf{S}_V$ and $\mathbf{C}_R, \mathbf{S}_R$ indicate

the estimate of the elastic stiffness and compliance tensors according to Voigt and Reuss respectively. The Reuss estimate cannot be applied if the microstructure is characterized by voids or porosity (due to the non existence of the compliance tensor in that case), while Voigt estimate holds for all materials. Based on a reformulation of the problem in an equivalent variational formulation of elasticity, Hill [36] found that the Voigt and Reuss estimates are bounds for the elastic effective stiffness and compliance tensors:

$$\mathbf{C}_R \leq \bar{\mathbf{C}} \leq \mathbf{C}_V, \quad \mathbf{S}_R \geq \bar{\mathbf{S}} \geq \mathbf{S}_V. \quad (22)$$

Hashin and Shtrikmann [35, 71, 72] extended Hill's findings [36] to statistically isotropic microstructures, providing an upper and a lower bound for the elastic effective tensor for a two-phase material. These two bounds are characterized by a smaller range with respect to (22), that are not able to provide useful estimates, especially when the difference between the elastic properties of the constituents becomes large. Walpole [69] generalized the results to certain types of anisotropic composites and Willis [70] to microstructures exhibiting ellipsoidal symmetry. The existence of these bounds is due to the fact that the assumed boundary conditions prescribed on the RVE are not the actual in-situ boundary conditions. In fact, in case of displacement boundary conditions, although they are admissible, they will produce a higher strain energy than the in-situ boundary conditions (that minimize the strain energy). Same in case of applied tractions, resulting in higher complementary energy and therefore higher compliance. Eshelby [20] solved the problem of a single inclusion embedded into an infinite matrix domain, assuming no interaction between the particles. The Mori-Tanaka [49] method approximates the phase interactions by assuming that each inclusion is immersed, in turn, in an infinite matrix: in this way, each inclusion behaves like an isolated inclusion in the matrix seeing the average matrix strain as a far-field strain [6]. An improved approach is introduced by the Self Consistent method [8, 38], where the problem of phase interactions is solved by considering the single particle embedded in an infinite effective medium. Since the effective properties of the infinite medium are not known, the method requires the iterative solution of a nonlinear equation. The method is able to provide a good prediction on the behavior of polycrystals, but less accurate results are obtained in case of two-phase composites, as shown in [55].

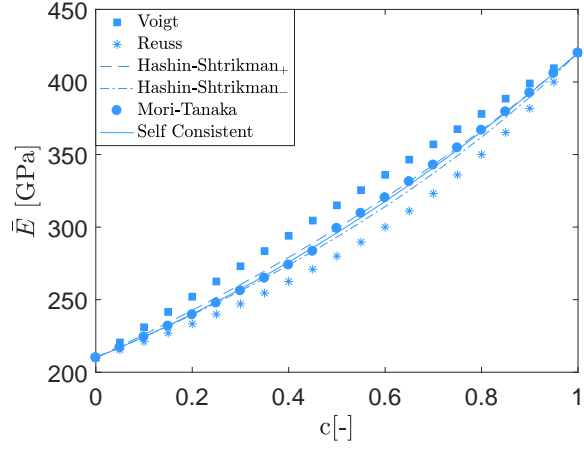
Examples

Some estimates on the effective Young's modulus \bar{E} for different semi-analytical methods are collected in Fig.3. In particular, a two-phase composite characterized by a spherical inclusion embedded into a matrix is considered. The Young's modulus of the matrix E_0 is set to 210 GPa, while increasing Young's moduli for the inclusion E_1 are considered (420, 1050 and 2100 GPa respectively). The Poisson's coefficient ν is set equal to 0.25 for both constituents. It

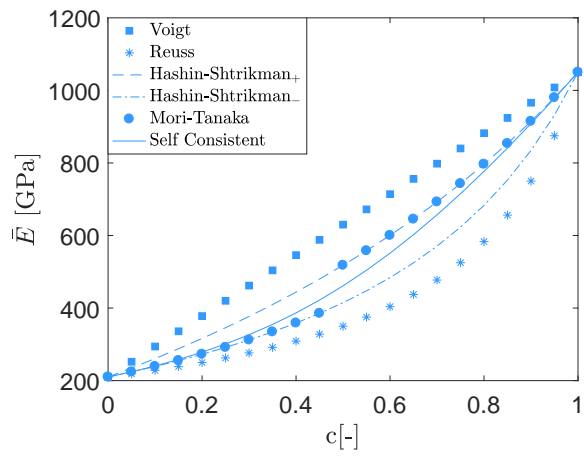
can be noted that all methods differ significantly from each other as the phase contrast increases, and that Voigt and Reuss estimates represent the maximum upper bound and minimum lower bound respectively. The two Hashin-Shtrikman estimates provide narrower bounds, that can be sufficient for moderate matrix-inclusion contrast. The Mori-Tanaka scheme coincides with the Hashin-Shtrikman lower bound for volume fraction $c < 0.5$, while for $c > 0.5$ it coincides with the upper bound (this is due to the fact that according to the Mori-Tanaka method, the matrix material is defined as the phase with higher volume fraction). The Self Consistent estimate is always within the Hashin-Shtrikman bounds.

Fig. 4 shows 3D-surface plots of the prediction of different methods for varying stiffness ratios \bar{E}/E_0 and inclusion volume fractions c : a similar study was presented in [41]. On one side, a linear dependence of the effective Young's modulus can be observed for the Voigt estimate, representing the upper bound. On the other side, the lower bound represented by the Reuss estimate shows an increase in the prediction only for high values of c and E_1/E_0 . A correspondence between the the Mori-Tanaka and the the lower Hashin-Shtrikman bound surfaces can be observed, while the Self Consistent shows a nearly linear behavior for high values of c and E_1/E_0 .

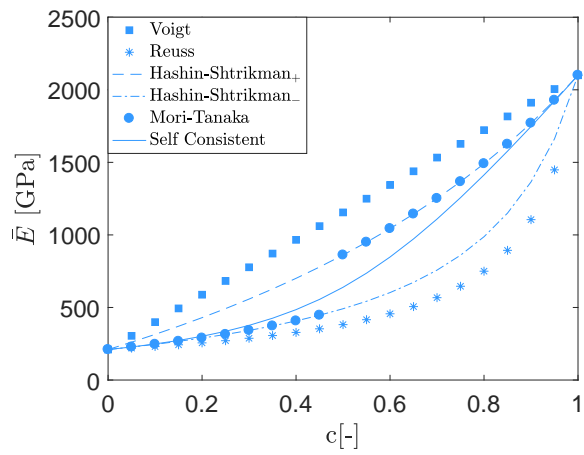
The semi-analytical methods are able to provide a solution assuming linear behavior of the constituents and for limited microstructural geometries, but they cannot be employed for arbitrary geometries and for nonlinear constitutive behaviors. In fact, when dealing with physical nonlinearities, the global and the local response can be both time and path dependent and no mathematical model would be able to derive the homogenized properties directly from the microstructure. A first idea could be a full discretization of the structure using finite element analysis. In this case, the required discretization should be at least as fine as the size of the heterogeneities, but this would be impossible due to prohibitively high computational costs. On one side, a possible solution is the development of a phenomenological model, in order to obtain a macroscopic constitutive relation for the RVE from experimental observations that yield the relevant mechanisms which are responsible for the global response. The advantage of this kind of approaches is that they are easy to use: once the global constitutive relation is known, the structure is modeled via finite element method. The main drawback of this approach is that certain assumptions are required and some information, e.g. details for the microscopic interactions, might be lost. Another way of deriving the phenomenological model is to perform numerical computations on a detailed discretization of the RVE. This approach is the so-called unit cell method and has been used in [7, 11, 50]. On the other side, integrated methods could be employed. A discretization of the microstructure is used, and the relationship between microscopic and



(a)



(b)



(c)

Figure 3: Comparison of effective Young's modulus for different methods as function of the volume fraction c - (a) $E_1 = 420\text{GPa}$, (b) $E_1 = 1050\text{GPa}$, (c) $E_1 = 2100\text{GPa}$

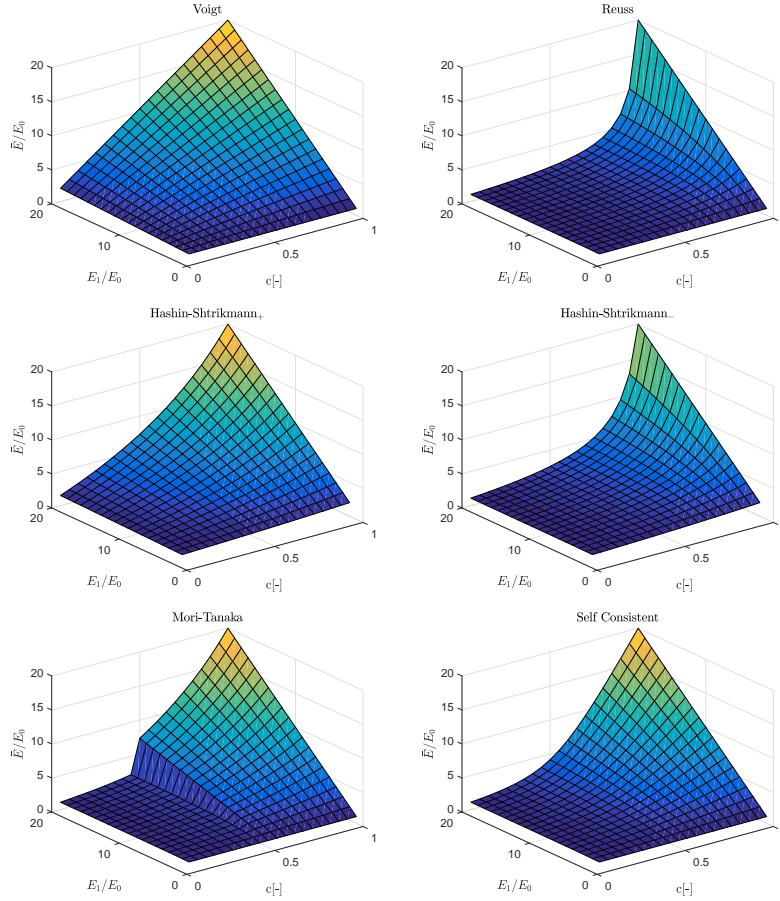


Figure 4: Prediction of the effective Young's modulus for different concentrations c and different stiffness ratios E_I/E_M .

macroscopic quantities is derived via homogenization rules. Among these methods, an interesting approach is the nested finite element method, or FE^2 method, introduced by Feyel [21–23]. According to this method, both the structure at the macroscale and the microstructure (i. e. the RVE) are discretized using finite element method (see Fig. 5). A RVE is associated to each integration point at the macroscale: two finite element meshes are needed, one for the RVE and one for the structure. The numerical analysis is then carried out simultaneously at both scales. At the generic macroscopic integration point, knowing the strain and the strain rate at time t , the local problem (5)-(8) is solved on the RVE and the homogenized stress field $\bar{\sigma}$ and the algorithmic homogenized tangent stiffness $\bar{\mathbb{C}}$ are derived for that RVE via (15)-(16), becoming the stress and the stiffness of that integration point at that time. The advantage of this method is that no macroscopic constitutive behavior has to be specified, since the constitutive relations enter the microscopic problem only and for this reason any constitutive behavior can be modeled. In addition, since also the RVE is discretized by finite elements, this method can be applied to any geometry. The main disadvantage of the FE^2 is related to the high

number of variables. Since the microscopic problem is solved for every integration point of the structure, all the history variables at time t_n need to be stored until the equilibrium at the current state t is reached.

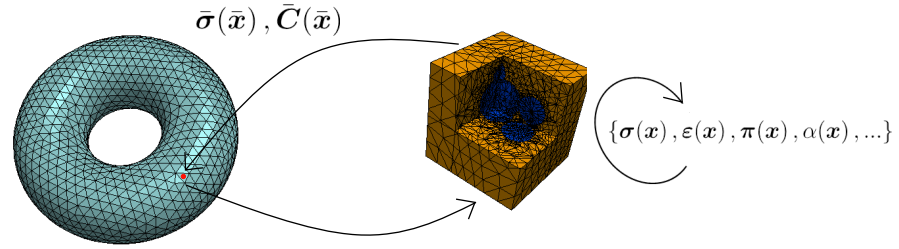


Figure 5: Schematic diagram of the FE^2 model.

Hybrid methods

Hybrid methods incorporate computational aspects but also a theoretical background. In these type of methods, the analytical expression for the localization tensors (17) is replaced by their numerically derived expression. A relationship between the microscopic and macroscopic fields is established so that once the constitutive equations are evaluated locally, their macroscopic counter part can be derived. Reduced Order Models (ROMs) belong to this class of homogenization methods, and among them, the Transformation Field Analysis (TFA).

2.4 TRANSFORMATION FIELD ANALYSIS

The transformation field analysis (TFA) was initially introduced by Dvorak [17], and it is a method aimed at the solution of thermo-mechanical loading problems in heterogeneous materials. According to Dvorak, such materials experience stress and strain fields deriving from mechanical loads, but also eigenstrains, or transformation strains, and corresponding residual stresses. The transformation fields may consist of different contributions (e.g. thermal and inelastic effects). The impact of these transformation fields on the composite can have large influence on the overall behavior of the material. The TFA applies to many constitutive material models for composites that admit an additive decomposition of the small strains into elastic and inelastic components:

$$\varepsilon(\mathbf{x}) = \varepsilon_e(\mathbf{x}) + \boldsymbol{\pi}(\mathbf{x}), \quad (23)$$

being $\varepsilon_e(\mathbf{x})$ the elastic strain and $\boldsymbol{\pi}(\mathbf{x})$ the inelastic strain, which is treated as a transformation strain inside the material. Assuming a distribution of the transformation fields over each phase, the local fields are determined by solving a system of differential equations depending on the localization (or concentration) tensors, that derive from the

solution of elastic problems for locally applied eigenstrains or eigenstresses and can be reconstructed either numerically (e. g. via Finite Element Analysis (FEA)) or semi-analytically (e. g. via semi-analytical methods, see 2.3). As mentioned in Chapter 1, different TFA-based schemes have been developed assuming different distribution for the transformation fields. In the following, the basic concepts of the TFA proposed by Dvorak are summarized.

2.4.1 Local and overall fields

It is assumed that a RVE occupying a volume Ω and characterized by M phases can be identified for the heterogeneous material. Then the response of the generic point \mathbf{x} at any time t in terms of total strains and stresses can be decomposed as:

$$\boldsymbol{\varepsilon}(\mathbf{x}, t) = \boldsymbol{\varepsilon}_{\bar{\varepsilon}}(\mathbf{x}, t) + \boldsymbol{\varepsilon}_{\pi}(\mathbf{x}, t), \quad (24)$$

where $\boldsymbol{\varepsilon}_{\bar{\varepsilon}}$ and $\boldsymbol{\varepsilon}_{\pi}$ denote the mechanical strain and the transformation strain contributions to the total strain. As mentioned before, the transformation fields may result from different contributions and can therefore be further decomposed. Here only the inelastic effects are considered. From now on the time dependency will be omitted. The contribution to (24) provided by the overall applied strain $\bar{\varepsilon}$ deriving from the imposed mechanical loads and the inelastic strain are:

$$\boldsymbol{\varepsilon}_{\bar{\varepsilon}}(\mathbf{x}) = \mathbf{L}_{\bar{\varepsilon}}(\mathbf{x})\bar{\varepsilon}, \quad \boldsymbol{\varepsilon}_{\pi}(\mathbf{x}) = \int_{\Omega} \mathbf{L}_{\pi}(\mathbf{x}, \mathbf{x}') \boldsymbol{\pi}(\mathbf{x}') d\Omega. \quad (25)$$

where $\mathbf{L}_{\bar{\varepsilon}}(\mathbf{x})$ is the mechanical localization operator and $\mathbf{L}_{\pi}(\mathbf{x}, \mathbf{x}')$ is the eigenstrain localization operator that evaluates the effect at \mathbf{x} induced by a transformation strain in \mathbf{x}' . Eq. (25) shows that the localization operators depend only on the local geometry and on the elastic response of the material. The reduction is performed by replacing the inelastic continuous fields by their approximation within the RVE. In [18] piecewise uniform approximation in the phase is adopted, by assuming a uniform distribution over phase subsets Ω^j , with $j = 1, \dots, n$. As a consequence, in each subset Ω^j (24) is rewritten as:

$$\boldsymbol{\varepsilon}^j = \mathbf{L}_{\bar{\varepsilon}}^j \bar{\varepsilon} + \sum_{i=1}^n \mathbf{L}_{\pi^i}^j \boldsymbol{\pi}^i, \quad (26)$$

where $\mathbf{L}_{\bar{\varepsilon}}^j$ and $\mathbf{L}_{\pi^i}^j$ are the localization operators for the subset Ω^j . The overall fields are connected to the local fields according to (1).

2.4.2 Pre-analyses

The pre-analyses are the offline phase necessary for the assessment of the localization operators $\mathbf{L}_{\bar{\varepsilon}}(\mathbf{x})^j$ and $\mathbf{L}_{\pi^i}(\mathbf{x}, \mathbf{x}')^j$. Their evaluation can be performed either analytically or numerically (e.g. via Finite Element Analysis (FEA)) by applying to the microstructure suitable boundary conditions. For instance, in case of periodic composites, periodic boundary conditions are applied to the RVE that is discretized into finite elements. The coefficients of $\mathbf{L}_{\bar{\varepsilon}}^j$ are determined solving 6 elasticity problems, where in each solution the RVE is subjected to overall strain $\bar{\varepsilon}$ that has only one active unit component. In particular the strain field found at \mathbf{x} belonging to Ω^j is the column of the localization tensor $\mathbf{L}_{\bar{\varepsilon}}^j(\mathbf{x})$ corresponding to the selected unit component. Similarly for $\mathbf{L}_{\pi^i}^j$, a unit inelastic strain is applied on Ω^i , and the local strains are derived in all the points. Each local strain in the \mathbf{x} is the column of the localization tensor $\mathbf{L}_{\pi^i}^j$. The unit eigenstrains can be produced either as distortions or as thermal strains. Figure 6 provides a graphical representation of the evaluation of the numerical localization tensors.

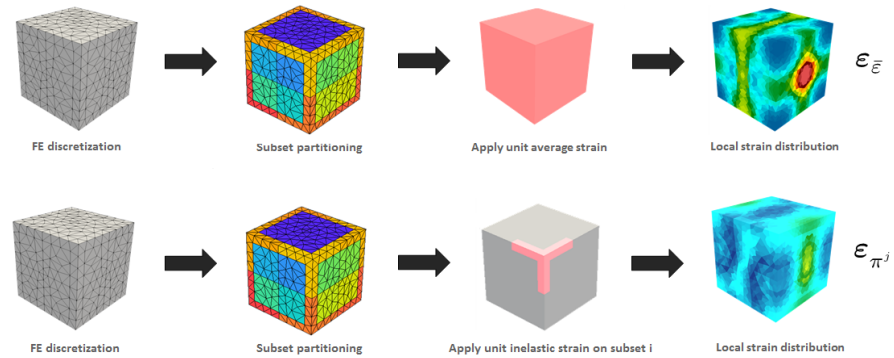


Figure 6: TFA - Pre-analyses (Offline phase).

2.4.3 Evolution problem

In order to evaluate the inelastic local fields on the RVE, a specific constitutive law need to be introduced for every phase (and therefore for every subset) in order to connect the inelastic strain (or the residual stress) to the prescribed overall path. Since the localization operators depend on elastic moduli and local geometry only, if those remain constant, then the constitutive equations describing the evolution of the inelastic strain (or residual stress) can be solved in order to evaluate the stress and strain increments along a prescribed overall strain/stress history. Dvorak [17, 19] provides the explicit governing equations assuming different material models for the composite phases (e.g. elastic-plastic, viscoelastic and viscoplastic systems).

MIXED TRANSFORMATION FIELD ANALYSIS (MXTFA)

In this Chapter the MxTFA technique is introduced. This new TFA method is based on a mixed-stress variational approach involving self-equilibrated stresses and the plastic multiplier as independent variables on RVE subsets. The chapter is organized as follows: in Section 3.1 the main ideas of the MxTFA are outlined, from the theoretical aspects to the numerical procedure. Sections 3.2 and 3.3 are dedicated to the homogenization within the framework of elasto-plasticity and viscoplasticity respectively. For each Section numerical results are presented in order to assess the accuracy of the proposed procedure. In particular, nonlinear periodic composites are analyzed.

3.1 MAIN IDEA

The local strain energy is:

$$\psi(\boldsymbol{\varepsilon}, \boldsymbol{\pi}, \alpha) = \frac{1}{2}(\boldsymbol{\varepsilon} - \boldsymbol{\pi})^T \mathbf{C}(\boldsymbol{\varepsilon} - \boldsymbol{\pi}) + h(\alpha), \quad (27)$$

being $\boldsymbol{\pi}$ the inelastic strain and α the accumulated plastic strain. The microscopic state laws are then derived as:

$$\boldsymbol{\sigma} = \frac{\partial \psi}{\partial \boldsymbol{\varepsilon}} = \mathbf{C}(\boldsymbol{\varepsilon} - \boldsymbol{\pi}) \quad (28)$$

$$r = \frac{\partial \psi}{\partial \alpha} = \frac{\partial h}{\partial \alpha}. \quad (29)$$

In the following, a linear hardening law is considered, but nonlinear hardening laws could as well be considered:

$$h(\alpha) = \frac{1}{2}H \alpha^2 \quad \Rightarrow \quad r = H \alpha, \quad (30)$$

where H is the hardening parameter. The homogenization problem (4)-(8) is restated imposing the weak form of the compatibility equation, taking into account for the strain decomposition (10):

$$\int_{\Omega} \delta \boldsymbol{\sigma}^T \mathbf{C}^{-1} \boldsymbol{\sigma} \, d\Omega - \int_{\Omega} \delta \boldsymbol{\sigma}^T (\bar{\boldsymbol{\varepsilon}} + \tilde{\boldsymbol{\varepsilon}} - \boldsymbol{\pi}) \, d\Omega = 0 \quad \forall \delta \boldsymbol{\sigma} : \mathbf{D}^T \delta \boldsymbol{\sigma} = \mathbf{0} \quad . \quad (31)$$

The above equation is completed introducing a yield condition for the stress and the evolution equations for the internal variables. A yield function f is introduced, such that the stress is admissible if $f \leq 0$.

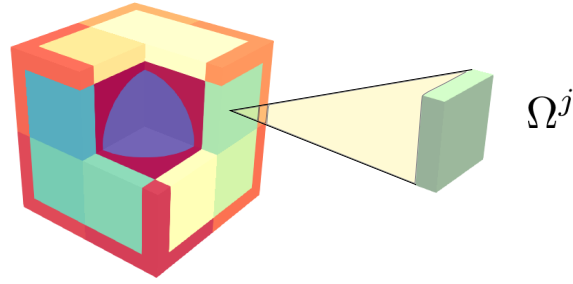


Figure 7: MxTFA: RVE partitioning into subsets.

An associated flow rule is assumed, relating the inelastic strain rate to the yield function:

$$\dot{\pi} = \dot{\lambda} \mathbf{N}(\boldsymbol{\sigma}) \quad \text{with} \quad \mathbf{N}(\boldsymbol{\sigma}) = \frac{\partial f(\boldsymbol{\sigma}, r)}{\partial \boldsymbol{\sigma}}, \quad (32)$$

where λ is a non negative plastic multiplier. The evolution laws for the internal variables, i. e. the inelastic strain π and the hardening variable (or accumulated plastic strain) α depend on the assumed constitutive model (see 3.2 and 3.3). The RVE is divided into n subsets (or subdomains) Ω^j with $j = 1, \dots, n$ such that:

Subset partitioning

$$\Omega = \bigcup_{j=1}^n \Omega^j. \quad (33)$$

The partitioning is performed considering the microstructural geometry of the material. For instance, partitions should account for position, shape and symmetry of inclusions. The subsets can have arbitrary and even non-convex shape (as shown in Fig. 7), and this allows, in principle, to partition any microstructure without restraints. In the following, the material properties are intended as those of the subset. The proposed MxTFA exploits the typical approach of mixed stress finite elements in which piecewise continuous representations for the stress components over the domain are allowed and traction continuity among the subdomains is not required. Thus, in the MxTFA the stresses are approximated independently over each subset of the RVE. In particular, the stress field $\boldsymbol{\sigma}^j$ at the generic time t in the typical j -th subset Ω^j , is approximated as (no sum on j):

Approximations

$$\boldsymbol{\sigma}^j(\mathbf{x}, t) = \mathbf{P}^j(\mathbf{x}) \hat{\boldsymbol{\sigma}}^j(t), \quad (34)$$

where \mathbf{P}^j is a matrix collecting a set of N_p^j self-equilibrated stress modes (the number of stress modes N_p^j can be chosen differently for each subset Ω^j) and $\hat{\boldsymbol{\sigma}}^j$ the vector of the unknown N_p^j stress parameters. In other words, the self-equilibrated stress in the subset is represented as linear combination of chosen self-equilibrated modes, that need to satisfy the requirement of zero divergence over the subset Ω^j .

A modified plastic multiplier γ , related to the hardening variable (or accumulated plastic strain) α is introduced, with the the only aim to simplify the form of the evolution equation for the following developments (i.e. the hardening variable is recovered from $\dot{\alpha}$ and not from $\dot{\gamma}$):

$$\dot{\gamma} = \dot{\gamma}(\dot{\alpha}). \quad (35)$$

The modified plastic multiplier is also approximated in each subset Ω^j independently from the representation of the stress field as:

$$\dot{\gamma}^j(\mathbf{x}, t) = \sum_{i=1}^{N_\rho^j} \rho_i^j(\mathbf{x}) \dot{\gamma}_i^j(t) = \boldsymbol{\rho}^{jT}(\mathbf{x}) \dot{\boldsymbol{\gamma}}^j(t), \quad (36)$$

where $\boldsymbol{\rho}^j$ is a set of N_ρ^j modes chosen to approximate the plastic multiplier $\dot{\gamma}$ in Ω^j and $\dot{\boldsymbol{\gamma}}^j$ is the vector containing the corresponding coefficients. In principle, different number of modes N_ρ^j can be used to represent the inelastic multiplier in each subset, but a simple and common choice is to consider a piecewise uniform distribution for $\dot{\gamma}^j$, i.e. it is set $\rho^j = 1$ in all subsets.

In the following, the time dependency will be omitted for sake of simplicity.

Taking into account the equations (34) and (36), the flow rule equation (32) in the subset Ω^j takes the form:

$$\boldsymbol{\pi}^j = \boldsymbol{\rho}^{jT} \hat{\boldsymbol{\gamma}}^j \hat{\mathbf{N}}(\hat{\boldsymbol{\sigma}}^j) \quad \text{with} \quad \hat{\mathbf{N}}(\hat{\boldsymbol{\sigma}}^j) = \mathbf{N}(\mathbf{P}^j \hat{\boldsymbol{\sigma}}^j). \quad (37)$$

Equation (37) reveals that the approximation introduced for the stress field in the subset Ω^j , through the flow rule condition, induces a representation form for the inelastic strain rate in that subset. A weak form describing the evolution of the modified plastic multiplier needs to be introduced in order to close the problem, since it is one of the two reduced variables, together with the stress field. Sections 3.2 and 3.3 provide the explicit expression of this weak form in a framework of elasto-plasticity and viscoplasticity respectively.

The total strain at the typical point \mathbf{x} of Ω^j depends on the average strain $\bar{\boldsymbol{\varepsilon}}$ and on the distribution of the inelastic strain $\boldsymbol{\pi}$ in the whole RVE. As a consequence, the perturbation strain field $\tilde{\boldsymbol{\varepsilon}}^j$ can be split in two contributions:

Local strain

$$\tilde{\boldsymbol{\varepsilon}}^j = \tilde{\boldsymbol{\varepsilon}}_\varepsilon^j + \tilde{\boldsymbol{\varepsilon}}_\pi^j = \mathbf{L}_\varepsilon^j \bar{\boldsymbol{\varepsilon}} + \sum_{i=1}^n \mathbf{L}_{\pi^i}^j \boldsymbol{\pi}^i, \quad (38)$$

where $\tilde{\boldsymbol{\varepsilon}}_\varepsilon^j$ and $\tilde{\boldsymbol{\varepsilon}}_\pi^j$ are the perturbation strains due to the average strain and to the presence of the inelastic field, respectively; \mathbf{L}_ε^j and $\mathbf{L}_{\pi^i}^j$ are localization operators, whose evaluation is performed using the finite

Pre-analyses

element method. In particular, the k -th column of the localization matrices $\mathbf{L}_{\bar{\boldsymbol{\varepsilon}}}^j(\mathbf{x})$ is evaluated computing the strain at $\mathbf{x} \in \Omega^j$, when the UC is subjected to the k -th component of $\bar{\boldsymbol{\varepsilon}}$ equal to $\mathbf{1}$ and all the others equal to zero; analogously, the p -th column of $\mathbf{L}_{\boldsymbol{\pi}^i}^j(\mathbf{x})$ is evaluated computing the strain at $\mathbf{x} \in \Omega^j$ when the sub-domain Ω^i of the UC is subjected to the p -th mode and all the others equal to zero. In order to ensure consistency between the representations of stress, total and inelastic strain, the following approximation $\check{\boldsymbol{\varepsilon}}^j$ of the perturbation strain $\tilde{\boldsymbol{\varepsilon}}^j$ is introduced in Ω^j :

$$\check{\boldsymbol{\varepsilon}}^j = \boldsymbol{\Pi}^j \hat{\boldsymbol{\varepsilon}}^j, \quad (39)$$

where $\boldsymbol{\Pi}^j = \boldsymbol{\Pi}^j(\mathbf{x})$ denotes a set of strain modes and $\hat{\boldsymbol{\varepsilon}}^j$ is a vector of unknown parameters. $\check{\boldsymbol{\varepsilon}}^j$ is evaluated as the projection of $\tilde{\boldsymbol{\varepsilon}}^j$ obtained by enforcing the weak form condition:

$$0 = \int_{\Omega^j} (\delta \check{\boldsymbol{\varepsilon}}^j)^T (\check{\boldsymbol{\varepsilon}}^j - \tilde{\boldsymbol{\varepsilon}}^j) d\Omega, \quad (40)$$

obtaining:

$$\hat{\boldsymbol{\varepsilon}}^j = \left(\int_{\Omega^j} \boldsymbol{\Pi}^{jT} \boldsymbol{\Pi}^j d\Omega \right)^{-1} \int_{\Omega^j} \boldsymbol{\Pi}^{jT} \tilde{\boldsymbol{\varepsilon}}^j d\Omega. \quad (41)$$

Note that Eq. (40) ensures that the average and the first moment of $\check{\boldsymbol{\varepsilon}}^j$ and $\tilde{\boldsymbol{\varepsilon}}^j$ are the same in every subset. This ensures that Eq. (8) is fulfilled also by $\check{\boldsymbol{\varepsilon}}^j$.

Setting $\hat{\mathbf{T}}^j = \int_{\Omega^j} \boldsymbol{\Pi}^{jT} \boldsymbol{\Pi}^j d\Omega$ and accounting for (38), Eq. (41) becomes:

$$\hat{\boldsymbol{\varepsilon}}^j = \left(\hat{\mathbf{T}}^j \right)^{-1} \int_{\Omega^j} \boldsymbol{\Pi}^{jT} \left(\mathbf{L}_{\bar{\boldsymbol{\varepsilon}}}^j \bar{\boldsymbol{\varepsilon}} + \sum_{i=1}^n \mathbf{L}_{\boldsymbol{\pi}^i}^j \boldsymbol{\pi}^i \right) d\Omega. \quad (42)$$

Substituting equations (34), (39), (42) into equation (31) referred to the subset Ω^j , it results:

$$\begin{aligned} \mathbf{S}^j \hat{\boldsymbol{\sigma}}^j - [\bar{\mathbf{P}}^{jT} + \mathbf{J}^j] \bar{\boldsymbol{\varepsilon}} - \int_{\Omega^j} \left[\mathbf{P}^{jT} \boldsymbol{\Pi}^j \hat{\mathbf{T}}^{j-1} \int_{\Omega^j} \boldsymbol{\Pi}^{jT} \sum_{i=1}^n \mathbf{L}_{\boldsymbol{\pi}^i}^j \boldsymbol{\pi}^i d\Omega \right] d\Omega + \\ + \int_{\Omega^j} \mathbf{P}^{jT} \boldsymbol{\pi}^j d\Omega = \mathbf{o}, \end{aligned} \quad (43)$$

where it has been set:

$$\begin{aligned} \mathbf{S}^j &= \int_{\Omega^j} \mathbf{P}^{jT} \mathbf{C}^{-1} \mathbf{P}^j d\Omega, \\ \bar{\mathbf{P}}^j &= \int_{\Omega^j} \mathbf{P}^j d\Omega, \\ \mathbf{J}^j &= \int_{\Omega^j} \left[\mathbf{P}^{jT} \boldsymbol{\Pi}^j \hat{\mathbf{T}}^{j-1} \int_{\Omega^j} \boldsymbol{\Pi}^{jT} \mathbf{L}_{\bar{\boldsymbol{\varepsilon}}}^j d\Omega \right] d\Omega. \end{aligned} \quad (44)$$

The \mathbf{S}^j matrix in Eq. (43) can be interpreted as the inverse of the overall constitutive law for the subset Ω^j on the basis of the introduced stress approximation, so that the term $\mathbf{S}^j \hat{\boldsymbol{\sigma}}^j$ represents an overall elastic strain in Ω^j ; \mathbf{J}^j localizes the average strain $\bar{\boldsymbol{\varepsilon}}$ in Ω^j , responsible for the total strain in the subset, and the third term depends on the inelastic strain and represents a contribution to the total strain. The last term of Eq. (43) is the overall inelastic strain in the subset Ω^j .

3.1.1 Numerical procedure

In order to solve the evolution problem, a time-integration technique has to be implemented. In particular, the backward Euler algorithm is adopted. The quantities at previous time t_n are denoted with the subscript n , while the quantities at the current time t have no subscript; the time interval $t - t_n$ is denoted as Δt .

At each time step, the solution of the evolution problem is performed by establishing a specific predictor-corrector strategy. A trial state is determined considering the internal variables as frozen. In particular a trial value of $q^{j,TR}$ is computed so that a trial plastic multiplier $\Delta\gamma^{j,TR}$ can be evaluated solving the time discretized form of its evolution equation. If $\Delta\gamma^{j,TR}$ is equal to zero in all the subsets, the trial state is the solution of the elastic step; otherwise a corrector phase is required. In this case the evolution of modified plastic multiplier in the time step interval occurs, leading to $\Delta\gamma^j > 0$; thus, the inelastic strain field evaluated at the current time step t , is obtained as:

$$\begin{aligned}\boldsymbol{\pi}^j &= \boldsymbol{\pi}_n^j + \Delta\hat{\gamma}^j \mathbf{T}^j \hat{\boldsymbol{\sigma}}^j \\ &= \mathbf{T}^j \left(\boldsymbol{\beta}^j + \Delta\hat{\gamma}^j \hat{\boldsymbol{\sigma}}^j \right),\end{aligned}\quad (45)$$

$$\alpha^j = \int_0^t \dot{\alpha}^j d\tau, \quad (46)$$

being $\boldsymbol{\pi}_n^j$ the inelastic strain at t_n and the components vector $\boldsymbol{\beta}^j$ defined as:

$$\boldsymbol{\beta}^j = \sum_{\tau=0}^{t_n} \Delta\hat{\gamma}_\tau^j \hat{\boldsymbol{\sigma}}_\tau^j, \quad (47)$$

representing the history variables of the problem for subset Ω^j , together with the hardening variable α^j . The residual form of equation (43) and the weak form of the evolution of γ^j integrated over the time step and defined as \mathbf{R}_σ^j and \mathbf{R}_γ^j respectively are:

$$\begin{aligned}\mathbf{R}_\sigma^j &= \mathbf{S}^j \hat{\boldsymbol{\sigma}}^j - [\hat{\mathbf{P}}^{jT} + \mathbf{J}^j] \bar{\boldsymbol{\varepsilon}} + \\ &+ \hat{\mathbf{P}}^j \left(\boldsymbol{\beta}^j + \Delta\hat{\gamma}^j \hat{\boldsymbol{\sigma}}^j \right) - \sum_{i=1}^n \mathbf{K}^{ij} \left(\boldsymbol{\beta}^i + \Delta\hat{\gamma}^i \hat{\boldsymbol{\sigma}}^i \right)\end{aligned}\quad (48)$$

$$\mathbf{R}_\gamma^j = \mathbf{R}_\gamma^j(\widehat{\boldsymbol{\sigma}}^j, \Delta\widehat{\boldsymbol{\gamma}}^j) \quad (49)$$

with:

$$\begin{aligned} \widehat{\mathbf{P}}^j &= \int_{\Omega^j} \mathbf{P}^\top \mathbf{T} \, d\Omega \\ \mathbf{K}^{ij} &= \int_{\Omega^j} \left[\mathbf{P}^\top \boldsymbol{\Pi} \widehat{\mathbf{T}}^{-1} \int_{\Omega^j} \boldsymbol{\Pi}^\top \mathbf{L}_{\pi^i}^j \mathbf{T} \, d\Omega \right] d\Omega. \end{aligned} \quad (50)$$

The explicit expression for \mathbf{R}_γ^j in (49) is detailed in 3.2 and 3.3.

The correction phase consists in solving the nonlinear system of $(\sum_{j=1}^n N_p^j + n)$ equations (48) and (49) with respect to the unknowns $\widehat{\boldsymbol{\sigma}}^j$ and $\Delta\widehat{\boldsymbol{\gamma}}^j$ defined on each subset, since they are the only information that is required in order to recover the material state at a given time step. At the end of each time step, the stress and plastic multiplier parameters allow for the recovery of the stress and inelastic strain field according to Eqs. (45) and (47). The residual and the unknown vectors for Ω^j are defined as $\mathbf{R}^j = \left\{ \left(\mathbf{R}_\sigma^j \right)^\top \quad \mathbf{R}_\gamma^j \right\}^\top$ and $\mathbf{U}^j = \left\{ \left(\widehat{\boldsymbol{\sigma}}^j \right)^\top \quad \Delta\widehat{\boldsymbol{\gamma}}^j \right\}^\top$ respectively, so that the full residual and unknown vectors for the whole RVE result:

$$\mathbf{R} = \left\{ \left(\mathbf{R}^1 \right)^\top \quad \left(\mathbf{R}^2 \right)^\top \quad \dots \quad \left(\mathbf{R}^n \right)^\top \right\}^\top \quad (51)$$

and

$$\mathbf{U} = \left\{ \left(\mathbf{U}^1 \right)^\top \quad \left(\mathbf{U}^2 \right)^\top \quad \dots \quad \left(\mathbf{U}^n \right)^\top \right\}^\top. \quad (52)$$

A Newton-Raphson technique is adopted to solve the nonlinear problem $\mathbf{R} = \mathbf{o}$, so that at the typical $[p + 1]$ iteration, the following linearized problem has to be solved:

$$\mathbf{R}^{[p]} + \left. \frac{\partial \mathbf{R}}{\partial \mathbf{U}} \right|_{[p]} \delta \mathbf{U} = \mathbf{o}, \quad (53)$$

with $\delta \mathbf{U}$ the variation of the whole unknown vector arising between two consecutive iterations. The explicit form of the tangent matrix, whose dimension is $(\sum_{j=1}^n N_p^j + n) \times (\sum_{j=1}^n N_p^j + n)$, takes the following form at the $[p]$ -th iteration :

$$\frac{\partial \mathbf{R}}{\partial \mathbf{U}} = \begin{bmatrix} \frac{\partial \mathbf{R}^1}{\partial \mathbf{U}^1} & \frac{\partial \mathbf{R}^1}{\partial \mathbf{U}^2} & \dots & \frac{\partial \mathbf{R}^1}{\partial \mathbf{U}^n} \\ \frac{\partial \mathbf{R}^2}{\partial \mathbf{U}^1} & \frac{\partial \mathbf{R}^2}{\partial \mathbf{U}^2} & \dots & \frac{\partial \mathbf{R}^2}{\partial \mathbf{U}^n} \\ \dots & \dots & \dots & \dots \\ \frac{\partial \mathbf{R}^n}{\partial \mathbf{U}^1} & \frac{\partial \mathbf{R}^n}{\partial \mathbf{U}^2} & \dots & \frac{\partial \mathbf{R}^n}{\partial \mathbf{U}^n} \end{bmatrix}. \quad (54)$$

where the expression of the generic component is given by:

$$\frac{\partial \mathbf{R}^j}{\partial \mathbf{U}^i} = \begin{bmatrix} \frac{\partial \mathbf{R}_\sigma^j}{\partial \hat{\boldsymbol{\sigma}}^i} & \frac{\partial \mathbf{R}_\sigma^j}{\partial \Delta \hat{\boldsymbol{\gamma}}^i} \\ \frac{\partial \mathbf{R}_\gamma^j}{\partial \hat{\boldsymbol{\sigma}}^i} & \frac{\partial \mathbf{R}_\gamma^j}{\partial \Delta \hat{\boldsymbol{\gamma}}^i} \end{bmatrix}, \quad (55)$$

Of course, the derivatives are only calculated in the j -th subset if it is actually active. The iterations will stop when the norm of the residual vector, suitably normalized, is lower than a prefixed tolerance.

Once all the unknowns are updated, the average stress in the whole RVE is computed. Thanks to the stress approximation introduced in (34), this can be achieved straightforward as:

$$\bar{\boldsymbol{\sigma}} = \frac{1}{\Omega} \sum_{j=1}^n \bar{\mathbf{P}}^j \hat{\boldsymbol{\sigma}}^j. \quad (56)$$

Note that the stress distribution could be also evaluated from the constitutive equation involving the total and plastic strain fields. However, as usual in mixed stress approaches, higher accuracy in the stress evaluation can be obtained if it is evaluated directly from the stress parameters, as shown in 3.3.4.1.

The algorithm is summarized in Box 1. In addition, a summary of the proposed procedure is shown in Fig. 8.

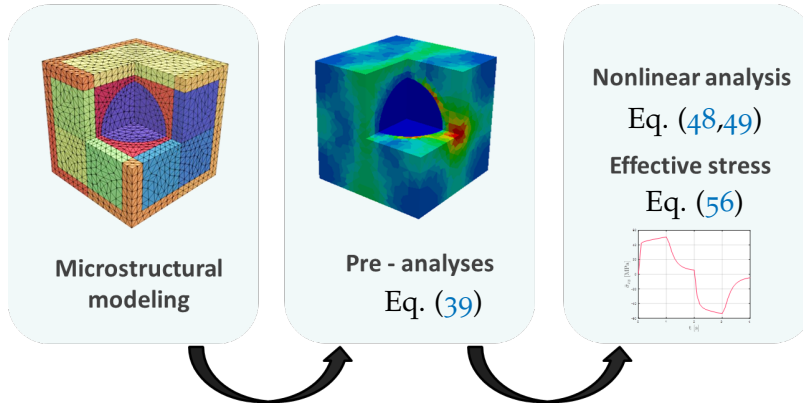


Figure 8: MXTFA: Graphical representation of the procedure.

3.2 MXTFA IN ELASTO-PLASTICITY

3.2.1 Homogenization in elasto-plasticity

In a plasticity framework the evolution laws for the internal variables are:

$$\dot{\boldsymbol{\pi}} = \dot{\lambda} \mathbf{N} \quad (58)$$

$$\dot{\boldsymbol{\alpha}} = \dot{\lambda}. \quad (59)$$

Algorithm 1 Integration algorithm for the elastic predictor.

1. Assign a new value of $\bar{\epsilon}$
2. Given the history variables β^j at time t_n , computed by equation (47), evaluate the elastic predictor state in each subset Ω^j from equations (48):

$$\hat{\sigma}^{j\text{TR}} = \mathbf{S}^{j-1} \left\{ [(\hat{\mathbf{P}}^j)^T + \mathbf{J}^j] \bar{\epsilon} + \hat{\mathbf{P}}^j \beta^j - \sum_{i=1}^n \mathbf{K}^{ij} \beta^i \right\}$$

3. Check for admissibility of the trial state at the subset:

$$\int_{\Omega^j} \delta \gamma^j f(\hat{\sigma}^{j\text{TR}}) d\Omega \leq 0, \quad (57)$$

if $\Delta \gamma^{j,\text{TR}} = 0$ for all the subsets \implies the trial state is the solution

else

- a) Compute the residuals $\mathbf{R}^{[p]}$ at iteration p from equations (48) and (49)
- b) if $\|\mathbf{R}^{[p]}\| > \text{TOL}$, where $\|\mathbf{R}^{[p]}\|$ is the L^2 norm of $\mathbf{R}^{[p]}$
 - compute the tangent $\partial \mathbf{R} / \partial \mathbf{U}$, as defined in (54) to get $\delta \mathbf{U}$ from (53)
 - update $\mathbf{U}^{[p+1]} = \mathbf{U}^{[p]} + \delta \mathbf{U}$, set $p = p + 1$ and go to step 3(a)
- c) else
 - update the variables

4. Continue
-

Note that here α can be interpreted as a non negative plastic multiplier [62]. The above equations are completed with the loading-unloading Kuhn-Tucker conditions:

$$f(\boldsymbol{\sigma}, r) \leq 0, \quad \dot{\lambda} \geq 0, \quad f(\boldsymbol{\sigma}, r) \dot{\lambda} = 0. \quad (60)$$

Concerning the plasticity model, the classical Mises yield function is considered in the framework of associate plasticity [63]. In this case, the limit function is:

$$f(\boldsymbol{\sigma}, r) = q - \tilde{\sigma}_y \quad \text{with} \quad q = \sqrt{\frac{3}{2} \boldsymbol{\sigma}^T \mathbf{M} \boldsymbol{\sigma}} = \sqrt{\frac{3}{2}} \|\boldsymbol{\sigma}'\|, \quad (61)$$

where q is the von Mises stress, $\boldsymbol{\sigma}'$ the deviatoric part of the stress fields, while:

$$\mathbf{M} = \frac{1}{3} \begin{bmatrix} 2 & -1 & -1 & 0 & 0 & 0 \\ -1 & 2 & -1 & 0 & 0 & 0 \\ -1 & -1 & 2 & 0 & 0 & 0 \\ 0 & 0 & 0 & 6 & 0 & 0 \\ 0 & 0 & 0 & 0 & 6 & 0 \\ 0 & 0 & 0 & 0 & 0 & 6 \end{bmatrix},$$

and $\tilde{\sigma}_y = \sigma_y + r$, being σ_y the initial yield stress. From Eqs. (32) and (61) it results:

$$\mathbf{N}(\boldsymbol{\sigma}) = \frac{3}{2q} \mathbf{M} \boldsymbol{\sigma}. \quad (62)$$

The modified plastic multiplier γ will be defined as:

$$\dot{\gamma} = \frac{1}{2q} \dot{\alpha}, \quad (63)$$

so that equation (32) can be rewritten as (considering Eq. (63)):

$$\dot{\boldsymbol{\pi}} = \dot{\gamma} 3 \mathbf{M} \boldsymbol{\sigma}. \quad (64)$$

The loading-unloading Kuhn-Tucker equations (60) are also restated in a weak form:

$$\int_{\Omega} \delta\gamma f(\boldsymbol{\sigma}, \gamma) d\Omega \leq 0, \quad \dot{\gamma} \geq 0, \quad \int_{\Omega} \delta\gamma f(\boldsymbol{\sigma}, \gamma) \dot{\gamma} d\Omega = 0 \quad \forall \delta\gamma \geq 0. \quad (65)$$

3.2.2 Computational homogenization technique

The RVE is subdivided into subsets according to (33). On each subset Ω^j the stress and the modified plastic multiplier are defined according to (34) and (36). On the basis of the introduced approximations,

the weak form of the loading-unloading Kuhn-Tucker equations (60) for the subset Ω^j reads as:

$$\int_{\Omega^j} \delta \hat{\gamma}^j f \, d\Omega \leq 0, \quad \hat{\gamma}^j \geq 0, \quad \int_{\Omega^j} \hat{\gamma}^j f \hat{\gamma} \, d\Omega = 0 \quad \forall \delta \hat{\gamma}^j \geq 0. \quad (66)$$

where f is defined according to (61) as:

$$f(\hat{\boldsymbol{\sigma}}^j, \hat{\gamma}^j) = \int_{\Omega^j} \left(\sqrt{\frac{3}{2}} (\hat{\boldsymbol{\sigma}}^j)^\top \mathbf{Q}^j \hat{\boldsymbol{\sigma}}^j - \hat{\sigma}_y^j \right) d\Omega \quad (67)$$

with $\mathbf{Q}^j = (\mathbf{P}^j)^\top \mathbf{M} \mathbf{P}^j$.

Equation (64) in the subset Ω^j takes the specific form:

$$\boldsymbol{\pi}^j = \hat{\gamma}^j \mathbf{T}^j \hat{\boldsymbol{\sigma}}^j, \quad (68)$$

being $\mathbf{T}^j = 3 \mathbf{M} \mathbf{P}^j$. The evolution problem is solved employing the backward Euler algorithm described in 3.1.1. If the trial stress satisfies the yield condition, the trial state is the solution of the elastic step; otherwise a corrector phase is required. In this case the evolution of plastic multiplier occurs, leading to $\Delta \gamma^j \neq 0$; the nonlinear system (51) needs to be solved, where R_γ^j is the first of (65) written in the equality residual form:

$$R_\gamma^j = \int_{\Omega^j} \left(\sqrt{\frac{3}{2}} (\hat{\boldsymbol{\sigma}}^j)^\top \mathbf{Q}^j \hat{\boldsymbol{\sigma}}^j - \hat{\sigma}_y^j \right) d\Omega \quad (69)$$

and its derivatives are:

$$\frac{\partial R_\gamma^j}{\partial \hat{\boldsymbol{\sigma}}^i} = \delta_{ij} \int_{\Omega^j} \frac{\partial q^j}{\partial \hat{\boldsymbol{\sigma}}^j} (1 - 2H\Delta \hat{\gamma}^j) \, d\Omega \quad (70)$$

$$\frac{\partial R_\gamma^j}{\partial \Delta \hat{\gamma}^i} = \delta_{ij} \int_{\Omega^j} (-2Hq^j) \, d\Omega, \quad (71)$$

being δ_{ij} Kronecker's delta and

$$\frac{\partial q^j}{\partial \hat{\boldsymbol{\sigma}}^i} = \frac{3\delta_{ij}}{2} \frac{\mathbf{Q}^j \hat{\boldsymbol{\sigma}}^j}{\left[\frac{3}{2} (\hat{\boldsymbol{\sigma}}^j)^\top \mathbf{Q}^j \hat{\boldsymbol{\sigma}}^j \right]^{\frac{1}{2}}}. \quad (72)$$

The hardening variable of the subset α^j , using (46) and (63) is determined as:

$$\alpha^j = \alpha_n^j + 2\Delta \hat{\gamma}^j \int_{\Omega^j} q^j \, d\Omega, \quad (73)$$

being α_n^j the accumulated plastic strain at t_n .

The $(N_p^j + 1)$ equations (48) and (69) have to be solved with respect to the $(N_p^j + 1)$ unknowns $\hat{\boldsymbol{\sigma}}^j$ and $\Delta \hat{\gamma}^j$. The average stress in the whole RVE is computed using the representation form (34) via (56).

3.2.3 Numerical Results

In this section, the performance of the proposed homogenization procedure in the framework of elasto-plasticity is verified on two numerical tests involving periodic composites. Thanks to the properties of periodicity of their microstructure, the overall behavior of periodic composites can be analyzed by considering a repetitive UC, subjected to periodic boundary conditions. In particular, for a rectangular UC of dimensions $2a_1 \times 2a_2$, considering a Cartesian coordinate system (x_1, x_2) placed at the center of it, the periodic boundary conditions are:

$$\begin{aligned}
 \tilde{u}_1(a_1, x_2) &= \tilde{u}_1(-a_1, x_2) & \forall x_2 \in (-a_2, a_2) \\
 \tilde{u}_2(a_1, x_2) &= \tilde{u}_2(-a_1, x_2) & \forall x_2 \in (-a_2, a_2) \\
 \tilde{u}_1(x_1, a_2) &= \tilde{u}_1(x_1, -a_2) & \forall x_1 \in (-a_1, a_1) \\
 \tilde{u}_2(x_1, a_2) &= \tilde{u}_2(x_1, -a_2) & \forall x_1 \in (-a_1, a_1)
 \end{aligned} \tag{74}$$

The MxTFA procedure is implemented into a Fortran program, and a linear stress approximation is assumed on all the subsets, resulting in $N_p = 7$ stress modes (and therefore inelastic modes), collected in the stress matrix \mathbf{P} defined as:

$$\mathbf{P}^j = \begin{bmatrix} 1 & 0 & 0 & x_2 & 0 & x_1 & 0 \\ 0 & 1 & 0 & 0 & x_1 & 0 & x_2 \\ 0 & 0 & 1 & 0 & 0 & -x_2 & -x_1 \end{bmatrix}. \tag{75}$$

The localization matrices $\mathbf{L}_{\bar{\varepsilon}}^j$ and $\mathbf{L}_{\pi^i}^j$ employed in the MxTFA are evaluated performing linear elastic Finite Element Analysis (FEA) of the UC subjected to each component of $\bar{\varepsilon}$ and of π^i , respectively, determining the perturbation strain at each Gauss point of the finite element mesh. In particular, 2D plane stress four-node finite elements are implemented into FEAP code. The level of refinement of the finite element mesh has been chosen so that the convergence of the FEA solution is ensured. The number of pre-analyses is equal to the 3 components of $\bar{\varepsilon}$ plus the number of the subsets times the 7 components of $\hat{\sigma}^j$. Furthermore, the matrices defined in (44) are evaluated through numerical integration on the same finite element mesh used for the pre-analyses. Note that the numerical integration could be not strictly necessary in case of simple-shaped subdomains, but when dealing with complex shapes then numerical integration becomes necessary. For sake of uniformity, in this work numerical integration for every matrix is employed.

In the first test, a UC with a simple geometry is considered and the proposed procedure is applied adopting an increasing number of

inelastic subsets in order to highlight its convergence properties. In the second test, a UC with a more complex geometry, representative of a realistic application, is considered. In both tests, the responses under uniaxial and biaxial loadings are analyzed.

The results obtained with the homogenization procedure are compared with nonlinear micromechanical analyses (FEA), carried out using 2D plane stress four-node quadrilateral finite elements, characterized by elastic and plastic constitutive models.

3.2.3.1 Test 1 - UC with rectangular inclusion

A periodic heterogeneous material characterized by a plastic matrix and elastic rectangular inclusions is considered. Because of the double symmetry of the UC only one quarter is considered in the following, as shown in Fig. 9. Unit thickness is assumed and the geometrical parameters are set as follows: $a_1 = 15$ mm, $a_2 = 9$ mm, $b_1 = 5$ mm and $b_2 = 4$ mm, resulting in a volume fraction equal to 15%. The mechanical properties of the constituents are summarized in Table 1, where E and ν are the Young modulus and the Poisson ratio respectively. Both for the elastic pre-analyses and for the nonlinear micromechanical analysis, the quarter of the UC is discretized with a regular mesh composed by 180 finite elements, 150 for the matrix and 30 for the inclusion.

As only loading conditions prescribing average strains $\bar{\epsilon}_{11}$ and $\bar{\epsilon}_{22}$ are considered in the following computations, the periodic boundary conditions (74) for the quarter of UC become:

$$\begin{aligned} \tilde{u}_1(0, x_2) &= 0 & \forall x_2 \in (0, a_2) \\ \tilde{u}_1(a_1, x_2) &= 0 & \forall x_2 \in (0, a_2) \\ \tilde{u}_2(x_1, 0) &= 0 & \forall x_1 \in (0, a_1) \\ \tilde{u}_2(x_1, a_2) &= 0 & \forall x_1 \in (0, a_1). \end{aligned} \tag{76}$$

The homogenization analyses are carried out considering three different subsets discretization, shown in Fig. 10. It can be noted that always one subset is used for the elastic inclusion, while the matrix is subdivided into 3, 5 and 7 subsets, resulting, respectively, in $3 \times 8 = 24$, $5 \times 8 = 40$ and $7 \times 8 = 56$ internal variables of the MxTFA procedure. In fact, for each subset the 7 components of the vector β^j and $\Delta\gamma$ represent the internal variables of the elasto-plastic problem. In the micromechanical nonlinear finite element analysis, the number of internal variables, considering 4 Gauss points for each finite element 3 components of the plastic strain and the accumulated plastic strain, it results $150 \times 4 \times 4 = 2400$, which is significantly higher than the one of the MxTFA.

Constituent	E [MPa]	ν	σ_y [MPa]	H [GPa]
Inclusion (elastic material)	25000	0.15	-	-
Matrix (plastic material)	2500	0.15	3	0

Table 1: Test 1 - Material properties of the constituents.

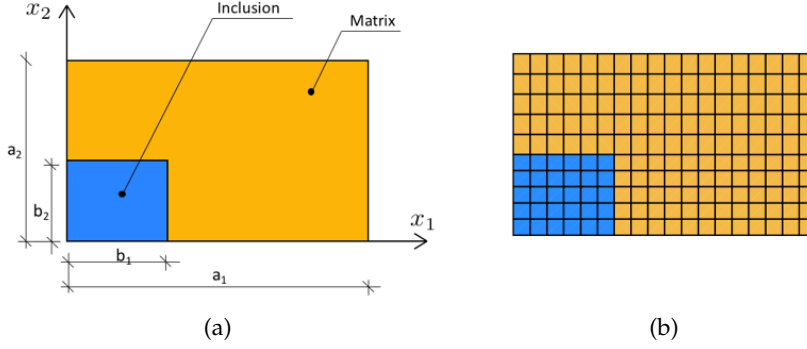


Figure 9: Test 1 - (a) Geometry of the UC, (b) UC FE discretization.

LOADING ALONG THE x_1 -AXIS The response of the UC subjected to uniaxial loading along the x_1 -direction is analyzed. In particular, a monotonic increasing value of the average strain $\bar{\epsilon}_{11}$ is prescribed until it reaches the value $\bar{\epsilon}_{11} = 0.005$.

The overall responses of the UC obtained with the MxTFA using the three different subsets discretization are shown in Fig. 11 in terms of average stress $\bar{\sigma}_{11}$ versus average strain $\bar{\epsilon}_{11}$. For comparison, the UC reference response, obtained from the nonlinear micromechanical finite element analysis, is also reported. Moreover, the percentage errors on the average stress $\bar{\sigma}_{11}$ at the end of the analysis (i.e. when the average deformation $\bar{\epsilon}_{11}$ reaches its final value), are collected in Table 2.

The MxTFA is able to reproduce the constitutive response of the UC characterized by nonlinear behavior and there is a very good agreement between the MxTFA predictions and the micromechanical reference solution. In particular, it can be observed that only 4 subsets suffices to achieve very good accuracy with an error of only 1.14%

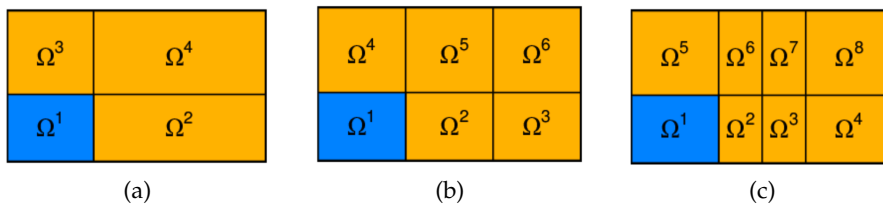


Figure 10: Test 1 - Subset subdivision: (a) 4 subsets, (b) 6 subsets, (c) 8 subsets.

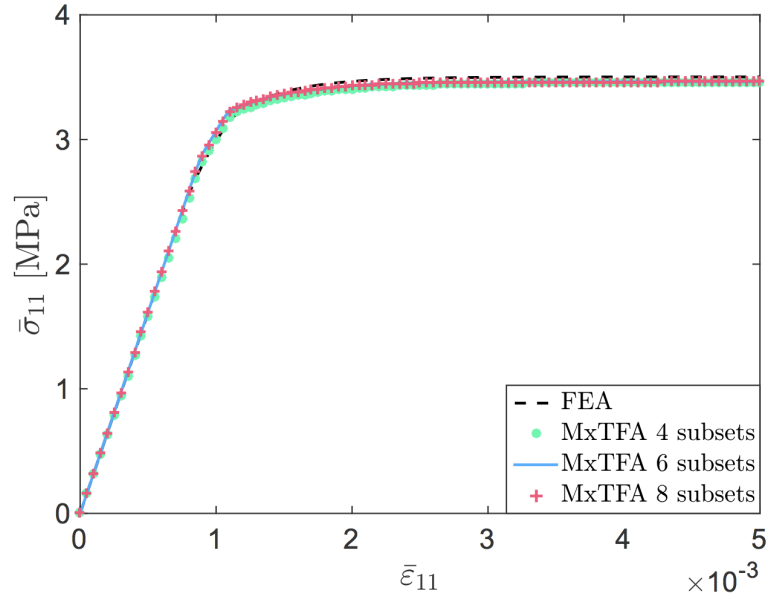


Figure 11: Test 1 - Mechanical response of the UC subjected to uniaxial loading.

Type of analysis	$\bar{\sigma}_{11}$ (MPa)	Error (%)
FEA	3.502	-
MxTFA (4 subsets)	3.461	1.184
MxTFA (6 subsets)	3.463	1.102
MxTFA (8 subsets)	3.464	1.093

Table 2: Test 1 - Uniaxial loading: final value of the average stress.

in the evaluation of the average stress $\bar{\sigma}_{11}$ at the end of the analysis. Finally, as expected, increasing the number of subsets results in an improvement in accuracy.

BIAXIAL LOADING The same UC is loaded in the x_1 - and x_2 - direction, by prescribing the axial strains $\bar{\epsilon}_{11}$ and $\bar{\epsilon}_{22}$ until the value $\bar{\epsilon}_{11} = \bar{\epsilon}_{22} = 0.005$ is reached, keeping the ratio $\bar{\epsilon}_{11}/\bar{\epsilon}_{22} = 1$ for the whole analysis. As in the previous case, the subsets configurations showed in Fig. 10 are considered, and the MxTFA results are compared with the micromechanical finite elements analysis. In particular, the overall response of the UC obtained with the MxTFA is shown in Fig. 12a in terms of the average normal stresses $\bar{\sigma}_{11}$ versus the average normal strains $\bar{\epsilon}_{11}$, and in Fig. 12b in terms of the average normal stresses $\bar{\sigma}_{22}$ versus the average normal strains $\bar{\epsilon}_{22}$. Moreover, Table 3 collects the results in terms of the average normal stresses $\bar{\sigma}_{11}$ and $\bar{\sigma}_{22}$ obtained at the end of the analyses. The above results show that the MxTFA is able to accurately predict the mechanical behavior of the UC along the two directions, with very good agreement with the reference FEA

Type of analysis	$\bar{\sigma}_{11}$ (MPa)	Error (%)	$\bar{\sigma}_{22}$ (MPa)	Error (%)
FEA	3.142	-	3.120	-
MxTFA (4 subsets)	3.173	0.98	3.183	2.01
MxTFA (6 subsets)	3.165	0.73	3.143	0.72
MxTFA (8 subsets)	3.164	0.70	3.120	0.02

Table 3: Test 1 - Biaxial loading: final value of the average stresses in x_1 - and x_2 -direction.

solution. Stress estimates are more accurate in the x_1 -direction for the 4 subset analysis, while increasing the subset number a very good approximation is achieved also along x_2 -direction.

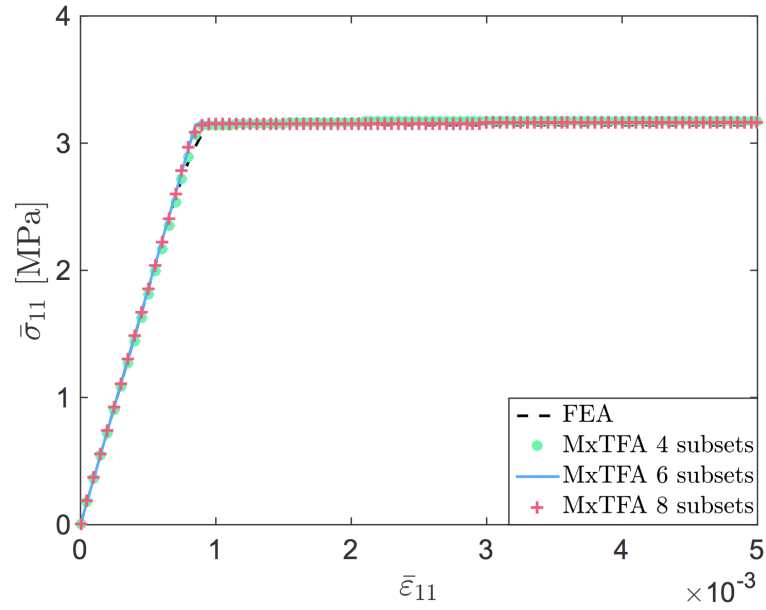
3.2.3.2 Test 2 - UC with circular inclusion

In this test, the behavior of a periodic composite consisting of a plastic matrix embedding elastic circular inclusions with volume fraction equal to 36% is analyzed. The UC geometry is shown in Fig. 13a; due to symmetry only one quarter of the UC is modeled considering the boundary conditions (76). The following geometrical parameters are assumed: $a = 0.5$ mm and $r = 0.34$ mm. The material parameters are collected in Table 4. Two different UCs were considered, in which the matrix was characterized by an elasto perfectly plastic behavior and by linear isotropic hardening respectively. The MxTFA homogenization analyses are performed discretizing the UC with 7 subsets (6 subsets for the matrix and 1 subset for the inclusion), as shown Fig. 13b, resulting in $6 \times 8 = 48$ internal variables. For the finite element model employed to perform the linear elastic pre-analyses and to compute the micromechanical reference solution, the quarter of UC has been discretized using 304 finite elements, 176 for the matrix and 128 for the inclusion. The internal variables of the nonlinear micromechanical analysis are equal to $176 \times 4 \times 4 = 2816$, significantly higher than the ones of the MxTFA.

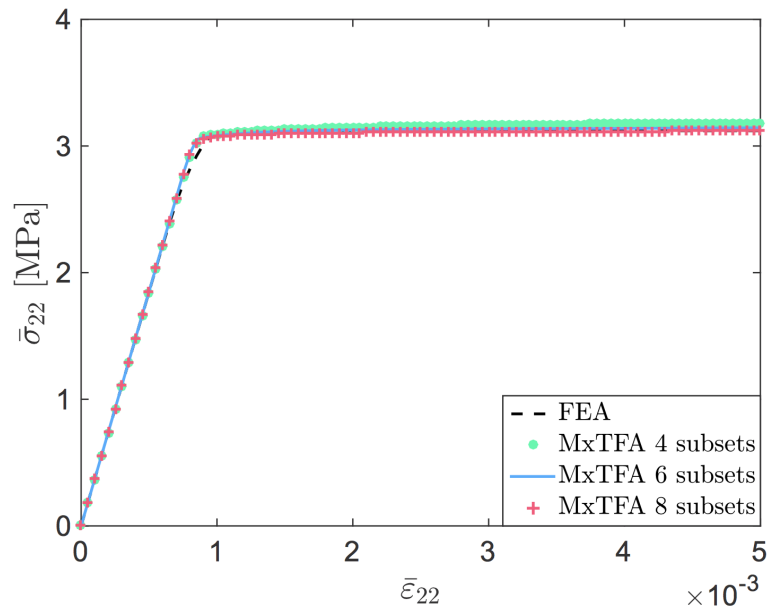
Constituent	E [GPa]	ν	σ_y [MPa]	H [GPa]
Inclusion (elastic material)	410	0.19	-	-
Matrix (plastic material)	75	0.33	426	2.894

Table 4: Material properties of the constituents.

LOADING ALONG THE x_1 -AXIS The UC is subjected to uniaxial loading along the x_1 -axis, with the average strain $\bar{\epsilon}_{11}$ monotonically increased until the final value $\bar{\epsilon}_{11} = 0.03$. Fig. 14 shows the constitutive response in both cases of elasto perfectly plastic and Linear



(a)



(b)

Figure 12: Test 1 - Mechanical response of the UC subjected to biaxial loading: (a) mechanical response in x_1 -direction, (b) mechanical response in x_2 -direction.

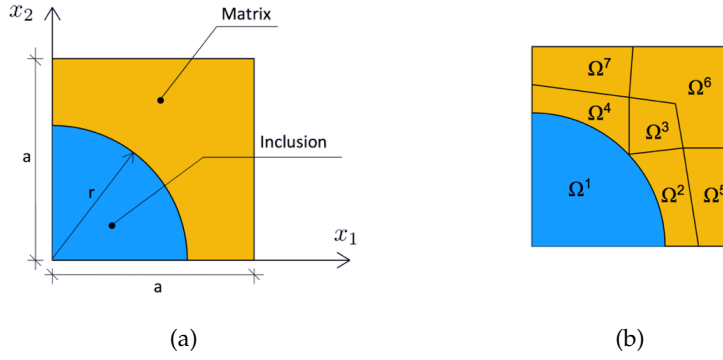


Figure 13: Test 2 - Geometry of the UC (a) and subset discretization (b)

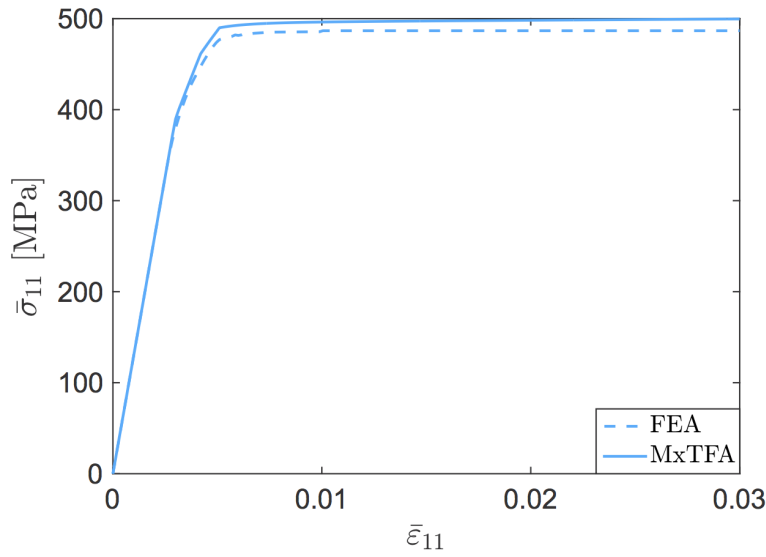


Figure 14: Test 2 - Mechanical response of the UC subjected to uniaxial loading.

Hardening (LH) of the equivalent homogenized material in terms of $\bar{\sigma}_{11}$ and $\bar{\epsilon}_{11}$, together with the micromechanical reference solution. The MxTFA is able to accurately reproduce the overall behavior of the UC also in this case. Moreover, the final value of the average stress $\bar{\sigma}_{11}$ obtained with the MxTFA is compared with the reference one deriving from the micromechanical analysis in Table 5; as it can be noted, the error is less than 3%.

BIAXIAL LOADING The UC is subjected to a biaxial tensile loading along x_1 - and x_2 -axis, with increasing prescribed axial deformations that reach the final value of $\bar{\epsilon}_{11} = \bar{\epsilon}_{22} = 0.03$, while keeping a constant unitary ratio $\bar{\epsilon}_{11}/\bar{\epsilon}_{22}$. For this load case, only the results for the elasto perfectly plastic material are reported. Fig. 15 shows the overall behavior of the UC in terms of average stress and average strain in x_1 -direction, and Table 6 reports the error on the final value of the

Type of analysis	$\bar{\sigma}_{11}$ (MPa)	Error (%)
FEA	492.01	-
MxTFA	499.66	0.98
FEA LH	681.36	-
MxTFA LH	697.53	2.37

Table 5: Uniaxial loading: final value of the average stress.

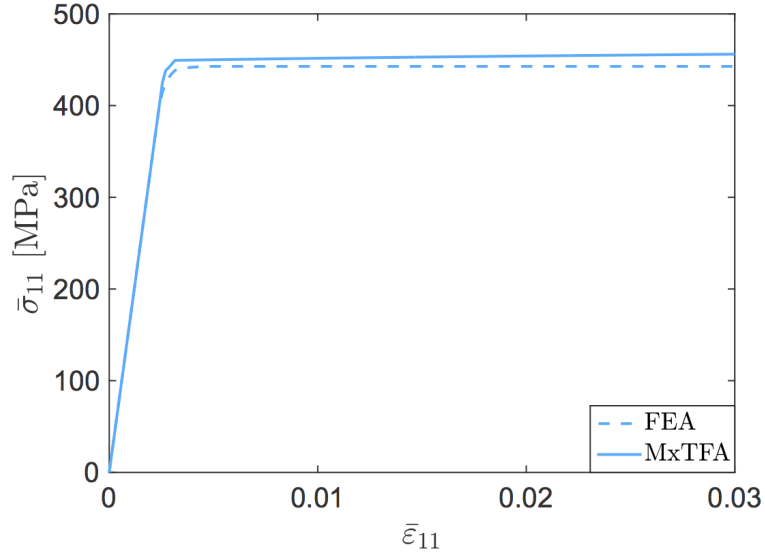


Figure 15: Test 2 - Mechanical response of the UC subjected to biaxial loading.

average stress. The results confirm the very good performance of the proposed homogenization procedure.

NO. SUBSETS VS NO. MODES For this test, a study concerning the influence of the number of subsets and the number of inelastic modes on the accuracy of the solution is performed. According to Fig. 16, four different subsets configurations are analyzed, and for each configuration first linear (LIN) then quadratic (QUAD) stress approximations are considered for each subset, resulting in 7 and 12 inelastic modes respectively. Table 7 collects information on the homogenization analyses performed. A deviatoric strain history of tension and

Type of analysis	$\bar{\sigma}_{11}=\bar{\sigma}_{22}$ (MPa)	Error (%)
FEA	442.74	-
MxTFA	456.06	3.01

Table 6: Test 2 - Biaxial loading: final value of the average stress.

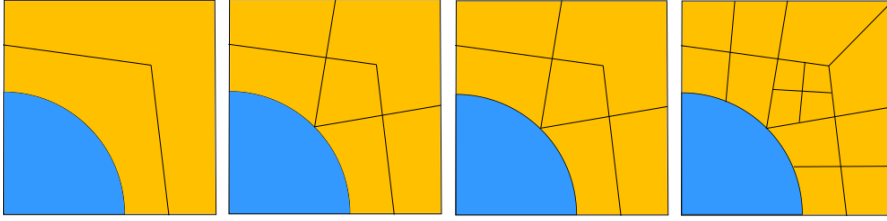


Figure 16: Test 2 - Subsets configurations.

Analysis	No. of subsets n	No. of modes N_p	No. of internal variables \bar{N}
FEA	-	-	704
3 LIN	3	7	16
3 QUAD	3	12	26
4 LIN	4	7	24
4 QUAD	4	12	39
7 LIN	7	7	48
7 QUAD	7	12	78
15 LIN	15	7	112
15 QUAD	15	12	182

Table 7: Test 2 - Homogenization analyses: final value of the average stress.

compression along x_1 and x_2 — direction respectively is applied to the UC. Fig. 17 shows a comparison of the results obtained via MxTFA and FEA. As expected, better results are obtained increasing n , and, for fixed n , higher accuracy is achieved increasing the number of modes N_p . It can be observed that both 3 LIN and 3 QUAD are not able to provide accurate results even if the total number of internal variables \bar{N} for 3 QUAD and 4 LIN are comparable: this means that 3 subsets are not enough for this UC in order to provide good results. The results also show that for a comparable number of internal variables \bar{N} (e.g. considering 4 QUAD and 7 LIN), a higher number of subsets n is preferable to a higher number of modes N_p when plasticity is reached (region A in the Figure). On the other side, when the UC is fully plastic, a higher number of modes determines a more accurate solution than a higher number of subsets (region B in the Figure). Figure 18 shows the relative error on the final value of $\bar{\sigma}_{22}$ between FEA and MxTFA.

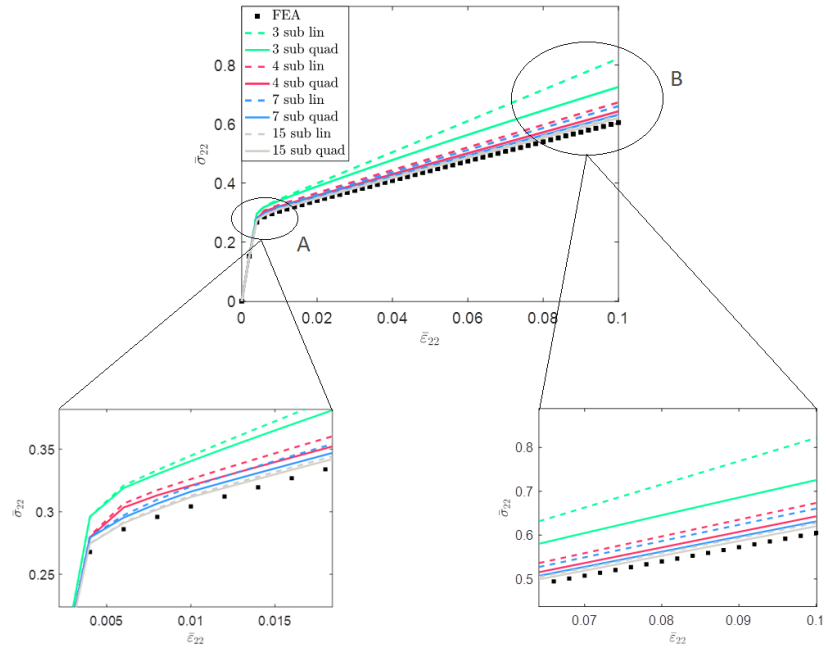
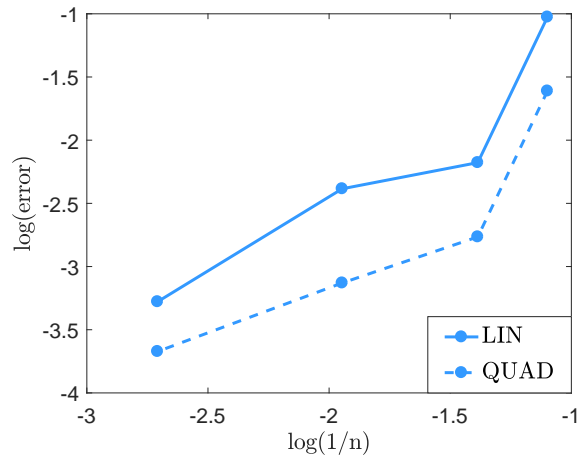
Figure 17: Test 2 - $\bar{\sigma}_{22}$ for the homogenization analyses.

Figure 18: Test 2 - Error convergence.

3.3 MXTFA IN VISCOPLASTICITY

Concerning the homogenization problem of viscoplastic composites, several techniques have been adopted in literature. Among the others, very recently, Czarnota et al. [15] presented a homogenization technique based on an additive tangent Mori–Tanaka scheme in order to study two-phase composites characterized by phases with nonlinear elastic–viscoplastic behavior and spherical inclusions. Mareau and Berbenni [44] presented a homogenization technique for heterogeneous elastic-viscoplastic materials based on the self-consistent approximation. Agoras et al. [3] presented an alternative technique of the incremental variational procedure of Lahellec and Suquet [43] considering a time-incremental variational formulation for the strain-rate potential of the elastic-viscoplastic composite and defining a homogenization problem with nonuniform “eigenstrain rates” in the phases. They adopted the variational procedure proposed in [56] to handle the nonlinearity and the heterogeneity of the properties in the phases.

This section is focused on the elastic-viscoplastic homogenization problem for composite materials. First, the constitutive model describing the elastic-viscoplastic behavior of the constituents is introduced and, then, the homogenization problem based on the MxTFA is presented.

3.3.1 *Elastic-viscoplastic constitutive model*

Viscoplasticity indicates a model where both rheologic and plastic effects are taken into account in order to describe the behavior of the material. In particular, a time dependence of the stress and strain state is introduced due to the viscous properties of the medium, while the plastic properties depend on the loading path. As a result, the model becomes both time and loading history dependent.

According to Perzyna [54], there are two different classes of viscoplastic materials: elasto-viscoplastic materials and elastic-viscoplastic materials. The former are the class of materials that show viscous properties in both elastic and plastic regions, while the latter exhibit viscous properties in the plastic region only. Here, this second class will be considered. The elastic-viscoplastic constitutive model is formulated assuming the existence of an elastic domain in which there are no viscous effects and of a dissipation potential, that governs the evolution of the internal variables .

Based on the assumption that the viscous properties manifest themselves only once the plastic state is reached, the strain rate can be split into an elastic and inelastic part, where the latter represents combined viscous and plastic effects. In addition, since the material does not show viscous properties in the elastic region, the classical Mises yield function is considered in the framework of associated plasticity [63].

In particular, an elastic perfectly plastic material is considered. The assumption of perfect plastic material is introduced only to get an easier formulation, but kinematic and/or isotropic hardening effects can be introduced in the procedure, i. e. the assumption of perfect plasticity is not strictly necessary for the proposed procedure. The initial yield condition (or static yield condition) is the one reported in Eq. (61) with $\tilde{\sigma}_y = \sigma_y$, i.e. $r = 0$.

Introducing a dissipation potential $\Phi^*(\sigma, r)$, the flow rule is given by deriving Φ^* with respect to the stress state:

$$\dot{\pi} = \frac{\partial \Phi^*(\sigma)}{\partial \sigma}. \quad (77)$$

Different types of dissipation potentials are herein considered, that can be found in the literature:

- the potential proposed by Perzyna [54]:

$$\Phi^*(\sigma) = \begin{cases} \frac{\tilde{\sigma}_y}{\mu} \left[\frac{1}{1+\epsilon} + \frac{\epsilon}{1+\epsilon} \Theta^{\frac{1+\epsilon}{\epsilon}} \right] & \text{if } f(\sigma) \geq 0 \\ 0 & \text{if } f(\sigma) < 0 \end{cases}, \quad (78)$$

$$\text{with } \Theta(\sigma) = q/\tilde{\sigma}_y - 1,$$

- the potential proposed by Perić [53]:

$$\Phi^*(\sigma) = \begin{cases} \frac{\tilde{\sigma}_y}{\mu} \left[\frac{1}{1+\epsilon} + \frac{\epsilon}{1+\epsilon} \Theta^{\frac{1+\epsilon}{\epsilon}} - \Theta \right] & \text{if } f(\sigma) \geq 0 \\ 0 & \text{if } f(\sigma) < 0 \end{cases}, \quad (79)$$

$$\text{with } \Theta(\sigma) = q/\tilde{\sigma}_y.$$

In equations (78) and (79), μ is a viscosity-related parameter, ϵ is the dimensionless rate sensitivity parameter, with $\epsilon \in (0, 1)$ and $\Theta(\sigma)$ a function that depends on the yield surface.

Differentiating the dissipation potential with respect to the stress state and taking into account for (32), one determines the evolution of the internal variables:

$$\dot{\pi} = \dot{\alpha} \mathbf{N}(\sigma), \quad (80)$$

where $\dot{\alpha}$ is defined:

- for the Perzyna model from equation (78):

$$\dot{\alpha} = \begin{cases} \frac{1}{\mu} \left[\left(\frac{q}{\tilde{\sigma}_y} - 1 \right)^{1/\epsilon} \right] & \text{if } f(\sigma) \geq 0 \\ 0 & \text{if } f(\sigma) < 0 \end{cases}, \quad (81)$$

- for the Perić model from equation (79):

$$\dot{\alpha} = \begin{cases} \frac{1}{\mu} \left[\left(\frac{q}{\sigma_y} \right)^{1/\epsilon} - 1 \right] & \text{if } f(\boldsymbol{\sigma}) \geq 0 \\ 0 & \text{if } f(\boldsymbol{\sigma}) < 0 \end{cases}, \quad (82)$$

It can be remarked that the classical Kuhn-Tucker loading-unloading conditions (60) do not govern the problem in case of rate dependent plasticity. In fact, when plasticity is reached, the updated stress state generally lies outside the yield surface, i.e. $f(\boldsymbol{\sigma}) > 0$. This is in contrast with the rate independent case, where the condition $f(\boldsymbol{\sigma}) = 0$ forces the updated stress state to lie on the yield surface when there is a plastic flow [63]. The crucial difference between the elasto-plastic and the elastic-viscoplastic model relies on the definition of the evolution of the internal variables. In fact, for elastic-viscoplastic materials, equation (32) is actually time-dependent, i.e. the time scale of the problem affects the evolution of $\boldsymbol{\pi}$. In addition, the hardening variable is not an independent variable of the problem, but it is an explicit function of the stress state.

3.3.2 Computational homogenization technique

The modified plastic multiplier is defined as in (63). The weak form of the modified plastic multiplier is introduced as:

$$\int_{\Omega} \delta\gamma \left(\dot{\gamma} - \frac{1}{2q} \dot{\alpha}(\boldsymbol{\sigma}) \right) d\Omega = 0, \quad (83)$$

where $\dot{\alpha}(\boldsymbol{\sigma})$ is defined according to the choice of Φ^* .

Then, the RVE is divided into n subsets Ω^j and on each of them an approximation for the stress and of the modified plastic multiplier is defined according to (34) and (36). A piecewise uniform distribution is considered for the modified plastic multiplier, i.e. $\rho = 1$ in all the subsets. In the typical j -th subset Ω^j , Eq. (83) takes the form:

$$\int_{\Omega^j} \delta\hat{\gamma}^j \left(\hat{\gamma}^j - \frac{1}{2q} \dot{\alpha}(\boldsymbol{\sigma}) \right) d\Omega = 0. \quad (84)$$

According to the dissipation potentials assumed in 3.3.1 it results:

$$\hat{\gamma}^j = \begin{cases} \frac{1}{\mu\Omega^j} \int_{\Omega^j} \frac{1}{2q^j} \left(\frac{q^j}{\bar{\sigma}_y} - 1 \right)^{1/\epsilon} d\Omega & \text{Perzyna} \\ \frac{1}{\mu\Omega^j} \int_{\Omega^j} \frac{1}{2q^j} \left[\left(\frac{q^j}{\bar{\sigma}_y} \right)^{1/\epsilon} - 1 \right] d\Omega & \text{Perić} \end{cases}, \quad (85)$$

Substituting Eqs. (85) into (83) written for the subset Ω^j , it results:

$$0 = \begin{cases} \hat{\gamma}^j - \frac{1}{\mu\Omega^j} \int_{\Omega^j} \frac{1}{2q^j} \left(\frac{q^j}{\bar{\sigma}_y} - 1 \right)^{1/\epsilon} d\Omega & \text{Perzyna} \\ \hat{\gamma}^j - \frac{1}{\mu\Omega^j} \int_{\Omega^j} \frac{1}{2q^j} \left[\left(\frac{q^j}{\bar{\sigma}_y} \right)^{1/\epsilon} - 1 \right] d\Omega & \text{Perić} \end{cases}. \quad (86)$$

3.3.3 Numerical procedure

The evolution problem is solved employing the backward Euler algorithm described in 3.1.1. The residual form of equation (86), integrated in the time step and its partial derivative with respect to the unknowns $\{\hat{\sigma}^j, \Delta\hat{\gamma}^j\}^T$ are rewritten as:

$$\mathbf{R}_\gamma^j = \begin{cases} \Delta\hat{\gamma}^j - \frac{\Delta t}{\mu\Omega^j} \int_{\Omega^j} \frac{1}{2q^j} \left[\left(\frac{q^j}{\bar{\sigma}_y} - 1 \right)^{\frac{1}{\epsilon}} \right] d\Omega & \text{Perzyna} \\ \Delta\hat{\gamma}^j - \frac{\Delta t}{\mu\Omega^j} \int_{\Omega^j} \frac{1}{2q^j} \left[\left(\frac{q^j}{\bar{\sigma}_y} \right)^{\frac{1}{\epsilon}} - 1 \right] d\Omega & \text{Perić} \end{cases} \quad (87)$$

$$\frac{\partial \mathbf{R}_\gamma^j}{\partial \hat{\sigma}^i} = \delta_{ij} \begin{cases} \frac{\Delta t}{2\mu\Omega^j} \int_{\Omega^j} \frac{1}{q^j} \left\{ \frac{1}{q^j} \Theta^{\frac{1}{\epsilon}} - \frac{1}{\epsilon \bar{\sigma}_y} \Theta^{\frac{1}{\epsilon}-1} \right\} \frac{\partial q^j}{\partial \hat{\sigma}^i} d\Omega & \text{Perzyna} \\ \frac{\Delta t}{2\mu\Omega^j} \int_{\Omega^j} \frac{1}{q^j} \left\{ \frac{1}{q^j} [\Theta^{\frac{1}{\epsilon}} - 1] - \frac{1}{\epsilon \bar{\sigma}_y} \Theta^{\frac{1}{\epsilon}-1} \right\} \frac{\partial q^j}{\partial \hat{\sigma}^i} d\Omega & \text{Perić} \end{cases} \quad (88)$$

$$\frac{\partial \mathbf{R}_\sigma^j}{\partial \Delta\hat{\gamma}^i} = \delta_{ij} \hat{\mathbf{P}}^j \hat{\sigma}^j - \mathbf{K}^{ij} \hat{\sigma}^i \quad (89)$$

$$\frac{\partial \mathbf{R}_\gamma^j}{\partial \Delta\hat{\gamma}^i} = \delta_{ij} . \quad (90)$$

where δ_{ij} and being δ_{ij} Kronecker's delta and $\frac{\partial q^j}{\partial \hat{\sigma}^i}$ is defined by Eq. (72).

3.3.4 Numerical results

In this section, the performance of the proposed technique in determining of the overall mechanical behavior of composites is assessed. In particular, composites characterized by a periodic microstructure are considered in the numerical applications, so that the UC subjected to periodic boundary conditions is studied.

The MxTFA code is implemented into a Fortran program and linear stress approximation is assumed for all the subsets. The stress approximation matrix \mathbf{P} and the evaluation of the localization operators and of the influence matrices, as well as the evaluation of the localization operators \mathbf{L}_ϵ^j and $\mathbf{L}_{\pi^i}^j$ employed in the MxTFA is carried out as described in 3.2.3. employing 2D four-node elements implemented in the code FEAP.

Two numerical applications are presented: the first is performed on a simple geometry in order to assess the capability of the viscoplastic

MXTFA procedure to capture the rate dependency of the problem by applying to the UC an average strain field at increasing strain rates. In order to show the applicability of the proposed technique to different viscoplastic models, both the viscoplastic models introduced by [54] and [53], described above, are adopted. In the second application, a more realistic geometry's considered and only the viscoplastic model introduced by Perzyna is used, performing analyses for different values the viscosity parameter ϵ at a given strain rate. The ability of the MXTFA technique to reproduce the response of the UC when subjected to loading/unloading strain histories is also investigated.

The results obtained with the proposed homogenization procedure are compared with nonlinear micromechanical analyses, carried out using 2D plane stress four-node quadrilateral finite elements, characterized by elastic and viscoplastic constitutive models. The same finite element meshes adopted for the pre-analyses are used for the nonlinear analyses.

3.3.4.1 Test 1 - UC with rectangular inclusion

A periodic heterogeneous material characterized by a viscoplastic matrix and elastic rectangular inclusions is considered. The geometric properties of the UC are the same of Test 1 in 3.2.3 (reported in Fig. 9a). The mechanical properties of the constituents are summarized in Table 8. Both the elastic pre-analyses and for the nonlinear micromechanical analysis were carried out using the finite element mesh of Fig. 9b. The homogenization analyses are performed considering the subset configurations shown in Figures 10a and 10b. In particular, only one subset is used for the elastic inclusion, while the matrix is subdivided into 3 and 5 subsets, resulting, respectively, in $3 \times 8 = 24$ and $5 \times 8 = 40$ history variables of the MXTFA procedure. In the micromechanical nonlinear analysis performed on the mesh shown in Fig. 9b it results $150 \times 4 \times 4 = 2400$.

Constituent	E [MPa]	n	σ_y [MPa]	H [GPa]	μ [s]	ϵ
Inclusion (elastic material)	25000	0.15	-	-	-	-
Matrix (viscoplastic material)	2500	0.15	3	0	500	$\frac{1}{0.1}$

Table 8: Test 1 - Material properties of the constituents.

The UC is subjected to uniaxial loading along x_1 -direction, with an increasing monotone average strain $\bar{\epsilon}_{11}$ that reaches the maximum value $\bar{\epsilon}_{11} = 0.005$, prescribing the symmetry boundary conditions (76). Several simulations are carried out at different strain rates, considering two different values of rate sensitivity coefficients.

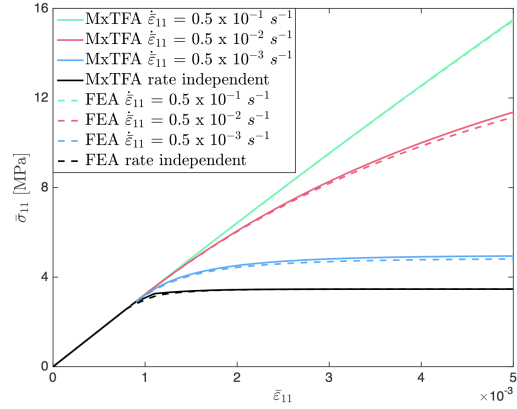
The mechanical response of the equivalent homogenized material in terms of average stress $\bar{\sigma}_{11}$ versus average strain $\bar{\epsilon}_{11}$ obtained with

the MxTFA compared with the FEA at different strain rates, $\dot{\bar{\epsilon}}_{11} = 0.05 \text{ s}^{-1}$, 0.005 s^{-1} , 0.0005 s^{-1} , is shown in Fig. 19 for the 4-subset configuration. The rate independent (i. e. elasto-plastic) curve is also reported as limit case for $\dot{\bar{\epsilon}}_{11} \rightarrow 0$. In particular, Fig. 19a shows the results for $\epsilon = 1$ using Perić model, while Fig. 19b and 19c for $\epsilon = 0.1$, adopting Perić and Perzyna models, respectively. Results for $\epsilon = 1$ are shown only for the Perić model, since for high value of rate sensitivity parameter the two models lead to similar results. On the contrary, for low values of the rate sensitivity parameter the two models lead to different results, and in particular, it can be seen that for $\epsilon \rightarrow 0$ the Perzyna results do not tend to the rate independent curve, but they tend to a curve whose maximum value of the stress is almost twice the one corresponding to the rate independent model. The effectiveness of the MxTFA is determined comparing the results with the FEA ones. In particular, in Table 9 the percentage errors of average stress $\bar{\sigma}_{11}$ at the end of the analyses (i.e. when the average deformation $\bar{\epsilon}_{11}$ reaches its final value) are collected. In the same table, the elasto-plastic results are also shown as the limit case for vanishing strain rate. As it can be noted, there is a very good agreement between the MxTFA predictions and the micromechanical reference solution. The results show that the major influence of the strain rate is observed for the high value of the rate sensitivity parameter ($\epsilon = 1$) reaching a maximum error equal to 2.77% for low value of the strain rate; while only a minor difference can be observed for the low value of the sensitivity parameter ($\epsilon = 0.1$) reaching a maximum error equal to 0.89% for high value of the strain rate. The effect of the strain rate on the response of the material can also be observed: for a given value of ϵ , higher stress values are obtained at high rates, and the rate independent (i.e. the elasto-plastic) solution is approached as the strain rate vanishes. Finally, it can also be remarked that only 4 subsets suffice to achieve very good accuracy in the evaluation of the average stress $\bar{\sigma}_{11}$ at the end of the analysis. The results obtained using the 6-subset partitioning do not provide a substantial improvement in the accuracy and for this reason they are not reported.

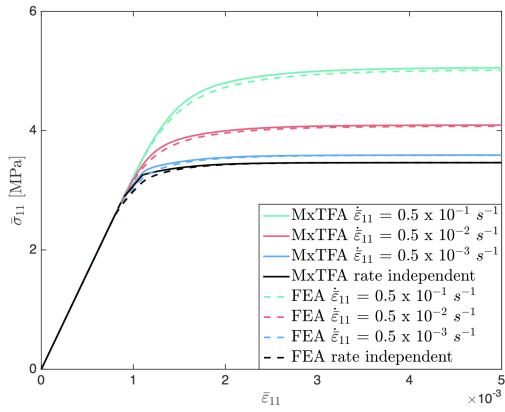
Numerical results show also that a linear viscoplastic flow rule ($\epsilon = 1$) could induce a complex inelastic strain distribution, more difficult to be approximated than the one obtained considering a nonlinear viscoplastic flow rule ($\epsilon = 0.1$). In other words, it is not ensured that the inelastic strain distribution coming from a simple (linear) evolution law can be more effectively approximated by the assumed inelastic strain than that coming from a more complex (nonlinear) evolution law.

Local strain

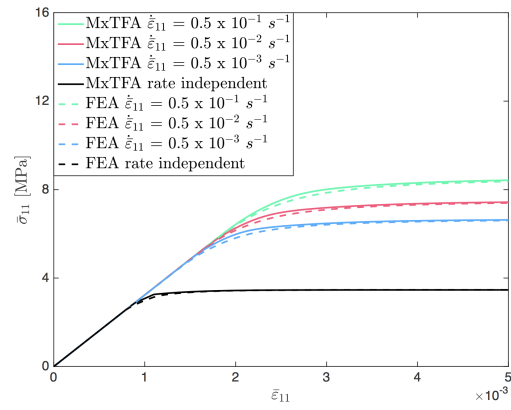
In addition to the previous results, it might be interesting to inspect the local distribution of the strain field. The total strain at the end of the loading history for the two subset configurations are shown in Fig. 20, considering the Perić model, $\epsilon = 0.1$ and strain rate $0.5 \cdot 10^{-2}$



(a)



(b)



(c)

Figure 19: Test 1 - Mechanical response of the UC subjected to uniaxial loading: (a) $\epsilon = 1$ Perić , (b) $\epsilon = 0.1$ Perić, (c) $\epsilon = 0.1$ Perzyna.

Strain rate [s^{-1}]	FEA	MxTFA	Error (%)
$0.5 \cdot 10^{-1}$	15.46	15.49	0.23
$0.5 \cdot 10^{-2}$	11.14	11.36	1.98
$0.5 \cdot 10^{-3}$	4.8	4.94	2.32
rate independent	3.46	3.47	0.02

(a)

Strain rate [s^{-1}]	FEA	MxTFA	Error (%)
$0.5 \cdot 10^{-1}$	5.02	5.05	0.78
$0.5 \cdot 10^{-2}$	4.07	4.09	0.47
$0.5 \cdot 10^{-3}$	3.58	3.59	0.04
rate independent	3.46	3.47	0.02

(b)

Strain rate [s^{-1}]	FEA	MxTFA	Error (%)
$0.5 \cdot 10^{-1}$	8.37	8.42	0.66
$0.5 \cdot 10^{-2}$	7.40	7.43	0.51
$0.5 \cdot 10^{-3}$	6.61	6.63	0.38
rate independent	3.46	3.47	0.02

(c)

Table 9: Test 1 - Final value of the average stress $\bar{\sigma}_{11}$ [MPa] for uniaxial loading condition; (a) $\epsilon = 1$ Perić model, (b) $\epsilon = 0.1$ Perić model, (c) $\epsilon = 0.1$ Perzyna model.

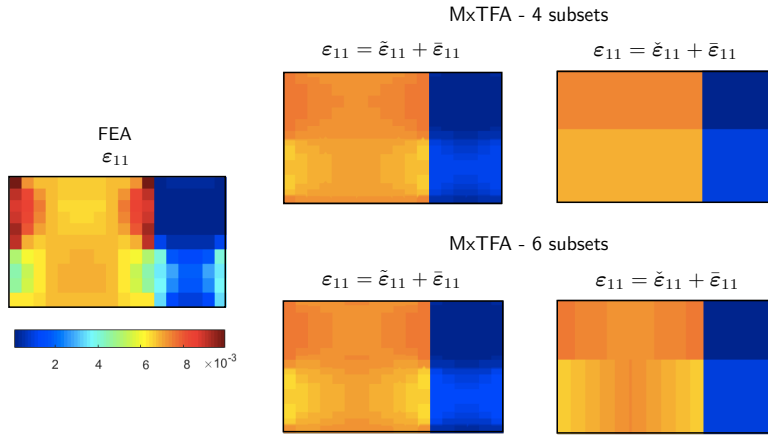


Figure 20: Test 1- Comparison between strain maps coming from FEA and MxTFA.

s^{-1} . The total strain ϵ is defined, according to (10), as the sum of two contributions, deriving from the prescribed average strain $\bar{\epsilon}$ and from the perturbation strain $\tilde{\epsilon}$. The latter is defined by Eq. (38) as function of the localization tensors $L_{\tilde{\epsilon}}^j$ and $L_{\pi_i}^j$, while its approximation $\check{\epsilon}$ is introduced by Eq. (39). In Fig. 20, two different strain distributions are considered: one coming from the perturbation strain $\tilde{\epsilon}$ and the other coming from its approximation $\check{\epsilon}$. As expected, $\check{\epsilon}$ determines a smoother distribution of the strain inside the domain with respect to $\tilde{\epsilon}$. Moreover, little differences in the local distribution can be observed passing from 4 to 6 subsets. For the same analysis, the average stress component $\bar{\sigma}_{11}$ is evaluated following three different approaches:

Average stress evaluation

- via stress parameters $\hat{\sigma}$ using Eq. (56) and denoted with $\hat{\sigma}$
- via constitutive law recovering the strain and inelastic strain fields using the full kinematic information provided by the localization tensors, denoted with π_{loc}
- via constitutive law recovering the strain and inelastic strain fields employing the strain approximation (39), denoted with $\pi_{\hat{\epsilon}}$

Fig. 21 shows that the evaluation of the average stress directly from the stress parameters determines a higher accuracy in the predictions.

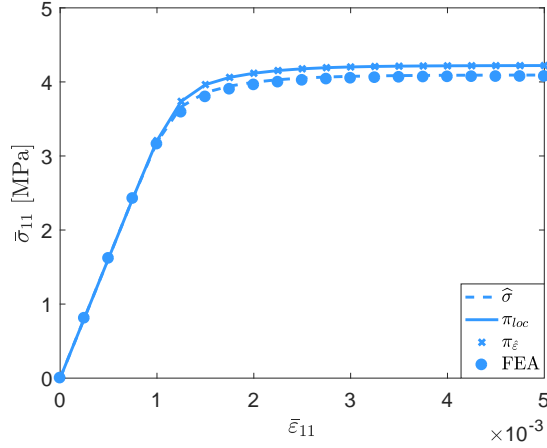


Figure 21: Test 1- Average stress evaluation using different approaches.

3.3.4.2 Test 2 - UC with a circular inclusion

The UC consists in a circular elastic inclusion embedded in a viscoplastic matrix with volume fraction equal to 25%, as shown in Fig. 22. Thanks to symmetry only one quarter of the UC is modeled applying symmetry boundary conditions defined by (76), with $a_1 = a_2 = a$. The following geometrical parameters are assumed: $a = 1$ mm and $r = 0.56$ mm. The material parameters are collected in Table 10. From the table it can be observed that the rate sensitivity parameter ϵ is set equal to 0.1, 0.2 or 1.

Fig. 23a shows that for the FEA model employed to perform the linear elastic pre-analyses and to compute the micromechanical reference solution, the quarter of UC has been discretized using 304 finite elements, 176 for the matrix and 128 for the inclusion. The history variables of the nonlinear micromechanical analysis are equal to $176 \times 4 \times 3 = 2112$. One of the main advantages of the MxTFA approach is that the subsets can have any shape (convex and no-convex shapes): this allows to model complex shapes using a small number of subsets. Anyway, the choice of the subsets is important to reach accurate results, as their shapes can influence the solution. As in finite elements, a suitable choice is to discretize the domain with regular subsets. For this reason, an almost regular discretization in subdomains is performed. In fact, the MxTFA homogenization analyses are performed discretizing the UC with 7 subsets (6 subsets for the matrix and 1 subset for the inclusion), as shown Fig. 23b, resulting in $6 \times 7 = 42$ history variables, significantly lower than the ones of the FEA.

UNIAXIAL LOADING ALONG x_2 -AXIS The UC is subjected to uniaxial loading along the x_2 -axis at the constant strain rate $\dot{\bar{\epsilon}}_{22} = 0.1s^{-1}$, with the average strain $\bar{\epsilon}_{22}$ monotonically increased until the final

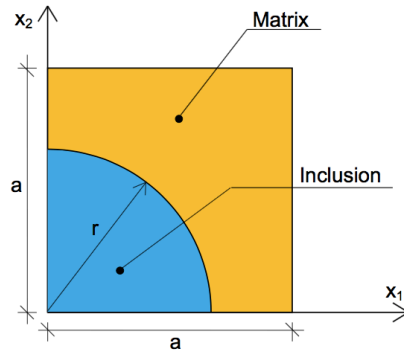


Figure 22: Test 2 - Problem geometry.

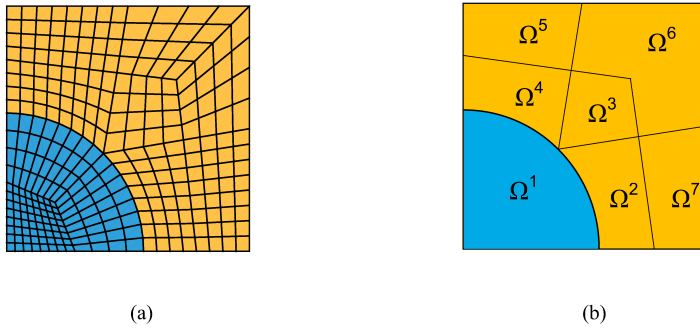


Figure 23: Test 2 - (a) Finite element mesh for reference solution and pre-analyses, (b) Subset discretization.

Constituent	E [GPa]	n	σ_y [MPa]	μ [s]	ϵ
Inclusion (elastic material)	400	0.20	-	-	-
Matrix (viscoplastic material)	70	0.30	480	500	0.2
					0.1

Table 10: Test 2 - Material properties for the constituents.

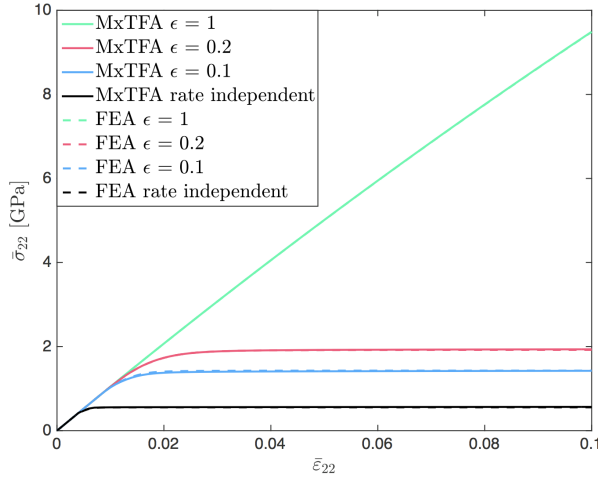


Figure 24: Test 2 - Mechanical response of the UC subjected to uniaxial loading.

ϵ	FEA	MxTFA	Error (%)
1	9.48	9.49	0.06
0.2	1.92	1.94	0.78
0.1	1.43	1.42	0.35
rate independent	0.56	0.57	2.01

Table 11: Test 2 - Final value of the average stress $\bar{\sigma}_{22}$ [GPa] for uniaxial loading condition.

value $\bar{\epsilon}_{22} = 0.1$. Fig. 24 shows the constitutive response of the equivalent homogenized material in terms of $\bar{\sigma}_{22}$ versus $\bar{\epsilon}_{22}$ for all the rate sensitivity exponents together with the corresponding FEA reference solution. The rate independent (elasto-plastic) solution is also reported, as limit case for $\epsilon \rightarrow 0$. The final value of the average stress $\bar{\sigma}_{22}$ obtained with the MxTFA is compared with the reference one deriving from the FEA in Table 11. As expected, different behaviors are observed for different values of ϵ , with higher stress values for higher values of the rate sensitivity parameter. These results highlight that the MxTFA is able to accurately reproduce the overall behavior of the UC also in this case, with the largest error equal to 2.01% for the rate independent case. Moreover, Fig. 25 shows the constitutive behavior of the UC, as well as the behavior of the sole matrix and inclusion, for $\epsilon = 0.2$. In particular, for the UC and each phase the respective average stress versus the respective average strain are reported. Also in this case the very good performance of the MxTFA can be observed.

For the same loading history, the stress and inelastic strain maps for the intermediate rate sensitivity parameter ($\epsilon = 0.2$) at the end of the analysis for the MxTFA and the FEA reference solution are reported in Figs. 26 and 27 respectively, in order to have a better insight of the

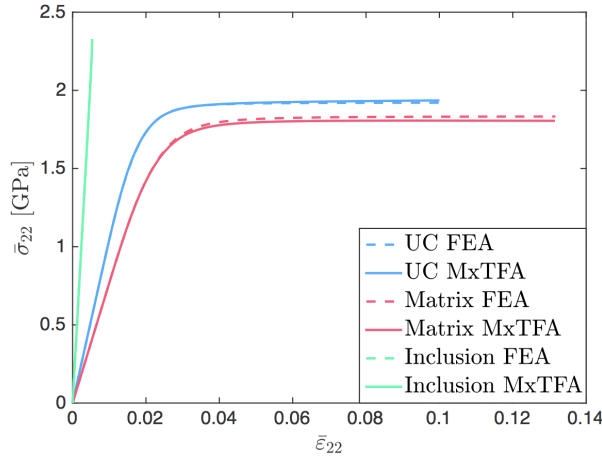


Figure 25: Test 2 - Mechanical response of the UC and the two phases subjected to uniaxial loading ($\epsilon = 0.2$).

local distribution of these quantities. A good agreement between the two solutions is observed.

The local error evaluated as the absolute value of the difference between the FEA reference solution and the MxTFA solution is shown in Fig. 28.

For this load case the local distribution at the end of the analysis is shown in Fig. 29, where the strain evaluated via FEA is compared with the one evaluated via MxTFA employing the full kinematic information provided by the localization operators (38) and the strain projection onto the reduced basis (39). As expected, a smoother distribution is obtained moving from (38) to (39).

Local strain

LOADING/UNLOADING HISTORIES The UC is considered subjected to the uniaxial loading/unloading history along x_1 -axis at a constant strain rate equal to $|\dot{\epsilon}_{11}| = 0.1 \text{ s}^{-1}$, collected in Table 12. The overall response of the UC is reported in Fig. 30 comparing the MxTFA and FEA results for the rate sensitivity parameter equal to $\epsilon = 0.1$ and $\epsilon = 0.2$; also the case of the rate independent elasto-plastic solution is reported.

Furthermore, the bi-axial loading/unloading history, shown in Table 13, is considered. In Fig. 31a the average stress $\bar{\sigma}_{11}$ is plotted versus the average strain $\bar{\epsilon}_{11}$ and in Fig. 31b $\bar{\sigma}_{22}$ is plotted versus $\bar{\epsilon}_{22}$ for MxTFA and FEA considering $\epsilon = 0.1$, $\epsilon = 0.2$ and the rate independent case.

The MxTFA results, obtained for both the uniaxial and bi-axial loading/unloading histories, appear in a very satisfactory agreement with the FEA responses, denoting also in this case the effectiveness of the proposed homogenization procedure.

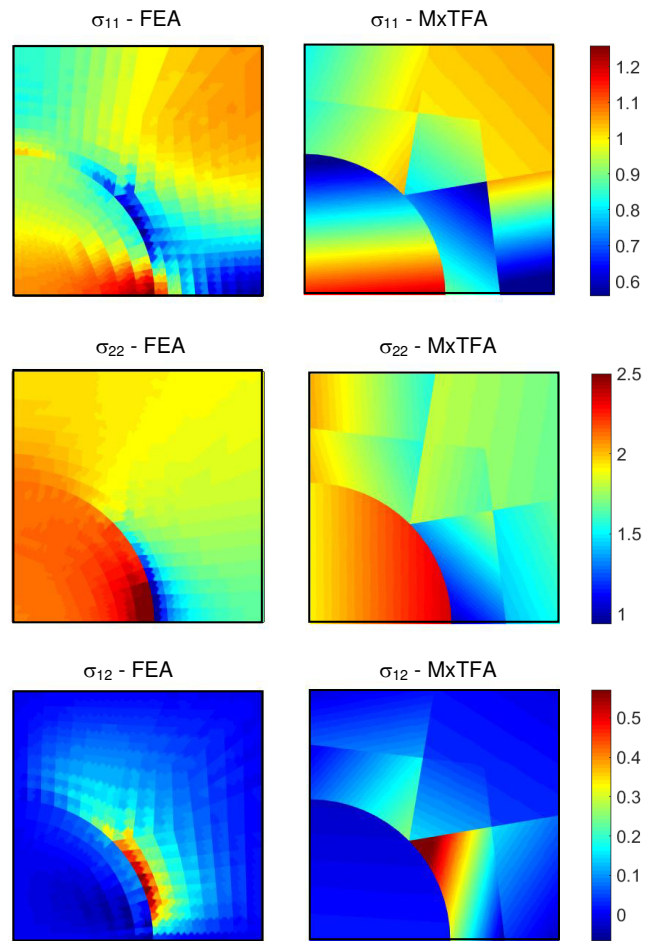


Figure 26: Test 2 - Contour maps of stress [GPa] for $\epsilon = 0.2$.

Table 12: Test 2 - Loading history along x_1 - axis.

Time [s]	$\bar{\epsilon}_{11}$	$\bar{\epsilon}_{22}$	$\bar{\epsilon}_{12}$
0	0	0	0
1	0.1	0	0
2	0	0	0
3	-0.1	0	0
4	0	0	0

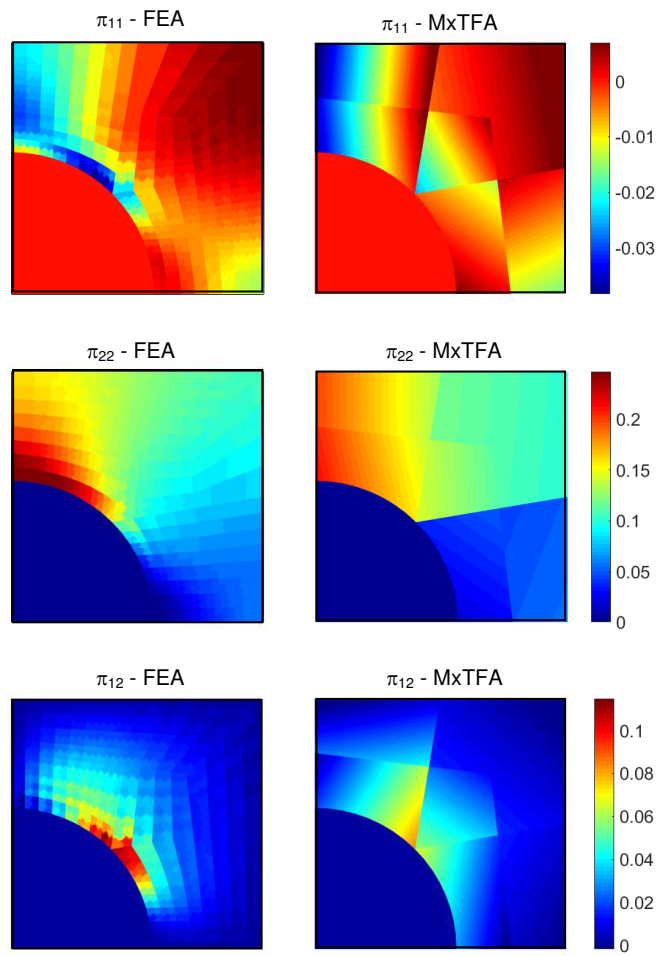


Figure 27: Test 2 - Contour maps of inelastic strain for $\epsilon = 0.2$.

Table 13: Test 2 - Biaxial loading history.

Time [s]	$\bar{\epsilon}_{11}$	$\bar{\epsilon}_{22}$	$\bar{\epsilon}_{12}$
0	0	0	0
1	0.1	0	0
2	0.1	0.1	0
3	0	0.1	0
4	0	0	0

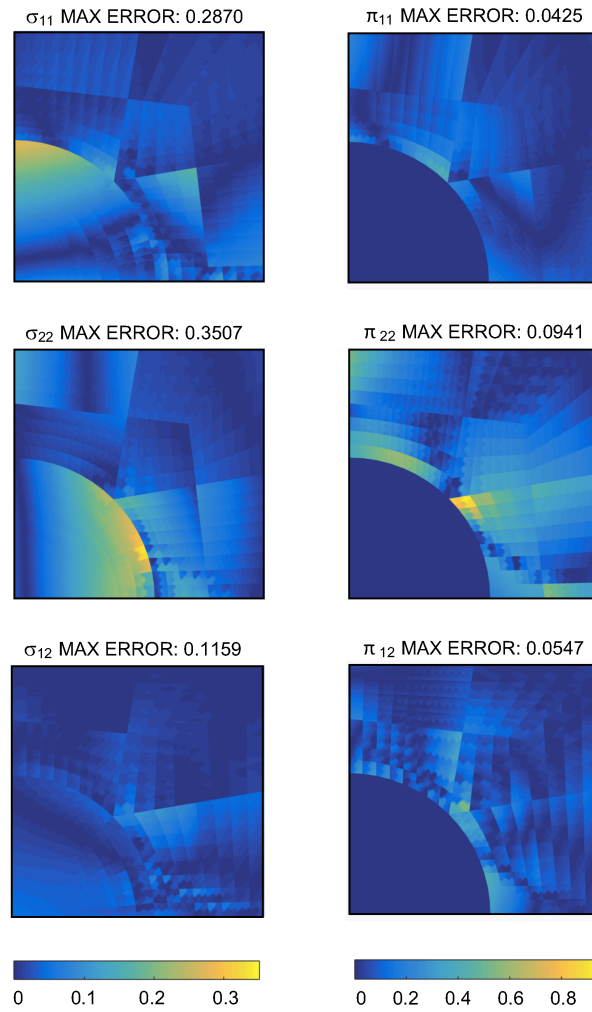


Figure 28: Test 2 - Local error maps of the stress [GPa] and inelastic strain, $\epsilon = 0.2$.

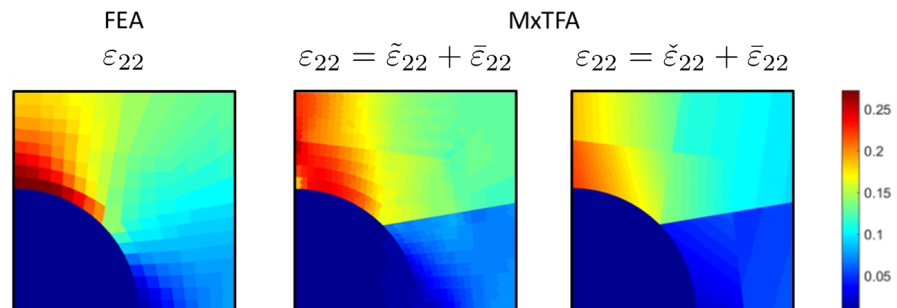


Figure 29: Test 2 - Strain distribution.

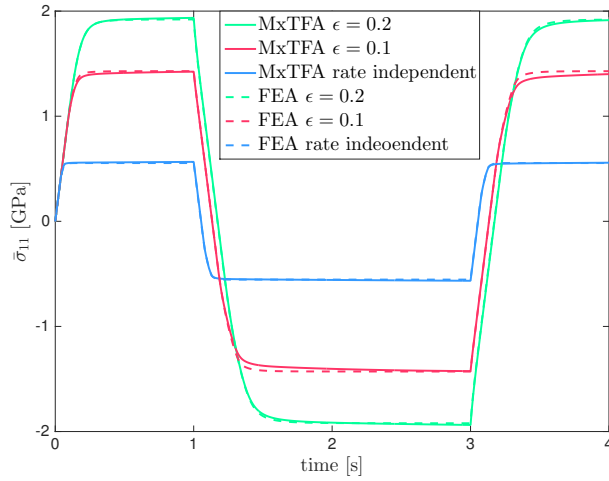
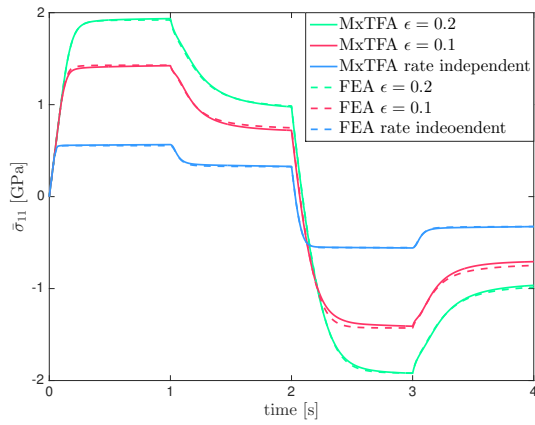
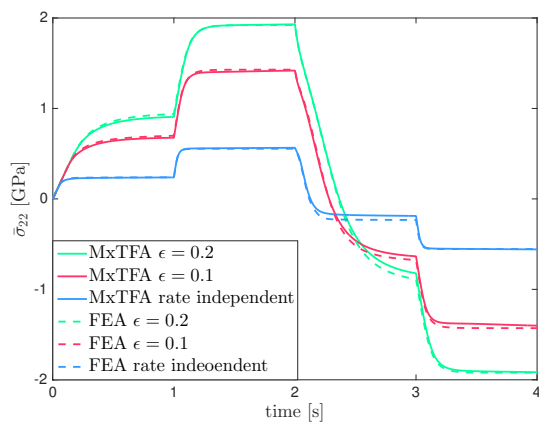


Figure 30: Test 2 - Mechanical response of the UC subjected to a uniaxial loading history.



(a)



(b)

Figure 31: Test 2 - Mechanical response of the UC subjected to a bi-axial loading history: (a) mechanical response in x_1 -direction; (b) mechanical response in x_2 -direction.

COMPARISON BETWEEN NTFA-BASED MODEL ORDER REDUCTION TECHNIQUES

The ideas first presented in the scope of the NTFA remain appealing even today and they have been the starting point for several Reduced Order Models (ROMs) rather recently. In this Chapter three of these ROMs stemming from the TFA and NTFA concepts are compared: the potential Reduced Basis Model Order Reduction (pRB MOR) of Fritzen and Leuschner [28, 29], the New Nonuniform TFA (NUTFA) by [61] and the recent MxTFA of [12] [also 13].

4.1 COMPARISON CRITERIA

The comparison between the three ROMs is carried out on the basis of four criteria that are outlined in the following. In particular, differences and similarities are investigated in terms of:

- **Mode selection**

Intuitively the proper choice of the modes has a major impact on the accuracy and efficiency of the approach. Two main directions followed in the literature are: (i) the direct construction via analytical shape functions and (ii) a snapshot proper orthogonal decomposition (snapshot POD) of plastic strain fields found during nonlinear pre-analyses (first done by [59] in the NTFA context).

- **Pre-analyses**

All techniques require pre-analyses in order to determine the operators necessary to perform the nonlinear homogenization analysis. In particular, linear elastic pre-analyses are required for NUTFA and MxTFA, while nonlinear pre-analyses are needed for the pRB MOR.

- **Evolution of the reduced degrees of freedom**

although all three investigated homogenization strategies might have large parts in common (for instance the self-equilibrated stress fields inspired by the TFA/NTFA), the biggest difference is found in terms of the evolution of the reduced degrees of freedom.

- **Effective stress computation**

The effective stress describes the macroscopic material response, and it can be computed only once the evolution problem is

solved in terms of internal variables at the microscopic scale. As stated in the following sections, the reduced internal variables of the problem are different among the techniques: for the NUTFA they are the inelastic strain coefficients, for the pRB MOR they are the inelastic strain and hardening coefficients and for the MxTFA the stress and plastic multiplier parameters. For this reason, the effective stress is computed differently in the three techniques.

4.2 THE PRBMOR

4.2.1 Mode selection

The pRB MOR [28, 29] relies on numerical pre-analyses for the identification of appropriate basis functions as follows: first, a set of loading paths is decided. Then (nonlinear) FE simulations are conducted in order to gather reference solutions for π and α for each recorded time step for each loading. A Proper Orthogonal Decomposition (POD) is used to compress this data in terms of spatially heterogeneous plastic modes $\mu^{(k)}(\mathbf{x})$ ($k = 1, \dots, N_\mu$) and hardening modes $\alpha^{(l)}(\mathbf{x})$ ($l = 1, \dots, N_\alpha$). The number of modes can either be prescribed or a POD threshold can be defined which determines N_μ and N_α implicitly. The reduced approximations of the internal state variables are:

$$\pi(\mathbf{x}, t) = \widehat{\mathbf{P}}(\mathbf{x})\xi(t), \quad (91)$$

$$\alpha(\mathbf{x}, t) = \widehat{\mathbf{Q}}(\mathbf{x})\alpha(t), \quad (92)$$

with $\xi \in \mathbb{R}^{N_\mu}$ and $\alpha \in \mathbb{R}^{N_\alpha}$ being the reduced unknowns, $\widehat{\mathbf{P}}(\mathbf{x})$ is a matrix collecting the N_μ inelastic modes as columns and $\widehat{\mathbf{Q}}(\mathbf{x})$ is a matrix whose columns collect the N_α hardening modes. Typically, N_μ is on the order of 32 to 64 and N_α ranges from 12 to 32 in most applications.

The relation between ξ and $\bar{\varepsilon}$ and the local stress and strain field is found through self-equilibrated fields $\sigma_*^{(k)}(\mathbf{x})$ and $\varepsilon_*^{(k)}(\mathbf{x})$ and via the elastic strain localization operator $\mathbf{L}_{\bar{\varepsilon}}(\mathbf{x})$ defined via the linear elastic problems:

$$\mathbf{D}^\top \sigma_e = \mathbf{0}, \quad \sigma_e = \mathbf{C} \mathbf{L}_{\bar{\varepsilon}} \bar{\varepsilon}, \quad \langle \mathbf{L}_{\bar{\varepsilon}} \rangle = \mathbf{I}, \quad (93)$$

$$\mathbf{D}^\top \sigma_*^{(k)} = \mathbf{0}, \quad \sigma_*^{(k)} = \mathbf{C}(\varepsilon_*^{(k)} - \mu^{(k)}), \quad \langle \varepsilon_*^{(k)} \rangle = \mathbf{0}, \quad (94)$$

where the vectors σ_* are then collected into the stress localization operator $\widehat{\mathbf{S}}_\pi(\mathbf{x}) = \mathbf{C}(\mathbf{x}) \mathbf{L}_\pi(\mathbf{x})$. A plastic strain mode and the components $\bar{\sigma}_{22}$ and $\bar{\sigma}_{33}$ of the related self-equilibrated stress field are shown in Figure 4.6. The procedure is similar to the TFA of Dvorak [17] and the self-equilibrated fields are identical to the NTFA of Michel and Suquet [48]; a FE implementation is described in [26]. The self-equilibrated

fields defined via (93), (94) imply that balance of linear momentum is always exactly satisfied. The only effective reduction is, hence, found in the inelastic variables: a constitutive approach to model reduction is pursued. Note also that the NUTFA follows a similar procedure, but (usually) requires more self-equilibrated fields as more independent plastic strain modes are used.

4.2.2 Pre-analyses

The pRB MOR requires two sets of pre-analyses: in the first set, several inelastic computations of the RVE along different loading paths are performed in order to collect the snapshot information (see Section 4.2.1). This part of the offline phase differs significantly from both the NUTFA and MxTFA which do not require nonlinear pre-analyses.

In addition to the collection of the snapshot data, the $(6 + N_\mu)$ linear problems for the self-equilibrated stress and strain fields (see Eqs. (93) and (94)) must also be solved once during the offline phase. They are basically identical to the linear computations of the NUTFA and MxTFA.

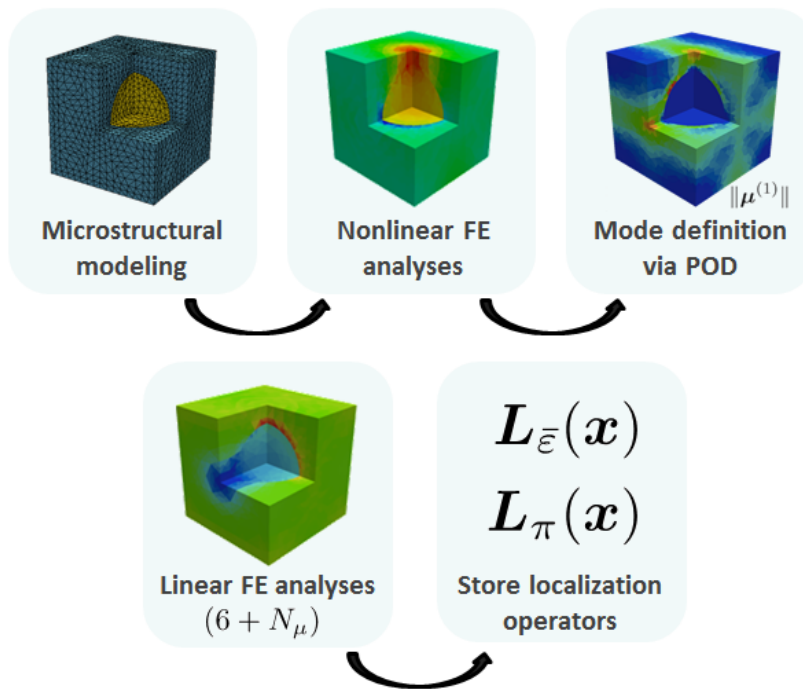


Figure 32: pRB MOR- Pre analyses.

4.2.3 Evolution of reduced degrees of freedom

The evolution of the reduced vectors ξ, λ of the pRB MOR is motivated from a mixed variational formulation that leads to a saddle-point

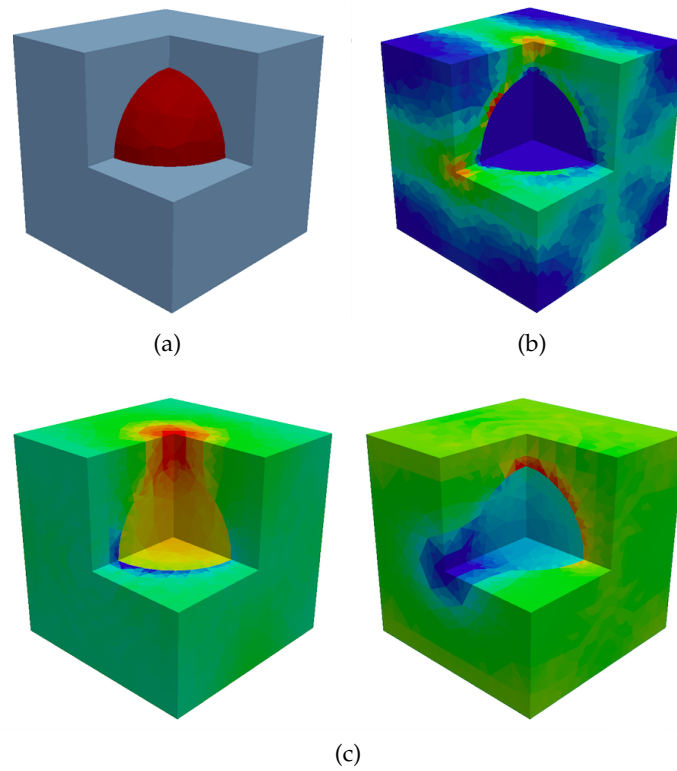


Figure 33: Inclusion matrix material - (a) RVE, (b) norm of the first plastic strain mode (c) stress components 22 and 33 of the induced self-equilibrated stress field for the example of Section 4.6.

problem (see [28, 31] for details) including the Helmholtz free energy ψ of the material:

$$\frac{1}{\Delta t} \begin{Bmatrix} \Delta \xi \\ \Delta \lambda \end{Bmatrix} = \arg \min_{\Delta \xi, \Delta \lambda} \arg \max_{\boldsymbol{\tau}, \mathbf{R}} \langle \Delta \psi \rangle + \begin{Bmatrix} \Delta \xi \\ \Delta \lambda \end{Bmatrix} \cdot \begin{Bmatrix} \boldsymbol{\tau} \\ \mathbf{R} \end{Bmatrix} - \Delta t \langle \Phi^*(\boldsymbol{\sigma}, r') \rangle, \quad (95)$$

with $r' = -\tilde{\sigma}_y$ for formal reasons. Here $\boldsymbol{\tau}$ and \mathbf{R} are the conjugate driving forces related to the inelastic strain modes and hardening modes, respectively:

$$\boldsymbol{\tau} = -\frac{\partial \langle \psi \rangle}{\partial \xi} = \langle \hat{\mathbf{P}}^T \boldsymbol{\sigma} \rangle, \quad \mathbf{R} = -\frac{\partial \langle \psi \rangle}{\partial \lambda} = -\langle \hat{\mathbf{Q}}^T \tilde{\sigma}_y \rangle. \quad (96)$$

After some intermediate steps the following time discrete evolution equations are obtained cf. [31] through projection of the local rate of the internal variables:

$$\frac{\Delta \xi}{\Delta t} = \hat{\mathbf{D}}^{-1} \langle \tilde{\mathbf{S}}_\pi \frac{\partial \Phi^*}{\partial \boldsymbol{\sigma}} \rangle = \hat{\mathbf{D}}^{-1} \langle \tilde{\mathbf{S}}_\pi \dot{\boldsymbol{\pi}} \rangle = \mathcal{P}^\xi [\dot{\boldsymbol{\pi}}], \quad (97)$$

$$\frac{\Delta \lambda_l}{\Delta t} = \hat{\mathbf{H}}^{-1} \langle \hat{\mathbf{Q}}^T \frac{\partial \tilde{\sigma}_y}{\partial \alpha} \frac{\partial r}{\partial \alpha} \frac{\partial \Phi^*}{\partial r} \rangle = \hat{\mathbf{H}}^{-1} \langle \hat{\mathbf{Q}}^T \frac{\partial \tilde{\sigma}_y}{\partial \alpha} \frac{\partial r}{\partial \alpha} \dot{\alpha} \rangle = \mathcal{P}^\lambda [\dot{\alpha}]. \quad (98)$$

The operators \mathcal{P}^ξ , \mathcal{P}^λ can be interpreted as projection operators. The symmetric matrices $\hat{\mathbf{D}}$ and $\hat{\mathbf{H}}$ are defined through:

$$\hat{\mathbf{D}} = -\langle \hat{\mathbf{S}}_\pi^T \mathbf{C}^{-1} \hat{\mathbf{S}}_\pi \rangle, \quad \hat{\mathbf{H}} = -\langle \hat{\mathbf{Q}}^T \frac{\partial \tilde{\sigma}_y}{\partial \alpha} \hat{\mathbf{Q}} \rangle. \quad (99)$$

It must be noted that $\hat{\mathbf{H}}$ depends on the reduced hardening state α . Hence, the projection operator in (98) is not constant which was also stated in [31].

4.2.4 Effective stress computation

The pRB MOR computes the effective stress based on the super-position of the weighted average of the self-equilibrated fields via

$$\bar{\boldsymbol{\sigma}} = \langle \mathbf{C} \rangle \bar{\boldsymbol{\varepsilon}} + \langle \hat{\mathbf{S}}_\pi \rangle \boldsymbol{\xi}. \quad (100)$$

4.3 THE NUTFA

4.3.1 Mode selection

The NUTFA assumes that the RVE is subdivided into n non-overlapping subsets Ω^j ($j = 1, \dots, n$) and relies on a direct construction of the modes via analytical shape functions. The partitioning is performed considering the microstructural geometry of the material. For instance, partitions should account for the position, shape and symmetry of inclusions. The subsets can have arbitrary even non-convex shape, and

this allows, in principle, to partition any microstructure without restraints. The domain partitioning is done only once during the offline (or pre-processing).

The inelastic modes in the NUTFA [61] are scalar, depending on the spatial variable and relying on a priori constructed shape functions on individual subsets. The NUTFA defines analytical modes which are scalar functions on each subset Ω^j . The modes do not have to satisfy any a-priori requirement, they only need to be regular enough and capable to represent a basis for the inelastic strain field. As a result, the reduced variables of the problem are vectors:

$$\boldsymbol{\pi}^j(\boldsymbol{x}, t) = \sum_{i=1}^{N_{\pi}^j} \mu^i(\boldsymbol{x}) \tilde{\boldsymbol{\pi}}^{j,i}(t). \quad (101)$$

where $\mu^i(\boldsymbol{x})$ are scalar inelastic modes represented by N_{π}^j pre-selected functions of the spatial variable and $\tilde{\boldsymbol{\pi}}^{j,i}(t)$ are tensors able to describe the time evolution of the plastic strain and they represent the internal variables of the evolution problem. Note that different number of modes N_{π}^j can be used to represent the inelastic strain in each subset.

4.3.2 Pre-analyses

As for the NUTFA, the pre-analyses are linear elastic computations employed on a full discretization of the microscopic domain in order to compute the localization tensors $\mathbf{L}_{\bar{\boldsymbol{\varepsilon}}}^g(\boldsymbol{x})$ and $\mathbf{L}_{\tilde{\boldsymbol{\pi}}^{j,i}}^g(\boldsymbol{x})$ able to recover the total strain in the typical point of the subset Ω^g by the relationship:

$$\boldsymbol{\varepsilon}^g = \mathbf{L}_{\bar{\boldsymbol{\varepsilon}}}^g \bar{\boldsymbol{\varepsilon}} + \sum_{j=1}^n \sum_{i=1}^{N_{\pi}^j} \mathbf{L}_{\tilde{\boldsymbol{\pi}}^{j,i}}^g \tilde{\boldsymbol{\pi}}^{j,i}, \quad (102)$$

where the localization operators for the subset Ω^j are evaluated as detailed in 3.1.

4.3.3 Evolution of reduced degrees of freedom

The NUTFA solves the evolution problem at each integration point of the domain, using the approximation of the local strain as driving parameter, i.e. the procedure is strain-driven. In particular, a backward Euler time integration scheme is adopted to evaluate the inelastic strain increment for every point of the domain by means of standard constitutive models. Then, the unknowns of the problem, i.e. the tensorial internal variables, are obtained by minimizing an error function in every subset, in order to derive the best approximation of the inelastic strain field with respect to the desired representation (i.e. the chosen analytical modes). In fact, once the updated value of the inelastic strain $\boldsymbol{\pi} = \boldsymbol{\pi}_n + \Delta\boldsymbol{\pi}$ has been determined in all the selected

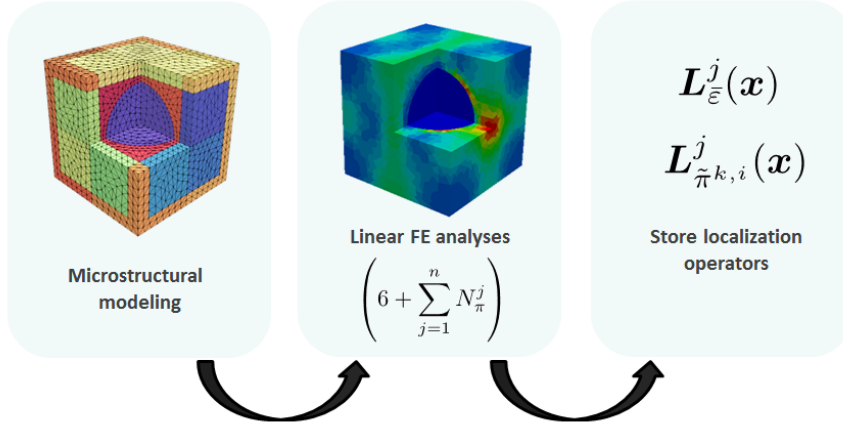


Figure 34: NUTFA- Pre analyses.

point of the subset Ω^j , the distribution of the inelastic strain is approximated adopting the representation proposed by equation (101). In particular, the error function is introduced as:

$$\Gamma_\pi = \sqrt{\int_{\Omega^j} \left(\boldsymbol{\pi}(\mathbf{x}) - \sum_{i=1}^{N_\pi^j} \mu^i(\mathbf{x}) \tilde{\boldsymbol{\pi}}^{j,i} \right)^\top \left(\boldsymbol{\pi}(\mathbf{x}) - \sum_{i=1}^{N_\pi^j} \mu^i(\mathbf{x}) \tilde{\boldsymbol{\pi}}^{j,i} \right) d\Omega} \quad (103)$$

and the minimum problem

$$\min \{ \Gamma_\pi \mid \tilde{\boldsymbol{\pi}}^{j,i} \ (i = 1, \dots, N_\pi^j) \} \quad (104)$$

is solved with respect to the N_π^j inelastic contributions $\tilde{\boldsymbol{\pi}}^{j,i}$. The described procedure is performed for all the subsets introduced in Ω .

4.3.4 Effective stress computation

Also in the NUTFA the effective stress is obtained via constitutive law. The effective stress in the subset Ω^g is given as:

$$\bar{\boldsymbol{\sigma}}^g = \langle \mathbf{C}^g \mathbf{L}_\varepsilon^g \rangle \bar{\boldsymbol{\varepsilon}} + \left\langle \sum_{j=1}^n \sum_{i=1}^{N_\pi^j} \mathbf{C}^g (\mathbf{L}_{\tilde{\boldsymbol{\pi}}^{j,i}}^g - \delta_{gj} \mu^i) \tilde{\boldsymbol{\pi}}^{j,i} \right\rangle, \quad (105)$$

with $\delta_{gj} = 1$ if $g = j$ and $\delta_{gj} = 0$ otherwise. As a result, the effective stress in the RVE is:

$$\bar{\boldsymbol{\sigma}} = \frac{1}{\Omega} \sum_{g=1}^n \Omega^g \bar{\boldsymbol{\sigma}}^g. \quad (106)$$

4.4 THE MXTFA

4.4.1 Mode selection

The MxTFA, based on a mixed variational framework of elasto-plasticity, defines an approximation of the stress and plastic multiplier over each subset Ω^j . As for the NUTFA, the subsets can have arbitrary shape and the partitioning is performed during the offline phase. The inelastic strain approximation is then derived from the stress and plastic multiplier approximations through the flow rule: differently from the NUTFA and pRBMOR, the inelastic modes are not directly defined for the inelastic strain, but they depend on the assumed approximation for the stress and plastic multiplier. In addition, over each subset Ω^j , the stress approximation is described by N_p^j self-equilibrated modes, that need to satisfy the requirement of zero divergence over the subset Ω^j .

The modified plastic multiplier (related to the hardening variable) is approximated in each subset Ω^j independently from the representation of the stress field as: where $\rho^j(\mathbf{x})$ is a set of N_p^j modes chosen to approximate the modified plastic multiplier $\dot{\gamma}$ in Ω^j and $\hat{\gamma}^j$ is the vector containing the corresponding coefficients. In principle, different number of modes N_p^j can be used to represent the inelastic multiplier in each subset, but a simple and common choice is to consider a piecewise uniform distribution for $\dot{\gamma}^j$, i.e. it is set $\rho^j = 1$ in all subsets.

The internal variables, i.e. the unknown of the problem, are the reduced stresses $\hat{\sigma}^j$ and the reduced plastic multipliers $\hat{\gamma}^j$.

4.4.1.1 Pre-analyses

In the MxTFA, the pre-analyses are the same linear elastic computations described in Section 3.1 of Chapter 3, aimed to compute the localization matrices L_ε^j and $L_{\pi^i}^j$. In addition, in order to ensure consistency between the representations of stress, total and inelastic strain, an approximation of the perturbation strain is introduced as shown in (39), and the corresponding coefficients determined from the projection of the perturbation strain onto the basis defined by Π . This implies that only the coefficients of the approximation of the perturbation strain $\hat{\varepsilon}$ need to be stored for every subset in order to solve the nonlinear homogenization analysis, and therefore there is no need to store the localization tensors for every integration point of the domain: in particular, for every subset, matrices of size $(N_l^j \times 6)$ and $(n \times N_l^j \times N_p^i)$ are stored, where N_l^j is the number of strain modes for Ω^j (see Eq. 39).

4.4.1.2 Evolution of reduced degree of freedom

Differently from the NUTFA, the evolution problem is not solved in any point of the domain. In fact, the independent variables of the problem (i.e. the stress and plastic multiplier parameters $\hat{\sigma}$ and $\Delta\gamma$ respectively) are obtained by enforcing the weak fulfillment of the compatibility equation and of the evolution of the plastic multiplier for every subset. The evolution of the reduced variables is solved employing a backward Euler time integration scheme with a return mapping technique. For each subset Ω^j , an elastic trial state is predicted, then the admissibility of the trial states is checked for the subset: if the trial state is admissible for all the subsets then the step is elastic, otherwise a nonlinear system deriving from the weak forms of the governing equations has to be solved for all the subsets simultaneously. At the time step Δt the nonlinear system to be solved for each subset Ω^j takes the following form: The inelastic strain field is then recovered from Eq.(45).

4.4.2 Effective stress computation

Since based on a mixed variational framework, the MxTFA computes the effective stress directly from the stress parameters that are recovered from the solution of the evolution problem in a more straightforward way, according to Eq. (56).

4.5 COMPARISON: INELASTIC MODES OF PRBMOR, NUTFA AND MXTFA

Some key differences can be highlighted regarding the definition of the inelastic modes for the three investigated techniques:

- **Partitioning of the RVE**
Both the NUTFA and the MxTFA make use of piecewise defined modes on the subsets Ω^j while the pRBMOR does not assume any partitioning.
- **Origin of the inelastic strain modes**
The NUTFA and the MxTFA are based on analytically defined mode sets. Thereby a general function space similar to the one of classical FE shape functions is spanned. In contrast to classical FE functions the domains are however arbitrarily shaped. Additionally, the inelastic strain fields are not assumed to be continuous between adjacent subsets. A priori, no accuracy prediction can be made for the NUTFA and the MxTFA.

In the pRBMOR the modes are linear combinations of actual solutions of the nonlinear problem. Hence, the modes share the same smoothness properties, i.e. the inelastic strain modes are

rather smooth functions over the full RVE and they are periodic with respect to the RVE. For sufficiently high number of modes (or sufficiently low POD threshold, respectively) the modes can accurately reproduce the training data from the pre-analyses. Thereby, some idea of the accuracy of the method is available without further investigations.

- **Computational effort**

The analytically defined shape functions of the NUTFA and MxTFA have the appealing feature of not being associated with any computations. Contrary to that, the pRB MOR requires the solution of a set of nonlinear pre-analyses. This can be a time consuming undertaking, especially for complex three-dimensional problems with fine discretization. However, the low number of linear pre-analyses of the pRB MOR in comparison to the NUTFA and MxTFA compensates (in parts) for the computational cost of the nonlinear computations.

- **Number of shape functions/number of reduced DOF!**

In the pRB MOR, the number of shape functions (and hence of history variables) depends on the total number of modes:

$$\bar{N}_{\text{pRB MOR}} = N_{\mu} + N_{\alpha}.$$

Usually $N_{\mu} > N_{\alpha}$ holds which is easily justified as π is a tensor field and α is a scalar in the considered setting: the tensor field lives on a higher-dimensional manifold and, hence, a higher dimensional reduced basis is straight-forward. Based on previous experience for a variety of different microstructures $\bar{N} \lesssim 60 \dots 160$. In both, the MxTFA and the NUTFA the total number of reduced DOF!s depends on the number of subsets and on the number of shape functions adopted. On one side in the NUTFA, since the inelastic modes are scalar, it results that: $\bar{N}_{\text{NUTFA}} = \sum_{i=1}^n (N_{\pi}^i \times 6) + N_h$, where N_h is the total number of hardening variables summed over all integration points of the RVE. On the other side in the MxTFA, being N_p^j the number of self-equilibrated stress modes and N_{ρ}^j the number of modes for the plastic multiplier for the subset Ω^j , then: $\bar{N}_{\text{MxTFA}} = \sum_{i=1}^n (N_p^i + N_{\rho}^i)$, with $N_p^i > N_{\rho}^i$.

The computational cost of the offline/online phases depends on the number of the reduced coefficients and it results different for the three techniques due to the following aspects.

- **Offline phase**

- pRB MOR: the offline phase divides into two stages. In the first stage the computational cost is due to the non-linear analyses. For each analysis the micromechanical inelastic fields are stored for every time step in order to perform the snapshot POD to determine the spatial distribution of

the inelastic modes. The second stage is characterized by linear pre-analyses depending on the number of inelastic modes. The spatial distribution of the inelastic modes as well as the localization tensors of every point of the RVE need to be stored at the end of the offline phase.

- NUTFA: only linear elastic pre-analyses are performed, whose number is related to the number of the selected inelastic modes. Furthermore, the storage of the localization tensors for every point of the domain is required.
 - MxTFA: only linear elastic pre-analyses are performed, whose number is related to the number of the selected stress modes. Unlike the other two techniques, only the strain coefficients for every subset (see Eq.39) are stored.
- Online phase
 - pRBMOR: the resolution of the nonlinear evolution problem is performed at RVE level in order to obtain the reduced coefficients.
 - NUTFA: the evolution problem is solved locally at each Gauss point of each subset.
 - MxTFA: the evolution equations are solved globally at the subset level.

A schematic comparison of the three proposed techniques is reported in Table 14, while Table 15 focuses on the main pros and cons of the three techniques in the offline and online phase.

4.6 NUMERICAL APPLICATIONS

This Section is devoted to the assessment of the efficiency of the pRBMOR, NUTFA and MxTFA in determining the effective response of periodic composites subjected to periodic boundary conditions. A 3D geometry consisting of an elastic inclusion embedded into a viscoplastic matrix is considered. The UC represents a metal-ceramic composite, a class of materials that are used in different applications such as cutting tools (due to the hard inclusions), or self-lubricated bearings. The UC is subjected to different load cases. The first two load cases were presented in a previous study [30], involving normal loading histories: here the effective response of the material obtained from the three methods is compared with the one obtained from a nonlinear FE analysis. The remaining two load cases are characterized by combined normal and shear loading: here only the MxTFA and pRBMOR procedures are compared.

Table 14: Schematic comparison of the three methods.

	pRBMOR (Section 4.2)	NUTFA (Section 4.3)	MxTFA (Section 4.4)
reduced DOF!	ξ, λ	$\tilde{\pi}^{j,i}$	$\hat{\sigma}, \hat{\gamma}$
# of reduced DOF!	$N_\mu + N_\alpha$	$6 \sum_{j=1}^n N_\pi^j + N_h$	$\sum_{j=1}^n N_p^j + \sum_{j=1}^n N_p^j$
pre-analyses	nonlinear & linear	linear	linear
modes	pre-computed	analytical	analytical
evolution of reduced DOF!	mixed variational formulation	L^2 minimization	mixed variational formulation
effective stress	via constitutive law see (100)	via constitutive law see (105)-(106)	via reduced DOFs see (56)
local constitutive model solved?	no	yes	no
effective tangent stiffness operator?	yes (inexpensive)	not yet	yes (inexpensive)
extension to non Generalized Standard Materials (GSM)	no (Φ^* needed)	yes	no (Φ^* needed)

Table 15: Pros and Cons in the offline and online phase.

technique	offline phase	online phase	
	small \tilde{N}	reduced computational effort for the evolution phase	PROs
pRBMOR (Section 4.2)	non linear pre-analyses: # and type is user defined affect the mode accuracy store $L_{\tilde{\epsilon}}(\mathbf{x}), L_\pi(\mathbf{x}), \mu(\mathbf{x})$ and $\alpha(\mathbf{x})$	local nonlinear computations (see Eq. 98)	CONs
	linear pre-analyses	easy to be extended to non GSM	PROs
NUTFA (Section 4.3)	large # of pre-analyses store $L_{\tilde{\epsilon}}^g(\mathbf{x})$ and $L_{\tilde{\pi}^{j,i}}^g(\mathbf{x})$	larger \tilde{N} evolution problem solved locally	CONs
	linear pre-analyses store $\tilde{\epsilon}^j$	reduced computation effort for the evolution phase fast stresses computation	PROs
MxTFA (Section 4.4)	large # of pre-analyses	larger \tilde{N} large system of equations (??)	CONs

Table 16: Material properties of the constituents.

	E [GPa]	ν -	σ_y [MPa]	H [MPa]	σ_D [MPa]	ϵ -	$\dot{\epsilon}_0$ [s ⁻¹]
Inclusion (elastic)	400	0.2	-	-	-	-	-
Matrix (viscoplastic)	75	0.3	90	500	10	20	0.02

4.6.1 Ceramic inclusion in viscoplastic matrix

The UC consists in a spherical ceramic inclusion embedded in a viscoplastic matrix, with volume fraction equal to 17.3%. The material properties are collected in Table 16 while Figure 33a and 35a show the problem geometry and the FE discretization respectively. In particular, the UC has been discretized employing 6096 ten-node quadratic tetrahedral elements with four integration points and 9057 nodes. In particular, 1216 elements are used in order to discretize the inclusion and 4880 for the matrix. The number of internal variables for the finite element analysis is 31360.

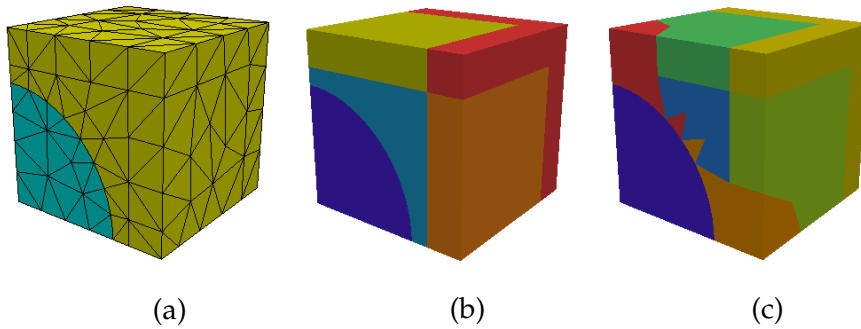


Figure 35: Unit cell made of elastic inclusion and plastic matrix (one eighth): (a) FE discretization; (b) NUTFA subset partitioning; (c) MxTFA subset partitioning.

MICROSTRUCTURAL CONSTITUTIVE MODEL A viscoplasticity framework combined with linear hardening is considered. Therefore $f = f(\sigma, r)$, $\Phi^* = \Phi^*(\sigma, r)$ and the evolution laws for the plastic strain π

and for the hardening variable α are given by the generalized gradients of the potential $\Phi^*(\boldsymbol{\sigma}, r)$.

$$\dot{\boldsymbol{\pi}} = \frac{\partial \Phi^*(\boldsymbol{\sigma}, r)}{\partial \boldsymbol{\sigma}}, \quad \dot{\alpha} = -\frac{\partial \Phi^*(\boldsymbol{\sigma}, r)}{\partial r}. \quad (107)$$

In this work we consider the following dissipation potential:

$$\Phi^*(\boldsymbol{\sigma}, r) = \begin{cases} \sqrt{\frac{2}{3}} \frac{\dot{\epsilon}_0 \sigma_D}{\epsilon+1} \left(\frac{f(\boldsymbol{\sigma}, r)}{\sigma_D} \right)^{\epsilon^*+1} & f(\boldsymbol{\sigma}, r) > 0 \\ 0 & f(\boldsymbol{\sigma}, r) \leq 0 \end{cases} \quad (108)$$

with $\dot{\epsilon}_0$ being a reference strain rate, $\epsilon^* = 1/\epsilon$ a dimensionless rate sensitivity parameter and σ_D a (constant) drag stress. Then (107) and (108) lead to:

$$\dot{\alpha} = \sqrt{\frac{2}{3}} \dot{\epsilon}_0 \left(\frac{f(\boldsymbol{\sigma}, r)}{\sigma_D} \right)^{\epsilon^*} \quad (109)$$

$$\dot{\boldsymbol{\pi}} = \sqrt{\frac{2}{3}} \dot{\epsilon}_0 \left(\frac{f(\boldsymbol{\sigma}, r)}{\sigma_D} \right)^{\epsilon^*} \frac{\partial f(\boldsymbol{\sigma}, r)}{\partial \boldsymbol{\sigma}} = \dot{\alpha} \mathbf{N} \boldsymbol{\sigma}. \quad (110)$$

PRBMOR For the pRB MOR a total of ten different loadings was considered in the nonlinear pre-analyses stage. The loading cases comprise purely volumetric loading, six different deviatoric loadings and uniaxial extension in the three coordinate directions [see 30, for details]. The snapshot POD was used to extract a total of 32 plastic modes and 16 hardening modes (and subsets thereof). During the pre-analyses the plastic strain field and the field information of the hardening variable $\alpha(\mathbf{x})$ must be stored. The outputs of the POD and of the subsequent linear pre-analyses stage comprise the plastic strain modes, the self-equilibrated stress fields and the hardening modes. Each of these is technically realized through an integration point-wise defined matrix. Additional (but not required) outputs are the related (total) strain fields. Further, the effective elastic stiffness matrix and the matrix $\hat{\mathbf{D}}$ (99) are pre-computed.

In total the reduced model for the considered example has $\bar{\mathbf{N}} = 32 + 16 = 48$ internal variables, i.e. the full field information can be recovered from these 48 scalars in an inexpensive post-processing step.

NUTFA For the NUTFA procedure the plastic matrix is divided into 40 subsets. Figure 35b illustrates one eighth of the unit cell with the subdivision in subsets. Two different combinations of approximation functions, denoted in the following as NUTFA 4 and NUTFA 4-10-20, are used in the computations. NUTFA 4 considers four linear modes for the inelastic modes in each subset, while NUTFA 4-10-20 approximates the inelastic strain using:

- in the 8 subsets surrounding the elastic inclusion, cubic inelastic modes are introduced;

- in the 24 subsets along the sides of the UC quadratic modes are used;
- in the remaining 8 subsets along the edges of the UC linear functions are adopted.

The inelastic modes are linearly independent but neither orthogonal nor normalized. The number of variables that are stored in the analysis is 960 for NUTFA 4 and 2592 for NUTFA 4-10-20 plus 4×6096 internal variables, in both cases.

The linear elastic analyses required to evaluate the the localization operators are performed using the same finite element mesh described previously. In particular, the total number of pre-analyses is equal to 984 and 1622 for NUTFA 4 and NUTFA 4-10-20 respectively, and for both combinations, the localization operators $\mathbf{L}_{\xi}^g(\mathbf{x})$ and $\mathbf{L}_{\bar{\pi},i}^g(\mathbf{x})$ are stored for the 4×6096 integration points of the UC.

MxTFA For the MxTFA homogenization analysis the UC is subdivided into 65 subsets, 1 for the inclusion and 64 for the matrix: the subset partitioning for one eighth of the UC is shown in Figure 35c. As for the stress distribution over the subsets, two different combinations are used. For the first combination, denoted as MxTFA 21, linear modes for all the subsets are employed, while cubic modes for the matrix and linear modes for the inclusion are used in the second combination termed MxTFA 21-117. According to these two combinations, the MxTFA model is described by $\bar{\mathbf{N}} = 1344$ and $\bar{\mathbf{N}} = 7552$ internal variables respectively.

For both combinations, the approximation matrix $\mathbf{\Pi}^j$ describing the distribution of the approximated perturbation strain $\tilde{\boldsymbol{\epsilon}}^j$ is chosen equal to \mathbf{P}^j . Also in this case, the linear elastic analyses are performed using the same finite element mesh described previously. For the first combination (MxTFA 21), $N_\rho = 1$ and $N_p = 21$, $N_l = 21$ for all the 65 subsets, resulting in $(6 + N_p) \times n = 1371$ analyses. For the second combination (MxTFA 21-117), being $N_p = 21$ for the inclusion, $N_p = 117$ for all the other subsets and $N_\rho = 1$, the total number of analyses is 7515. At the end of the pre-analyses $N_l \times 6$ and a $65 \times N_l \times N_p$ coefficients matrices for every subset are stored for the MxTFA analysis.

4.6.1.1 Load case 1

A complex loading/unloading strain history is prescribed to the UC, as described in Table 17.

Figure 36 shows the comparisons for the macroscopic stress components for the NUTFA, MxTFA and pRB MOR. A good agreement between the reduced models predictions and the FE reference solution can be observed. In particular, the left side shows the effective stress component, while on the right its corresponding deviatoric counterpart

Table 17: Load case 1 (LC-1) (data cf. [30], LC-2 for the 3D UC).

Time [s]	$\bar{\epsilon}_{11}$	$\bar{\epsilon}_{22}$	$\bar{\epsilon}_{33}$	$2\bar{\epsilon}_{12}$	$2\bar{\epsilon}_{23}$	$2\bar{\epsilon}_{13}$
0	0	0	0	0	0	0
1	0.02	0	0	0	0	0
2	0.02	0.01	0.01	0	0	0
3	0.01	0.01	0.01	0	0	0
4	0.00	0	0	0	0	0
5	-0.01	0	0	0	0	0

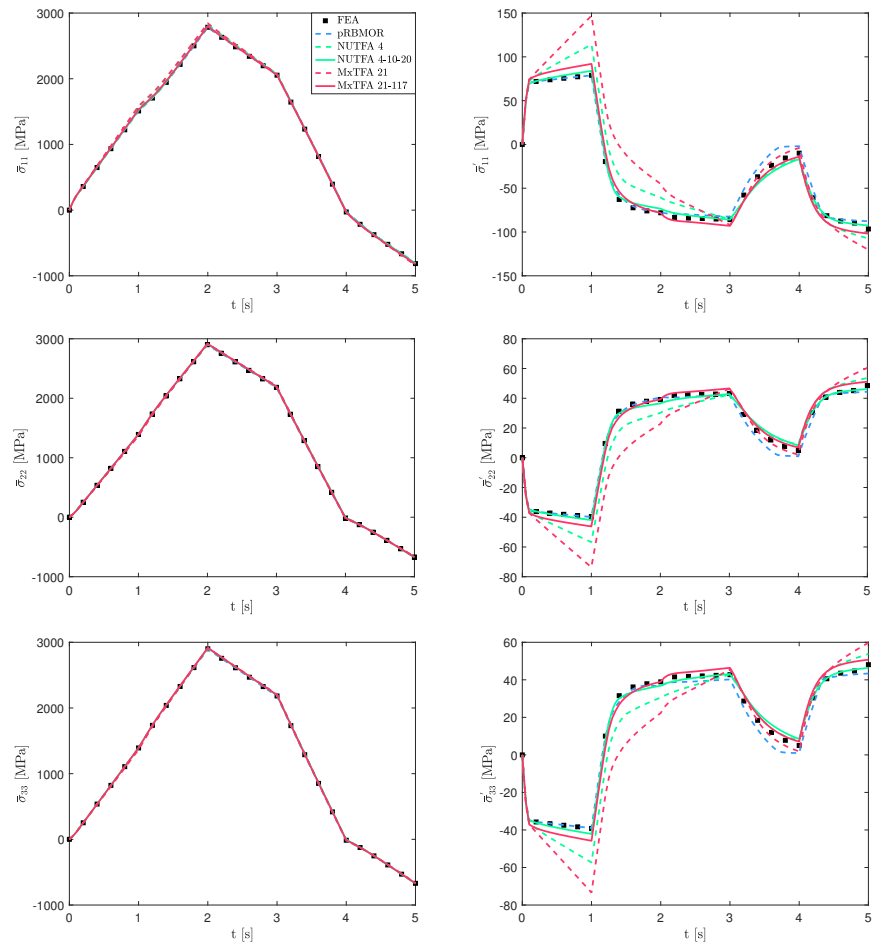


Figure 36: Load case 1: Comparison of the results between the FE and the model order reduction methods (pRB MOR, NUTFA and MxTFA) in terms of effective response (left) and corresponding deviator (right) .

Table 18: Load case 2 (LC-2) (data cf. [30], LC-3 for the 3D UC).

Time [s]	$\bar{\epsilon}_{11}$	$\bar{\epsilon}_{22}$	$\bar{\epsilon}_{33}$	$2\bar{\epsilon}_{12}$	$2\bar{\epsilon}_{23}$	$2\bar{\epsilon}_{31}$
0	0	0	0	0	0	0
1	0.02	0	0	0	0	0
2	0.02	-0.01	0.01	0	0	0
3	0.01	-0.01	0.01	0	0	0
4	0.00	0	0	0	0	0
5	-0.01	0	0	0	0	0

is reported. As expected, increasing the number of modes allows for better results, especially in terms of deviatoric stress. Nevertheless, as far as the effective stress prediction is concerned, NUTFA 4 and MxTFA 21 are already able to accurately reproduce the macroscopic response of the UC.

4.6.1.2 Load case 2

Also for this second load case, a 5-step complex loading/unloading strain history is prescribed to the UC (see Table 18).

The effective stress components as well as their deviatoric parts are collected in Figure 37. Also in this case, the three techniques prove to be very efficient in the resolution of the micromechanical problem. The better performance of the enriched-basis combination, especially in the deviatoric components, is also confirmed.

4.6.1.3 Load case 3

In the third load case, the UC is subjected to a loading/unloading involving both normal and shear strains as detailed in Table 19. For this load case, the attention is focused on the pRBMOR and the MxTFA only (for the latter, only the first combination MxTFA 21 is employed). Figure 38 shows the comparison of the results between the FE analysis and the reduced model analyses. In particular, only one normal component is shown thanks to symmetry and its deviatoric counterpart is not reported as it is zero for this load case. Both models are able to reproduce the overall response of the UC for both the normal and the shear stress components.

The local distribution of selected stress and inelastic strain components is shown for $t = 2s$ in Figs. 39-42, where the local distribution provided by pRBMOR and MxTFA are compared with the FEA reference solution. Unlike the prediction of the effective stress, where all the techniques proved to be equally efficient, it can be observed that for this specific for UC geometry, material properties and Load

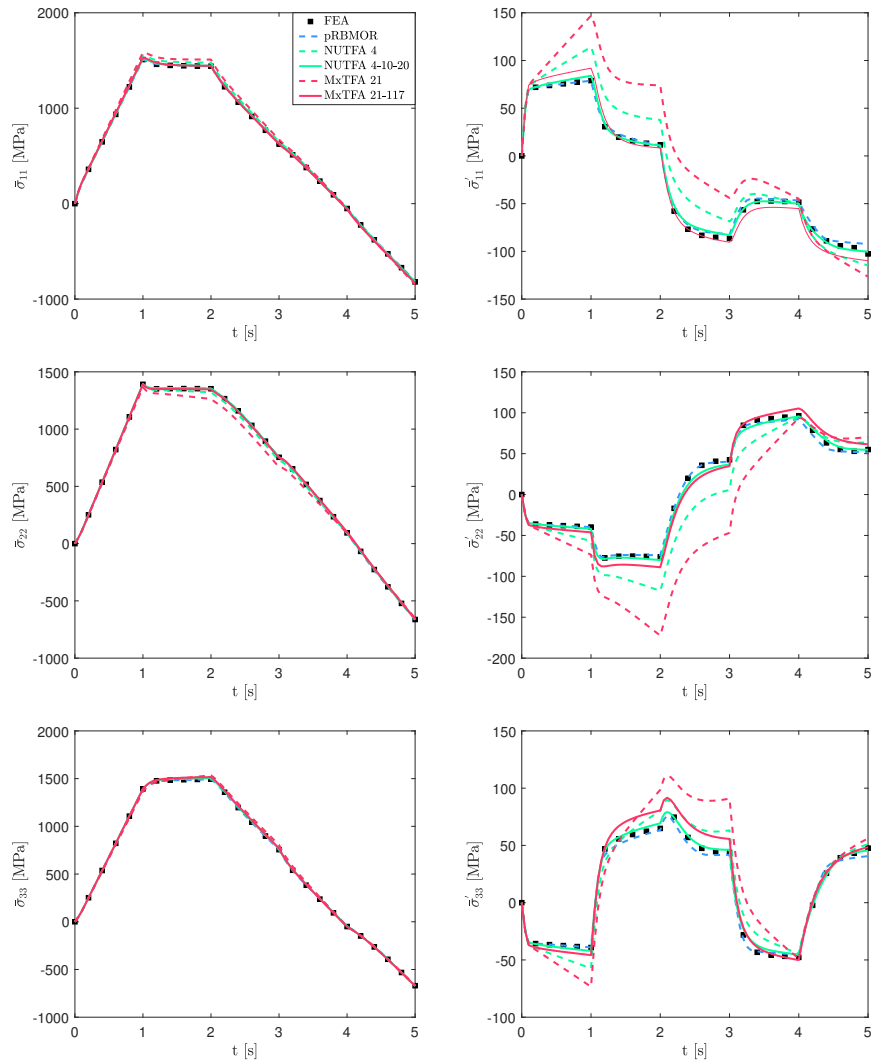


Figure 37: Load case 2: Comparison of the results between the FE and the model order reduction methods (pRB MOR, NUTFA and MxTFA) in terms of effective response (left) and corresponding deviatoric components (right) .

Table 19: Load case 3 (LC-3).

Time [s]	$\bar{\epsilon}_{11}$	$\bar{\epsilon}_{22}$	$\bar{\epsilon}_{33}$	$2\bar{\epsilon}_{12}$	$2\bar{\epsilon}_{23}$	$2\bar{\epsilon}_{13}$
0	0	0	0	0	0	0
1	0	0	0	$\sqrt{2} \cdot 0.01$	0	0
2	0.01	0.01	0.01	$\sqrt{2} \cdot 0.01$	0	0
3	0.01	0.01	0.01	0	0	0
4	0	0	0	0	0	0

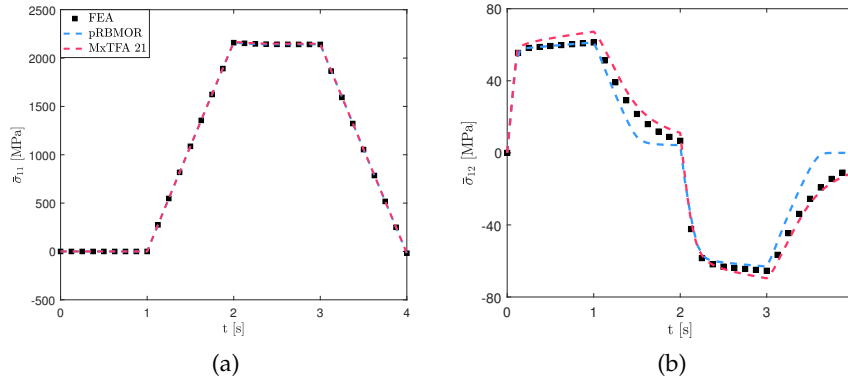


Figure 38: Load case 3 - Comparison of the results between the FE and the model order reduction methods (pRB MOR and MxTFA) in terms of effective response.

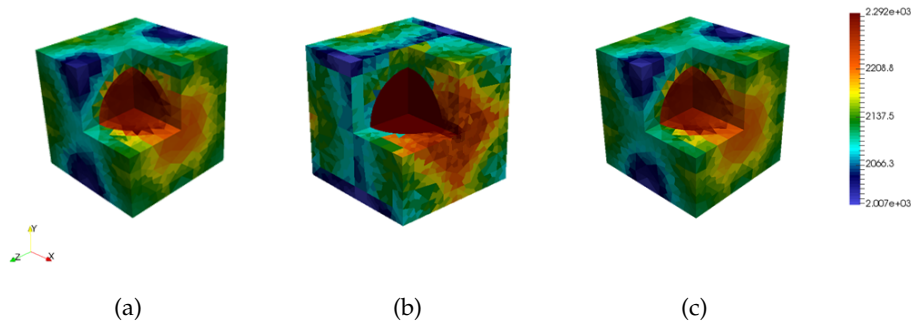


Figure 39: Load case 3 - Local distribution of stress component σ_{11} [MPa] at $t = 2$ s: (a) FEA, (b) MxTFA and (c) pRB MOR.

Case, the pRB MOR is able to better capture the distribution of the micromechanical fields.

4.6.1.4 Load case 4

Also in this load case, the effective response of the UC under a loading history involving both normals and shear strains for the pRB MOR and the MxTFA (MxTFA 21 only) is investigated. The load case is detailed in Table 20. The comparison of the results between the FE solution and the reduced models solution in terms of normal and shear stress components is shown in Figures 43 and 44 respectively. The results show a good agreement between the predictions. It could be noted that, the MxTFA 21 is not perfectly able to capture the behavior of the deviatoric stress components, but results in the previous load cases show that this could be overcome by enriching the basis. It could be emphasized that, in the framework of multiscale analysis, two key points become important: the average stress should be accurately evaluated

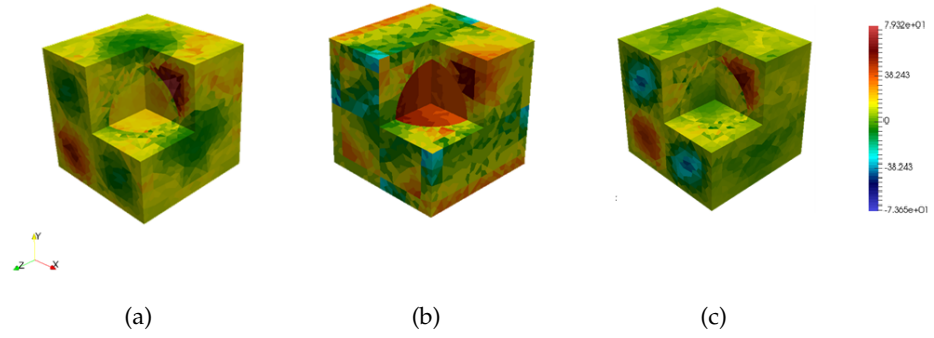


Figure 40: Load case 3 - Local distribution of stress component σ_{12} [MPa] at $t = 2s$: (a) FEA, (b) MxTFA and (c) pRB MOR

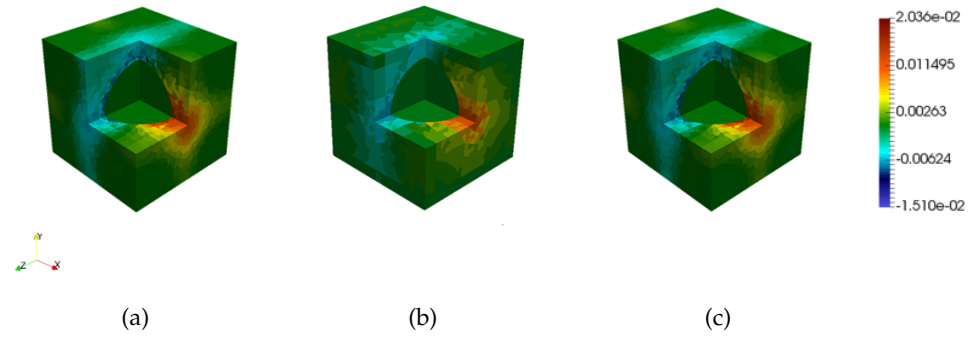


Figure 41: Load case 3 - Local distribution of inelastic strain component π_{11} at $t = 2s$: (a) FEA, (b) MxTFA and (c) pRB MOR

(less important is the accuracy of the deviatoric part), the computational effort should be as reduced as possible.

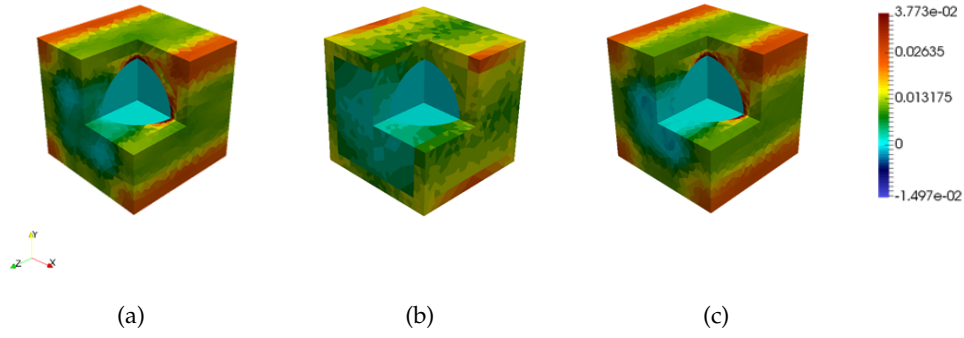


Figure 42: Load case 3 - Local distribution of inelastic strain component π_{12} at $t = 2s$: (a) FEA, (b) MxTFA and (c) pRBMOR

Table 20: Load case 4 (LC-4).

Time [s]	$\bar{\epsilon}_{11}$	$\bar{\epsilon}_{22}$	$\bar{\epsilon}_{33}$	$2\bar{\epsilon}_{12}$	$2\bar{\epsilon}_{23}$	$2\bar{\epsilon}_{13}$
0	0	0	0	0	0	0
1	0	0	0	$\sqrt{2} \cdot 0.01$	0	$-\sqrt{2} \cdot 0.01$
2	0.01	0.01	0.	$\sqrt{2} \cdot 0.01$	0	$-\sqrt{2} \cdot 0.01$
3	0.01	0.01	0	0	0	0
4	0.0	0	0	0	0	0

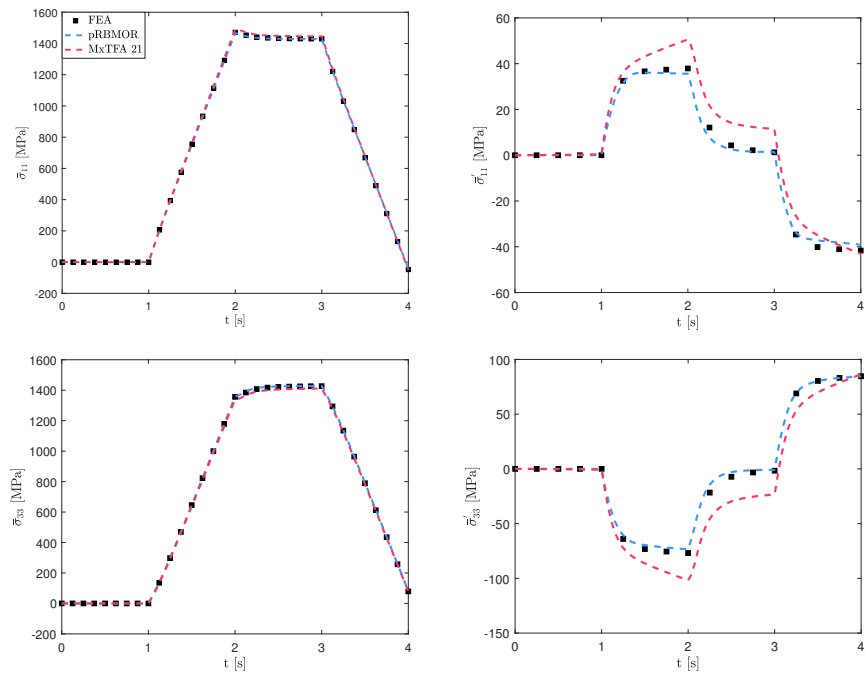


Figure 43: Load case 4: Comparison of the normal components between the FE and the model order reduction methods (pRB MOR and MxTFA) in terms of effective response (left) and corresponding deviatoric part (right).

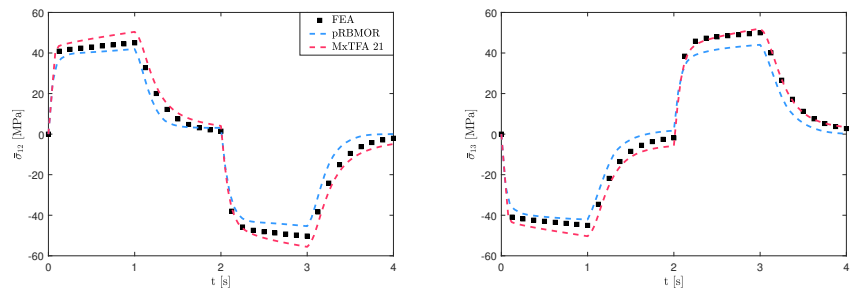


Figure 44: Load case 4: Comparison of the shear components between the FE and the model order reduction methods (pRB MOR and MxTFA).

In this Chapter, the problem addressed in Chapter 2 is solved employing a new multiscale method. The presented technique involves the MxTFA detailed in Chapter 3 at the microscale, in order to derive the global response by taking into account for the nonlinearities occurring at its microscale due to a heterogeneous microstructure. Some numerical examples show the accuracy and efficiency of the technique.

5.1 MICROSACLE: MXTFA

As detailed in Chapter 2, the constitutive equations are written only at the microscopic scale, and the relation between the effective stress $\bar{\sigma}$ and effective strain $\bar{\epsilon}$ is derived via MxTFA presented in Chapter 3.

5.1.1 Algorithmic tangent stiffness

Once the effective stress $\bar{\sigma}$ is derived for the generic RVE employing Eq. (56), the algorithmic tangent stiffness $\bar{\mathbf{C}}$ providing the linearization of the relationship between the effective stress $\bar{\sigma}$ and the effective strain $\bar{\epsilon}$ is derived as:

$$\bar{\mathbf{C}} = \frac{\partial \bar{\sigma}}{\partial \bar{\epsilon}}. \quad (111)$$

The evaluation of $\bar{\mathbf{C}}$ is required in order to evaluate the stiffness matrix of the structure at the macroscale. The MxTFA can provide its evaluation at no additional computational cost. From (56) and (111) it results:

$$\bar{\mathbf{C}} = \frac{1}{\Omega} \sum_{j=1}^n \bar{\mathbf{P}}^j \frac{\partial \hat{\sigma}^j}{\partial \bar{\epsilon}}. \quad (112)$$

The only term that needs to be calculated is $\frac{\partial \hat{\sigma}^j}{\partial \bar{\epsilon}}$, that is derived considering a perturbation of the macroscopic strain $\bar{\epsilon}$ in the nonlinear system (48)-(49):

$$\begin{aligned} d\mathbf{R}^j(\mathbf{U}^i, \bar{\epsilon}) &= d\mathbf{R}^j(\hat{\sigma}^i, \Delta\hat{\gamma}^i, \bar{\epsilon}) \\ &= \left(\frac{\partial \mathbf{R}^j}{\partial \hat{\sigma}^i} \frac{\partial \hat{\sigma}^i}{\partial \bar{\epsilon}} + \frac{\partial \mathbf{R}^j}{\partial \Delta\hat{\gamma}^i} \frac{\partial \Delta\hat{\gamma}^i}{\partial \bar{\epsilon}} + \frac{\partial \mathbf{R}^j}{\partial \bar{\epsilon}} \right) d\bar{\epsilon} = \mathbf{o}, \end{aligned} \quad (113)$$

Then, the partial derivative of the stress parameters $\hat{\sigma}^i$ can be obtained from:

$$\begin{bmatrix} \frac{\partial \hat{\sigma}^i}{\partial \bar{\varepsilon}} \\ \frac{\partial \Delta \hat{\gamma}^j}{\partial \bar{\varepsilon}} \end{bmatrix} = - \begin{bmatrix} \frac{\partial \mathbf{R}_\sigma^j}{\partial \hat{\sigma}^i} & \frac{\partial \mathbf{R}_\sigma^j}{\partial \Delta \hat{\gamma}^i} \\ \frac{\partial \mathbf{R}_\gamma^j}{\partial \hat{\sigma}^i} & \frac{\partial \mathbf{R}_\gamma^j}{\partial \Delta \hat{\gamma}^i} \end{bmatrix}^{-1} \begin{bmatrix} \frac{\partial \mathbf{R}_\sigma^i}{\partial \bar{\varepsilon}} \\ \frac{\partial \mathbf{R}_\gamma^i}{\partial \bar{\varepsilon}} \end{bmatrix}. \quad (114)$$

In (114), the two derivatives of the residuals with respect to $\bar{\varepsilon}$ are:

$$\frac{\partial \mathbf{R}_\sigma^i}{\partial \bar{\varepsilon}} = - [(\bar{\mathbf{P}}^j)^T + \mathbf{J}^j] \delta_{ij}, \quad (115)$$

$$\frac{\partial \mathbf{R}_\gamma^i}{\partial \bar{\varepsilon}} = \mathbf{0}. \quad (116)$$

The matrices in (115) are constant matrices defined in (44).

5.2 MULTISCALE PROCEDURE

The implementation of the method involves two main steps:

- Step 1: linear elastic micromechanical finite elements analysis - Offline phase

The offline phase involves the modelling of the RVE microstructure (i.e. subset identification and micromechanical finite element discretization) in order to perform the pre-analyses. The pre-analyses are linear elastic finite element analyses aimed at obtaining the localization operators \mathbf{L}_ε^j and $\mathbf{L}_{\pi^i}^j$ for the generic subset Ω^j . Thanks to the perturbation strain approximation introduced in (39), only the strain coefficients collected in the vector $\hat{\varepsilon}^j$ need to be stored for all the subsets. This stage also involves the evaluation of all the constant matrices for each subset defined in (44) and (50).

- Step 2: Implementation of the MxTFA in a finite element code - Online phase

The online phase consists in the modeling of the structural problem. The structure is discretized into N_e finite elements and appropriate loading and boundary conditions are applied. Then structural problem is solved incrementally employing nonlinear finite elements (arbitrary finite element codes can be employed), where the significant variables are known at time t_n , and the unknowns at time t are determined by equilibrium recalling the constitutive relations.

Equilibrium of the structure at time t implies:

$$\mathbf{K} \Delta \bar{\mathbf{u}} = \mathbf{F}, \quad (117)$$

where:

$$\mathbf{K} = \sum_{e=1}^{N_e} \int_{\Omega_e} \mathbf{B}^T \bar{\mathbf{C}} \mathbf{B} d\Omega \quad (118)$$

is the global stiffness matrix of the structure, \mathbf{B} is the strain-displacement matrix and:

$$\mathbf{F} = - \sum_{e=1}^{N_e} \int_{\Omega_e} \mathbf{B}^T \bar{\boldsymbol{\sigma}} d\Omega \quad (119)$$

is the vector of the nodal forces. The only difference relies in the call to the constitutive model in order to determine $\bar{\boldsymbol{\sigma}}$ and $\bar{\mathbf{C}}$ for every point $\bar{\mathbf{x}}$. In fact, the MxTFA model is called instead of calling the standard constitutive model for each (macroscopic) integration point at each (macroscopic) iteration. At the end of each load step, the history parameters β^j and the hardening variable α^j (see Eqs. (47) and (46)) are stored for every subset, for each macroscopic integration point $\bar{\mathbf{x}}$.

A schematic view of the Online phase is given in Fig.45.

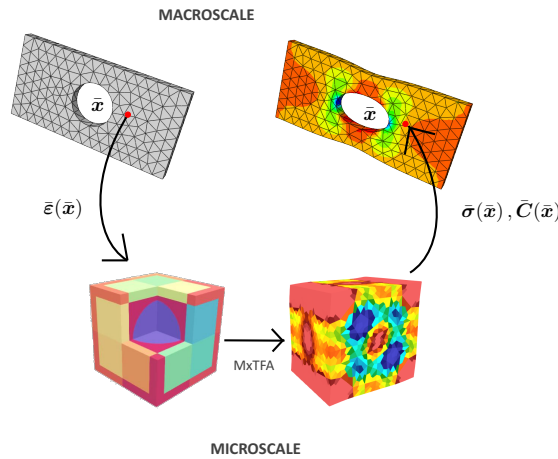


Figure 45: Multiscale Procedure: Graphical representation of the Online phase.

5.3 NUMERICAL RESULTS

This section is devoted to the assessment of the efficiency of the procedure in multiscale computations. The presented technique is implemented into FEAP. Two different periodic composites are considered, with different types of nonlinear materials. Because of the periodicity, the UC can be analyzed instead of the RVE, applying periodic boundary conditions. For both the UCs representing the two microstructures

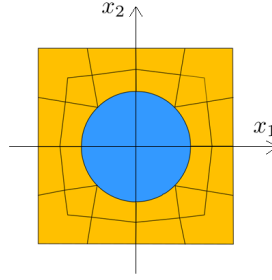


Figure 46: Microstructure A - Geometry and subset partitioning.

Constituent	E [GPa]	n	σ_y [MPa]	H [GPa]	μ [s]	ϵ
Inclusion	400	0.20	-	-	-	-
Matrix	70	0.30	480	2.085	500	0.1

Table 21: Microstructure A - Material properties for the constituents.

a linear stress approximation and a uniform plastic multiplier approximation is assumed for all the subsets. First, the response of the UCs evaluated via MXTFA for different loading histories is compared with the results obtained via micromechanical FEA. The same FE meshes adopted for the pre-analyses are used for the finite element micromechanical analyses. Then, two scale computations are performed for two different structural problems. At both scales, 2D four-node finite elements are employed.

5.3.1 UC analysis

Microstructure A is the same UC analyzed in [13], considering the viscoplastic model introduced by Perzyna [54] for the matrix and a rate sensitivity coefficient $\epsilon = 0.1$, combined with a linear isotropic hardening (hardening modulus $H = 2.085$ GPa). This UC has been discretized into $24+1$ subsets, resulting in $(7 + 1) \times 24 = 192$ internal variables. Fig. 46 and Table 21 illustrate the UC geometry and material properties.

Microstructure B derives from an hexagonal array distribution of elastic fibers in a plastic matrix with a volume fraction equal to 0.25, as shown in Fig. 47. The composite considered in this investigation is composed of coated silicon-carbide fibers (SCS-6 fibers produced by Textron) in a Ti-6Al-4V matrix. The material properties are the same of [51], summarized in Table 22. The UC was discretized into $18+1$ subsets as shown in Fig. 47, resulting in $(7 + 1) * 18 = 144$ internal variables.

For Microstructure A plane strain is assumed, while Microstructures B is analyzed in a plane stress framework.

First a monotonic loading along x_2 - direction is applied to the mi-

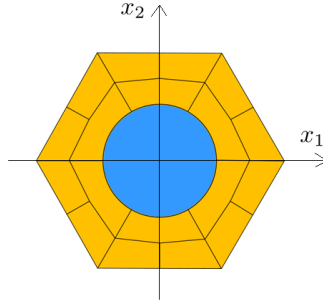


Figure 47: Microstructure B - Geometry and subset partitioning.

Constituent	E [GPa]	ν	σ_y [MPa]	H [GPa]
Inclusion	414	0.30	-	-
Matrix	113.7	0.30	900	4.6

Table 22: Microstructure B - Material properties for the constituents.

crostructures, and the results obtained with the MxTFA are compared with a nonlinear finite element analysis, as shown in Fig. 48. For this simple load case, a stress prediction given by the equivalent algorithmic tangent stiffness $\tilde{\mathbf{C}}$, evaluated from the MxTFA is also reported, where the effective stress $\bar{\boldsymbol{\sigma}}(t)$ is predicted from the effective stress $\bar{\boldsymbol{\sigma}}(t_n)$ as:

$$\bar{\boldsymbol{\sigma}}(t) = \bar{\boldsymbol{\sigma}}(t_n) + \tilde{\mathbf{C}}(t) \Delta \bar{\boldsymbol{\varepsilon}}. \quad (120)$$

Numerical results show that the MxTFA is able to provide a good resolution of the UC micromechanical problem. In fact, introducing the relative error with respect to the FEA solution as $\text{error} = (\bar{\sigma}_{ij}^{\text{FEA}} - \bar{\sigma}_{ij}^{\text{MxTFA}}) / \bar{\sigma}_{ij}^{\text{FEA}}$, the maximum error evaluated at the end of the monotonic loading history for the effective stress component $\bar{\sigma}_{11}$ results to be equal to 4.34% and 0.01% for Microstructure A and B, respectively. Analogously, the maximum relative error for the component $\bar{\sigma}_{22}$ is equal to 1.12% and 4.32% for the two microstructures. As for the tangent prediction, good agreement is also obtained setting $\Delta \bar{\boldsymbol{\varepsilon}} = 0.002$ in both the UC analyses. In particular, Figs. 48a and 48b show a stiffer response evaluated via stress prediction due to the rate dependent behavior of the matrix in Microstructure A, with a relative error compared to the MxTFA solution on the final effective stress equal to 3.15% and 3.34% for the two stress components $\bar{\sigma}_{11}$ and $\bar{\sigma}_{22}$. Figs. 48c and 48c show how the rate independent behavior of the matrix in Microstructure B determines a perfect agreement between the prediction and the MxTFA solution. Further computations demonstrate that in the limit as $\Delta \bar{\boldsymbol{\varepsilon}} \rightarrow 0$ the effective stress evaluated by Eq. ?? tends to the MxTFA solution, confirming the accuracy of the algorithmic

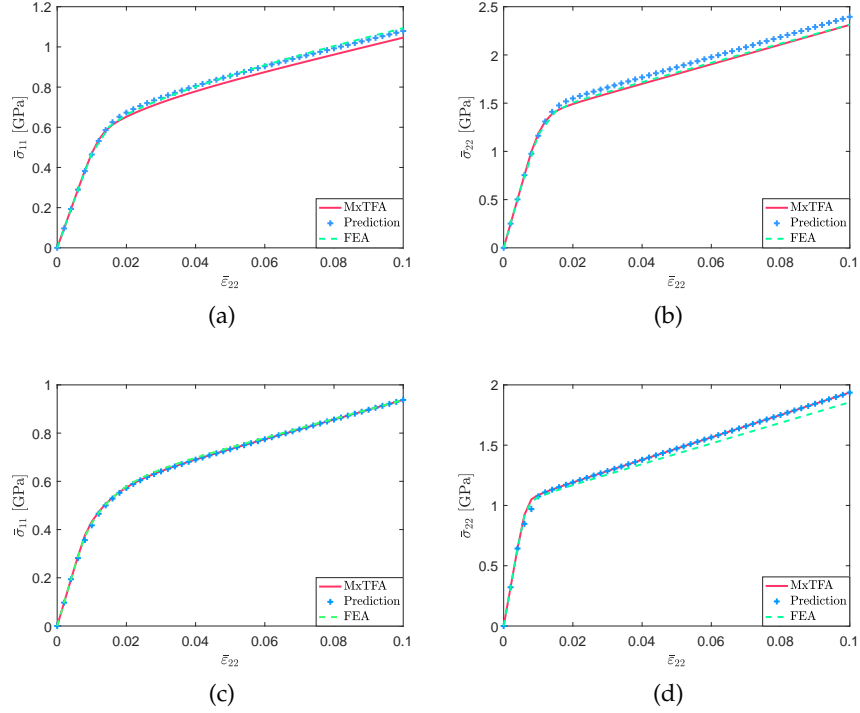
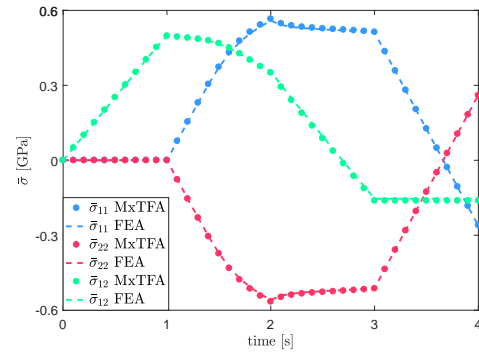


Figure 48: Stress prediction - (a) Microstructure A: $\bar{\sigma}_{11}$ [GPa], (b) Microstructure A: $\bar{\sigma}_{22}$ [GPa], (c) Microstructure B: $\bar{\sigma}_{11}$ [GPa], (d) Microstructure B: $\bar{\sigma}_{22}$ [GPa].

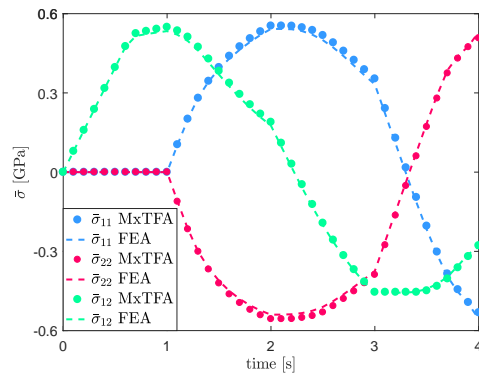
tangent stiffness. Then, a more complex loading history, characterized by combined normal and shear strain (shown in Table 23), is applied to the microstructures. The results of the UC homogenization analyses are reported in Fig. 49. In particular, the values of the effective stress components $\bar{\sigma}_{11}$, $\bar{\sigma}_{22}$ and $\bar{\sigma}_{12}$ are plotted versus time during the whole loading history for the two considered microstructures. Also in this case, good agreement can be observed between the MxTFA and FE solutions.

Table 23: Load case for Microstructure A and B.

Time [s]	$\bar{\epsilon}_{11}$	$\bar{\epsilon}_{22}$	$\bar{\epsilon}_{12}$
0	0	0	0
1	0	0	$\sqrt{2} \cdot 0.01$
2	0.01	-0.01	$\sqrt{2} \cdot 0.01$
3	0.01	-0.01	0
4	0	0	0



(a)



(b)

Figure 49: UC analysis - Mechanical response under loading/unloading of Table 23: (a) Microstructure A, (b) Microstructure B.

5.3.2 Multiscale analysis

The two microstructures analyzed in 5.3.1 are associated to two different structural problems, in order to assess the proposed multiscale procedure. In particular, Microstructure A is associated to the first structure, while Microstructure B is associated to the second problem.

5.3.2.1 Square tube

The square tube shown in Fig. 50 is considered. The tube is subjected to a distributed uniform load q and $-q$ on the top and bottom edges, respectively, acting along the vertical direction. Because of double symmetry of the problem, only the quarter of the cross section shown in Fig. 51a is analyzed under plane strain condition, setting $a = 10$ mm.

The multiscale analysis of the tube is performed discretizing the cross section into 75 finite elements, as shown in Fig. 51b. A load $q = 0.64$ kN/mm is first applied and then removed at a constant strain rate, in a time $t = 2$ s. The results obtained with the multiscale analysis (MS) are compared with a Nonlinear Finite Element structural Analysis (NFEA), where all the heterogeneities are discretized. Since the multiscale analysis implicitly assume a very small fiber diameter D with respect to the structural size (scale separation), herein two values of D are considered keeping the same volume fraction, in order to investigate to which extent the results obtained with a full structural NFEA could be compared with a MS analysis. In particular, inclusions of diameter size $D = 0.56$ mm and $D = 1.12$ mm are considered.

Table 24 shows the number of elements and of DOFs for the two different micromechanical discretizations as well as the ratio ξ between the fiber diameter D of the Nonlinear Finite Element structural Analysis (NFEA) discretizations and the finite element size in the MS. For lower fiber diameter D the ratio ξ tends to zero, as implicitly assumed in a multiscale procedure. For the two values of the diameter D of the inclusion, different number of elements is used in Nonlinear Finite Element structural Analysis (NFEA), as smaller elements are required in the discretization of the heterogeneous solid when D reduces.

Figure 52 shows the response of the cross-section of the tube in terms of the vertical displacement \bar{u}_2 of point P in Fig. 51a versus the load q . A good agreement between the results obtained by the different analyses is observed and, as expected, the Nonlinear Finite Element structural Analysis (NFEA) curves converge towards the MS solution, that is characterized by a significantly reduced number of variables and, then, of the computational cost in terms of time and memory. The influence of the rate dependency in the viscoplastic matrix is highlighted in Figure 53, where the same final load $q = 0.64$

Table 24: Properties of the micromechanical finite element discretization (Nonlinear Finite Element structural Analysis (NFEA)).

Fiber diameter D [mm]	No. of internal variables	No. of element	ξ
0.56	2457600	364800	0.28
1.12	614400	91200	0.56

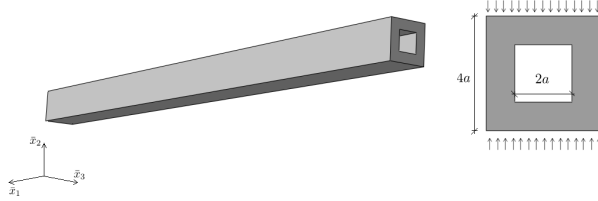


Figure 50: Square tube.

kN/mm is monotonically applied at different rates $\dot{q}_1 = 1.28$ and $\dot{q}_2 = 0.64$ kN/mm s (corresponding to a loading time equal to 0.5 s and 1 s, respectively), determining a different response in the material. In particular, a stiffer response is obtained for higher loading rates; in fact, the final value of \bar{u}_2 recovered by the MS solution is equal to 1.8263 mm and 2.0652 mm for \dot{q}_1 and \dot{q}_2 , respectively. This difference is further highlighted in materials with lower rate sensitivity coefficient ϵ . The results show that the multiscale analysis is able to give a good resolution of the problem for fiber diameter D of the same magnitude of the volume around the integration point of the macroscopic discretization; in other words, the MS results and the Nonlinear Finite Element structural Analysis (NFEA) with $D = 0.56$ mm are absolutely comparable.

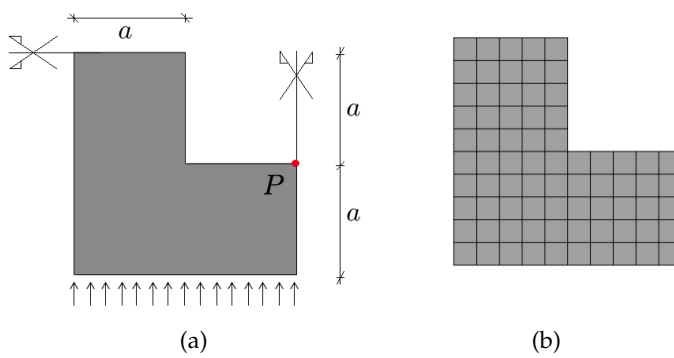


Figure 51: Square tube - (a) Problem geometry, (b) MS structural discretization.

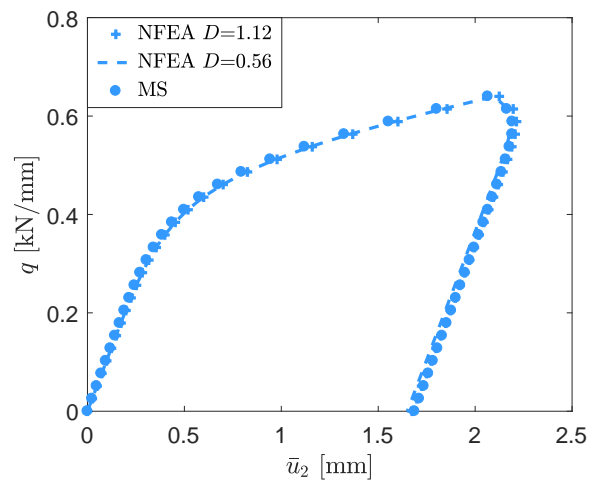


Figure 52: Square tube - Load/displacement curve.

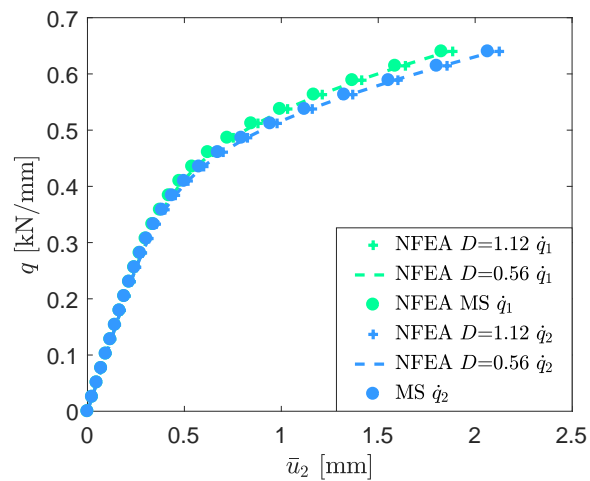


Figure 53: Square tube - Rate dependency: comparison between loading at different rates $\dot{q}_1 = 1.28$ and $\dot{q}_2 = 0.64$ [kN/mm s].

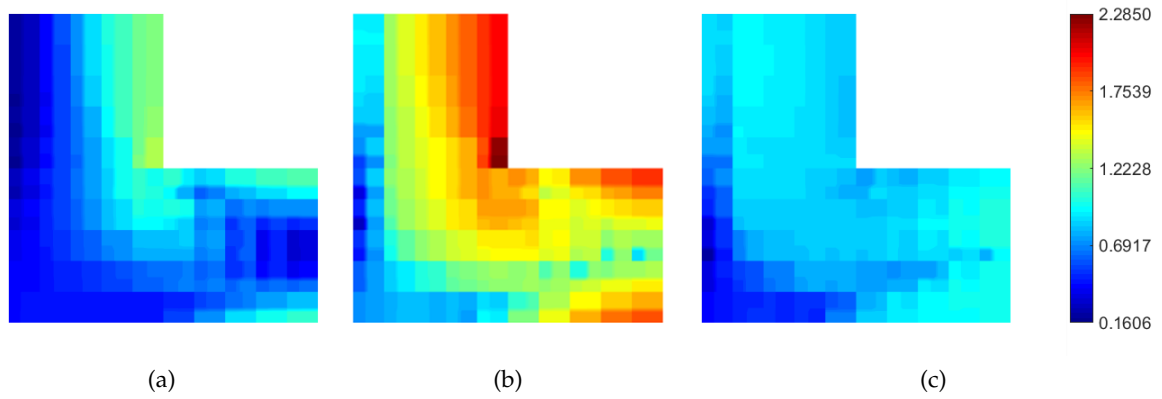


Figure 54: Square tube - Equivalent Stress [GPa]: (a) Load Step A ($q = 0.32$ kN/mm loading phase), (b) Load Step B ($q = 0.64$ kN/mm), (c) Load Step C ($q = 0.32$ kN/mm unloading phase).

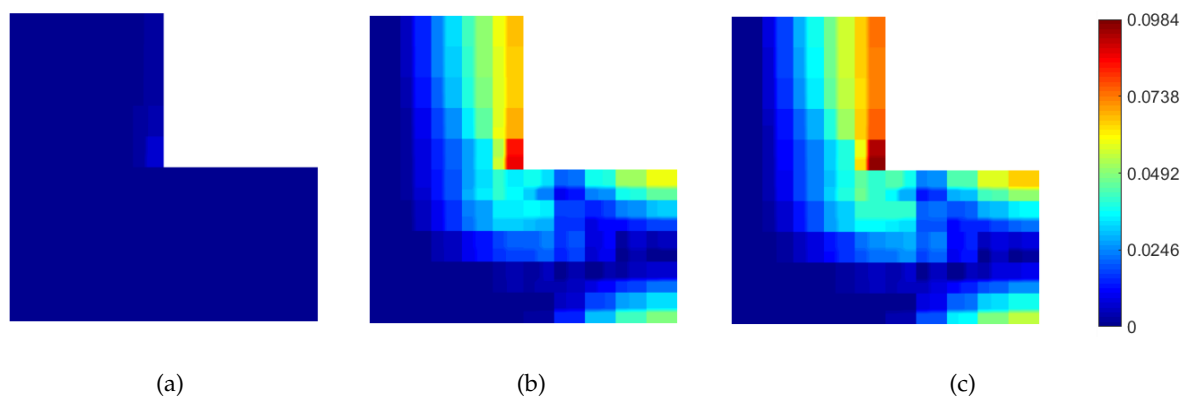


Figure 55: Square tube - Equivalent plastic strain : (a) Load Step A ($q = 0.32$ kN/mm loading phase), (b) Load Step B ($q = 0.64$ kN/mm), (c) Load Step C ($q = 0.32$ kN/mm unloading phase).

Figs. 54 and 55 show the local distribution of the (macro) equivalent stress $\bar{\sigma}_{eq}$ and inelastic strain $\bar{\pi}_{eq}$ at three different load steps, where $\bar{\pi}_{eq}$ is defined as:

$$\bar{\pi}_{eq} = \sqrt{\frac{2}{3} \bar{\pi}' \mathbf{M} \bar{\pi}}. \quad (121)$$

The first load step considered (Load Step A) corresponds to half of the final load ($q = 0.32$ kN/mm) in the loading phase, the second load step (Load Step B) corresponds to the end of the loading phase ($q = 0.64$ kN/mm) and the last load step (Load Step C) to half of the final load ($q = 0.32$ kN/mm) in the unloading phase. From Fig. 54a (Load Step A) a stress concentration in correspondence of the internal corner of the cross section can be detected, and yielding initiates in correspondence of this region, as confirmed by Fig. 55a. Figs. 54b and 55b show a further development of plastic regions in correspondence of the internal corners of the cross section at Load Step B, as a consequence of a load increase from $q = 0.32$ to $q = 0.64$ kN/mm. Load Step C belongs to the unloading phase; as expected, while the equivalent stress state is decreasing with respect to Load Step B (Fig. 54c), there is still the presence of inelastic (residual) deformations, as shown in Fig. 55c.

5.3.2.2 Perforated plate

A rectangular plate with a circular hole in the center, as shown in Fig. 56a, is considered. Only a quarter of the plate is analyzed under the plane stress condition, setting $a = 6$ mm. The quarter of plate is subjected to a prescribed vertical displacement \bar{u}^* applied at the top edge. The plate is discretized into 192 finite elements (see Fig. 56b) and the total stretch \bar{u}^* is incrementally applied, up to a value $\bar{u}^* = 0.2$ mm.

Thanks to the multiscale approach adopted, various level of analysis are accessible. The effective force-displacement curve showing the edge reaction R obtained via multiscale analysis is reported in Fig. 57, where the nonlinearity of the material at the macroscale can be clearly observed. At the microscale, the response of the UCs associated to the integration points of Elements 1 and 121 highlighted in Fig. 56b, (where higher stress and inelastic strain concentrations are expected) is reported in Figs. 58 and 59, respectively, in terms of effective stress components versus time of the analysis. The stress field of each integration point recorded during the analysis corresponds to the effective stress $\bar{\sigma}$ of the associated UC under the applied strain field $\bar{\epsilon}$. Two significant load steps are investigated: Load Step A ($\bar{u}^* = 0.1$ mm), at the onset of plasticity on the force-displacement curve in Fig. 57 and Load Step B ($\bar{u}^* = 0.2$ mm) at the end of the analysis. The average

edge load Q , corresponding to the plate reaction R , is evaluated at Load Step A and B as:

$$Q = \frac{R}{2a \times s}, \quad (122)$$

being $s = 1$ mm the plate unit thickness. As a result $Q_A = Q(A) = 0.4091$ and $Q_B = Q(B) = 0.5316$ kN/mm respectively. The equivalent (macro) stress and inelastic strain distribution is investigated for the two different Load Steps, as indicators of the distribution of plastic regions over the plate. Figs. 60-63 show their distribution for Load Step A and B. In addition, a focus on the stress and inelastic strain components of selected integration points for Element 1 and 121 (whose stress path is represented in magenta in Figs. 58 and 59) is also reported, where the stress components σ_{ij}^* are scaled with respect to Q_A and Q_B for the two Load Steps, in order to have a better insight on the local stress increment with respect to the average edge load. For Load Step A, higher stress concentrations can be found in correspondence of the bottom-right side of the hole (see Element 1), as shown in Fig 60. A initiation of a plastic zone in this region can be observed from Fig. 62, where the UC corresponding to intp #1 of Element 1 shows that all the subsets of the matrix reached yielding while the UC corresponding to Element 121 is not yet in plastic regime (i.e. no plastic subsets). At the end of the analysis (Load Step B), the development of a large plastic zone at the hole can be observed from Figs. 61 and 63. In particular it can be observed from Fig. 63 that the UC associated to Gauss point intp #1 of Element 1 is fully plastic, while in the UC associated to Gauss point intp #4 of Element 121 only four subsets reached yielding. It can be also remarked that for Load Step B, the minimum stress σ_{11}^* at intp #4 of Element 121 is about equal to -2, while the maximum stress σ_{22}^* at intp #1 of Element 1 is about equal to 3. Thus, a significant stress concentration can be noted in the composite at microscale, greater than the concentration expected from the analytical solution of an infinite elastic homogeneous plate with a hole subjected to unit pressure at infinity, which would be -1 and 3, respectively. In both the loading step cases, large gradients in the inelastic strain distribution can be detected at the interface between the matrix and the inclusion. A multiscale tool that allow for such inspections at local level can be useful in order to prevent microscopic failure.

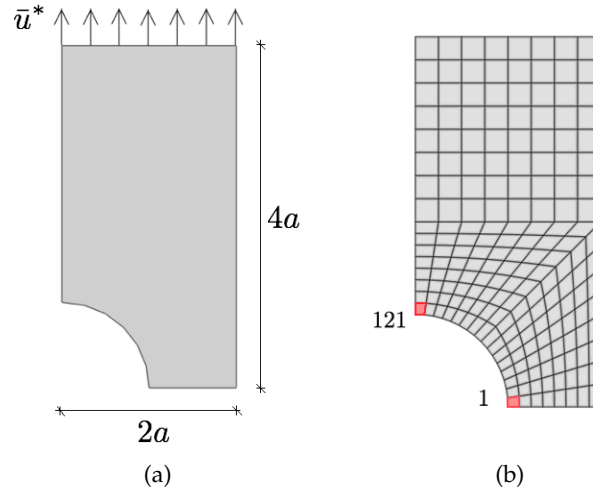


Figure 56: Perforated plate - (a) Problem geometry, (b) Structural discretization.

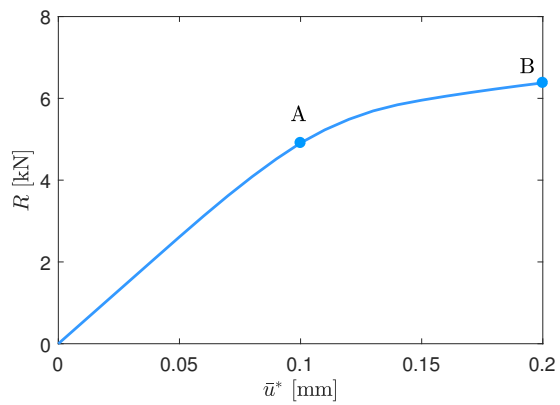
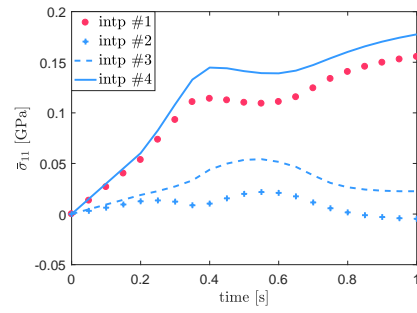
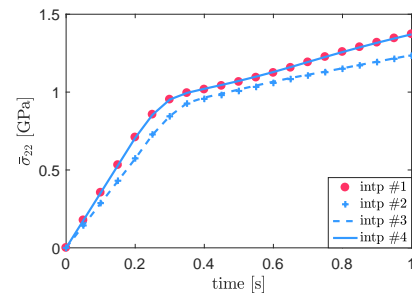


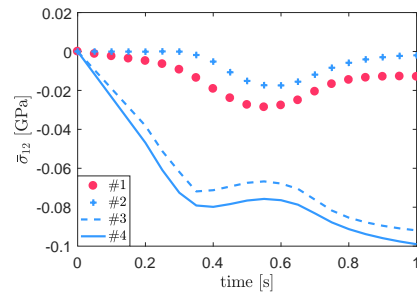
Figure 57: Perforated plate - force/displacement curve.



(a)

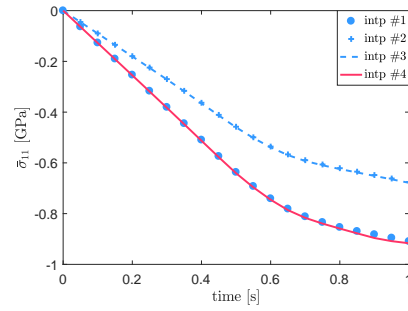


(b)

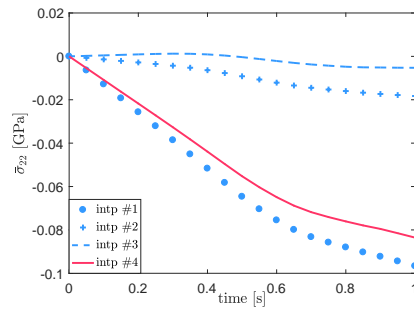


(c)

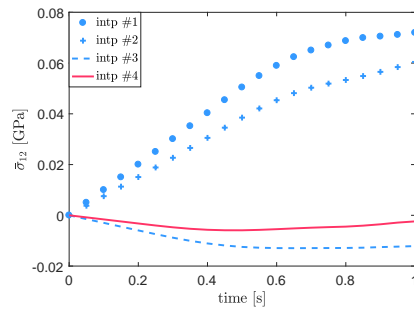
Figure 58: Perforated plate - Stress Components of the 4 integration points (intp) for Element 1: (a) $\bar{\sigma}_{11}$, (b) $\bar{\sigma}_{22}$, (c) $\bar{\sigma}_{12}$.



(a)



(b)



(c)

Figure 59: Perforated plate - Stress Components of the 4 integration points (intp) for Element 121: (a) $\bar{\sigma}_{11}$, (b) $\bar{\sigma}_{22}$, (c) $\bar{\sigma}_{12}$.

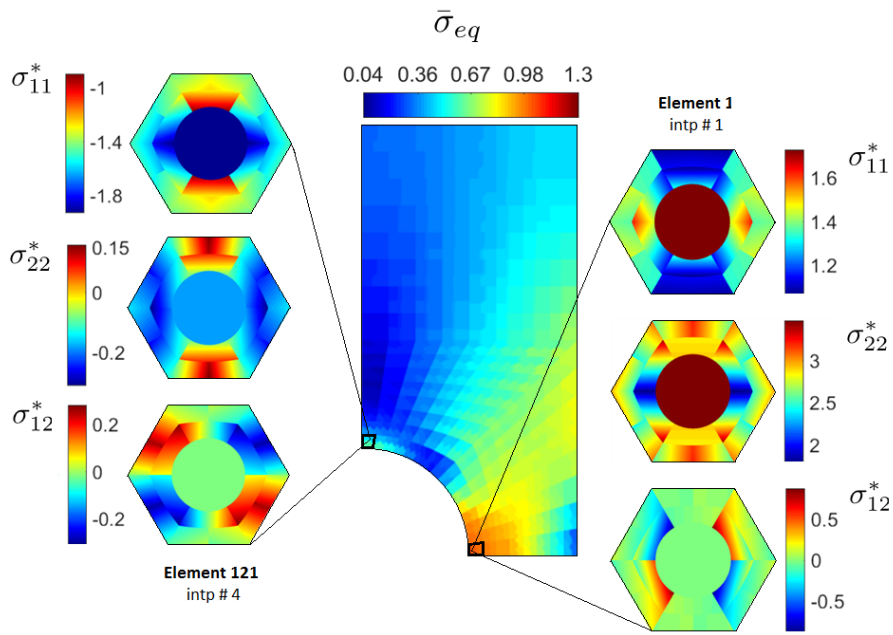


Figure 60: Perforated plate - Load Step A ($\bar{u}^* = 0.1$ mm): Macro equivalent stress [MPa] and Micro stresses $\sigma^* = \sigma/Q_A$.

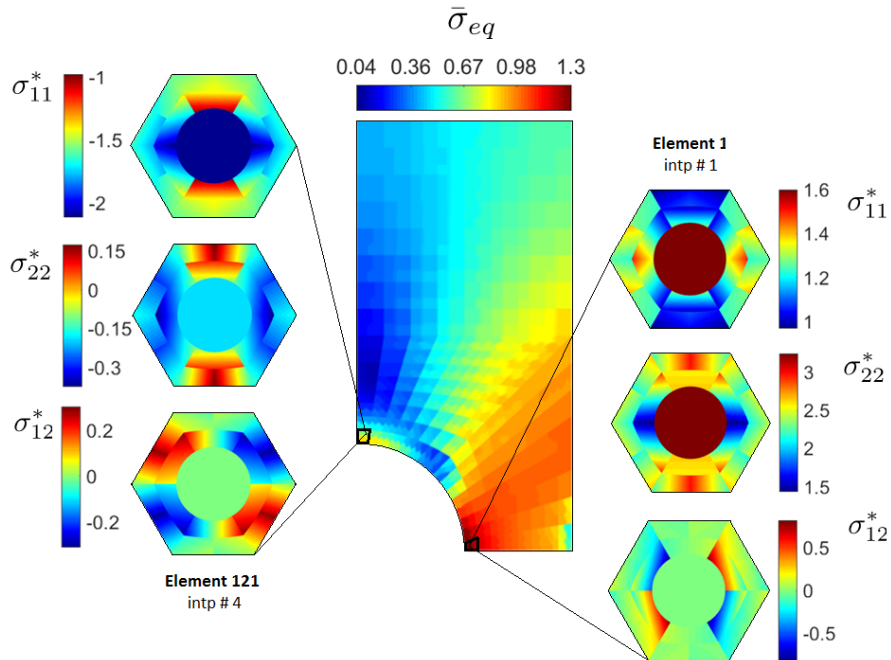


Figure 61: Perforated plate - Load Step B ($\bar{u}^* = 0.2$ mm): Macro equivalent stress [MPa] and Micro stresses $\sigma^* = \sigma/Q_B$.

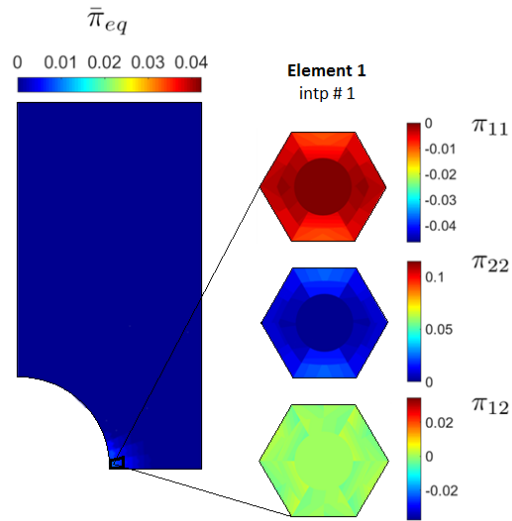


Figure 62: Perforated plate - Load Step A ($\bar{u}^* = 0.1$ mm): Micro - Macro Inelastic Strain.

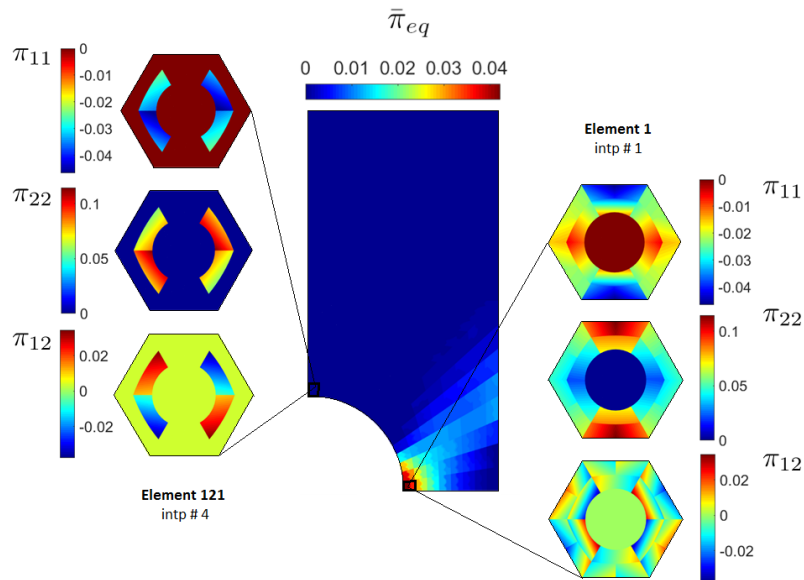


Figure 63: Perforated plate - Load Step B ($\bar{u}^* = 0.2$ mm): Micro - Macro Inelastic Strain.

SUMMARY AND CONCLUSIONS

This thesis investigates the homogenization problem for the multiscale analysis of nonlinear composites. The complexity of the problem is due to the existence of two scales (macroscale and microscale), that are assumed to be separated. In order to solve the mechanical problem at the macroscale, a deep understanding of the nonlinear phenomena occurring at the microscale is required. The resolution of a multiscale problem requires the definition of a homogenization scheme in order to provide the constitutive relation of an equivalent homogenized material. Homogenization techniques can be classified into analytical, computational and hybrid methods. Among the homogenization schemes here the focus is on a class of hybrid methods called Reduced Order Models (ROMs), aimed at the resolution of a reduced micromechanical problem. In particular, Transformation Field Analysis (TFA) techniques are considered, where the reduced variable is the inelastic strain.

Within this framework a new approach based on a mixed stress variational formulation named Mixed TFA (MxTFA) is introduced in Chapter 3. Since it is Nonuniform TFA (NTFA)-based, it allows to take into account for nonuniform distribution of the inelastic strain in the RVE. Some innovations have been introduced both in the approximation of the inelastic strain field and in the evaluation of the reduced internal variables of the problem. In particular, the approximation of the inelastic strain field derives from the assumed approximation for the stress and plastic multiplier, while in other TFA schemes the inelastic modes are directly assigned to this quantity. The evaluation of the reduced internal variables is performed based on a weak formulation of the evolution problem which is enforced over RVE subsets. At each time step the MxTFA procedure requires to solve a nonlinear system for all the subsets simultaneously, in order to determine the evolution of the reduced internal variables. The dimensions of the nonlinear system to be solved depends on the stress and plastic multiplier approximations assumed for every subset, while a classical Finite Element Analysis (FEA) solves the nonlinear evolution problem at each integration point of each finite element. This results in a reduction in terms of computational burden.

The numerical applications show the ability of the proposed MxTFA technique in reproducing the micromechanical nonlinear response for periodic composite characterized by Mises elasto-plastic and viscoplastic behavior combined with linear isotropic hardening under

monotonic and complex loading/unloading histories, in the prediction of both overall and local fields. In addition, from the results it can be highlighted that:

- Increasing the number of subsets the error with respect to the FEA solution is reduced.
- For the same number of internal variables, a basis enrichment leads to more accurate results. Once the RVE is fully plastic, while higher number of subsets is preferable at the onset of yielding.

Chapter 4 is dedicated to a comparative study between the MxTFA and two other homogenization techniques developed in the framework of the NTFA [47] for the analysis of viscoplastic composite media: the pRBMOR and the NUTFA. The key features as well as the differences of all techniques are described. The study highlighted that:

- Modes can be identified analytically or by a numerical training (simulating the nonlinear response of the RVE under prescribed loading paths).
- In case of analytical modes pre-analyses are linear elastic, to determine the localization operators; in case of numerically computed modes, nonlinear pre-analyses are also required.
- The effective stress is computed according to the reduced variables of the problem.

On the basis of the results shown in Chapters 3 and 4, the MxTFA is adopted within the framework of multiscale analysis to determine the overall response of a composite body in Chapter 5. In particular, a multiscale procedure is developed, where the MxTFA is implemented in a FE code in order to solve the micromechanical problem for the integration point of the macroscopic FE discretization. The advantage of using a multiscale approach is that both the macroscale and the microscale results can be easily accessed, resulting in a detailed analysis of global and local fields e.g. in order to estimate local damage before structural failure.

The novelty of the MxTFA technique presented in this thesis relies on the direct approximation of the auto-equilibrated stress fields rather than a direct inelastic strain approximation. To the author knowledge, there are no such schemes in the literature. The mixed-stress formulation translates in a more accurate stress prediction but also in a more straightforward evaluation of the overall stress and of the algorithmic tangent stiffness (which are required in order to solve the full multiscale problem).

In conclusion, the development of a reduced homogenization technique requires a compromise between theoretical rigor, computational cost and accuracy. This thesis opened a new direction for mixed schemes in the TFA context. Future developments of the proposed method could include:

- Extension to the analysis of composites characterized by general/random microstructure: in this case some modifications should be introduced in the procedure.
- Improvement of the strategy of subset partitioning (e.g. by incorporating pre-analysis data and snapshot POD).
- Improvement of the evolution procedure for the reduced variables.
- Introduction of a cohesive damage interface model in order to account for cracking and decohesion among constituents (this requires the introduction of new internal variables and evolution equations).

BIBLIOGRAPHY

- [1] D. Addressi, E. Sacco, and A. Paolone. "Cosserat model for periodic masonry deduced by nonlinear homogenization." In: *European Journal of Mechanics, A/Solids* 29 (2010), pp. 724–737.
- [2] M.M. Aghdam and S.R. Morsali. "Effects of manufacturing parameters on residual stresses in SiC/Ti composites by an elastic-viscoplastic micromechanical model." In: *Computational Materials Science* 91 (2014), pp. 62–67.
- [3] M. Agoras, R. Avazmohammadi, and P. Ponte-Castañeda. "Incremental variational procedure for elasto-viscoplastic composites and application to polymer- and metal-matrix composites reinforced by spheroidal elastic particles." In: *International Journal of Solids and Structures* (2016).
- [4] A. Benedetti, S. de Miranda, and F. Ubertini. "A posteriori error estimation based on the superconvergent recovery by compatibility in patches." In: *International Journal for Numerical Methods in Engineering* 67 (2006), pp. 108–131.
- [5] Peter Benner, Serkan Gugercin, and Karen Willcox. "A Survey of Projection-Based Model Reduction Methods for Parametric Dynamical Systems." In: *SIAM* 57 (2015), pp. 483–531.
- [6] Y. Benveniste. "A new approach to the application of Mori-Tanaka's theory in composite materials." In: *Mechanics of Materials* 6 (1987), pp. 376–396. 147–157.
- [7] J.R. Brockenbrough, S. Suresh, and H.A. Wienecke. "Deformation of metal-matrix composites with continuous fibers: geometrical effects of fiber distribution and shape." In: *Acta Metallurgica et Materialia* 39.5 (1991), pp. 735–752. ISSN: 0956-7151. DOI: [https://doi.org/10.1016/0956-7151\(91\)90274-5](https://doi.org/10.1016/0956-7151(91)90274-5). URL: <http://www.sciencedirect.com/science/article/pii/0956715191902745>.
- [8] B. Budiansky. "On the elastic moduli of some heterogeneous materials." In: *J Mech Phys Solids* 13 (1965), 223–227.
- [9] G. Castellazzi, S. de Miranda, and F. Ubertini. "Patch based stress recovery for plate structures." In: *Computational Mechanics* 47 (2011), pp. 379–394.
- [10] J. Chaboche, L.S. Kruch, J. Maire, and T. Pottier. "Towards a micromechanics based inelastic and damage modeling of composites." In: *International Journal of Plasticity* 17 (2001), pp. 411–439. DOI: [10.1016/S0749-6419\(00\)00056-5](https://doi.org/10.1016/S0749-6419(00)00056-5).

- [11] T. Christman, A. Needleman, and S. Suresh. "An experimental and numerical study of deformation in metal-ceramic composites." In: *Acta Metallurgica* 37.11 (1989), pp. 3029–3050. ISSN: 0001-6160. DOI: [https://doi.org/10.1016/0001-6160\(89\)90339-8](https://doi.org/10.1016/0001-6160(89)90339-8). URL: <http://www.sciencedirect.com/science/article/pii/0001616089903398>.
- [12] F. Covezzi, S. de Miranda, S. Marfia, and E. Sacco. "Complementary formulation of the TFA for the elasto-plastic analysis of composites." In: *Composite Structures* 156 (2016), pp. 93–100. DOI: <http://dx.doi.org/10.1016/j.compstruct.2016.01.094>.
- [13] F. Covezzi, S. de Miranda, S. Marfia, and E. Sacco. "Homogenization of elastic-viscoplastic composites by the Mixed TFA." In: *Computer Methods in Applied Mechanics and Engineering* 318 (2017), pp. 701–723. DOI: <http://dx.doi.org/10.1016/j.cma.2017.02.009>.
- [14] Roy R. Craig and Mervyn C. Bampton. "Coupling of Substructures for Dynamic Analysis." In: *AIAA Journal* 6.7 (1968), pp. 1313–1319.
- [15] C. Czarnota, K. Kowalczyk-Gajewska, A. Salahouelhadj, M. Martiny, and S. Mercier. "Modeling of the cyclic behavior of elastic-viscoplastic composites by the additive tangent Mori-Tanaka approach and validation by finite element calculations." In: *International Journal of Solids and Structures* 56-57 (2015), pp. 96–117.
- [16] F. Daghia, S. de Miranda, and F. Ubertini. "Patch based recovery in finite element elastoplastic analysis." In: *Computational Mechanics* 52 (2013), pp. 827–836.
- [17] G.J. Dvorak. "Transformation field analysis of inelastic composite materials." In: *Proceedings of the Royal Society of London A* 437 (1992), pp. 311–327.
- [18] G.J. Dvorak and A. Bahei-El-Din. "Inelastic composite materials: transformation field analysis and experiments." In: *In: Suquet, P. (Ed.), Continuum Micromechanics, CISM Course and Lecture* 377 (1997), pp. 1–59.
- [19] G.J. Dvorak, Y.A. Bahei-El-Din, and A.M. Wafa. "Implementation of the transformation field analysis for inelastic composite materials." In: *Computational Mechanics* 14 (1994), pp. 201–228.
- [20] J. D. Eshelby. "The determination of the elastic field of an ellipsoidal inclusion, and related problems." In: *Proc. R. Soc. Lond. A* 241 (1957), pp. 376–396.
- [21] F. Feyel. "Multiscale FE² elastoviscoplastic analysis of composite structures." In: *Computational Material Science* 16 (1999), pp. 344–354.

- [22] F. Feyel and J.L. Chaboche. "FE² multiscale approach for modelling the elastoviscoplastic behaviour of long fiber SiC/Ti composite materials." In: *Comput. Methods Appl. Mech. Eng.* 183 (2000), pp. 309–330.
- [23] Frédéric Feyel. "A multilevel finite element method (FE²) to describe the response of highly non-linear structures using generalized continua." In: *Computer Methods in Applied Mechanics and Engineering* 192.28 (2003). Multiscale Computational Mechanics for Materials and Structures, pp. 3233–3244. ISSN: 0045-7825. DOI: [https://doi.org/10.1016/S0045-7825\(03\)00348-7](https://doi.org/10.1016/S0045-7825(03)00348-7). URL: <http://www.sciencedirect.com/science/article/pii/S0045782503003487>.
- [24] P. Franciosi and S. Berbenni. "Heterogeneous crystal and polycrystal plasticity modeling from transformation field analysis within a regularized Schmid law." In: *Journal of Mechanics and Physics of Solids* 55 (2007), pp. 2265–2299.
- [25] P. Franciosi and S. Berbenni. "Multi-laminate plastic-strain organization for nonuniform TFA modeling of poly-crystal regularized plastic flow." In: *International Journal of Plasticity* 24 (2008), pp. 1549–1580.
- [26] F. Fritzen and T. Böhlke. "Three-dimensional finite element implementation of the nonuniform transformation field analysis." In: *International Journal for Numerical Methods in Engineering* 278 (2010), pp. 186–217.
- [27] F. Fritzen and T. Böhlke. "Nonuniform transformation field analysis of materials with morphological anisotropy." In: *Composites Science and Technology* 71 (2011), pp. 433–442.
- [28] F. Fritzen, M. Hodapp, and M. Leuschner. "GPU accelerated computational homogenization based on a variational approach in a reduced basis framework." In: *Computer Methods in Applied Mechanics and Engineering* 278 (2014), pp. 186–217.
- [29] F. Fritzen and M. Leuschner. "Reduced basis hybrid computational homogenization based on a mixed incremental formulation." In: *Computer Methods in Applied Mechanics and Engineering* 260 (2013), pp. 143–154.
- [30] F. Fritzen, S. Marfia, and V. Sepe. "Reduced order modeling in nonlinear homogenization: A comparative study." In: *Computers and Structures* 157 (2015), pp. 114–131.
- [31] Felix Fritzen and Max Hodapp. "The Finite Element Square Reduced (FE^{2R}) method with GPU acceleration: towards three-dimensional two-scale simulations." In: *International Journal for Numerical Methods in Engineering* 107.10 (2016), pp. 853–881. ISSN: 1097-0207. DOI: [10.1002/nme.5188](https://doi.org/10.1002/nme.5188).

- [32] R.M. Guedes, ed. *Creep and Fatigue in Polymer Matrix Composites*. Woodhead Publishing, 2011.
- [33] Robert J. Guyan. "Reduction of Stiffness and Mass Matrices." In: *AIAA Journal* 3.2 (1965), p. 380.
- [34] Z. Hashin. "Analysis of Composite Materials - A Survey." In: *Journal of Applied Mechanics* 50 (1983), pp. 481–505.
- [35] Z. Hashin and S. Shtrikman. "A variational approach to the theory of the elastic behavior of polycrystals." In: *Journal of the Mechanics and Physics of Solids* 10 (1963), pp. 343–352.
- [36] R. Hill. "The elastic behaviour of a crystalline aggregate." In: *Proc Phys Soc A* 65 (1952), pp. 349–354.
- [37] R. Hill. "Elastic properties of reinforced solids: some theoretical principles." In: *J. Mech. Phys. Solids* 11 (1963), pp. 357–372.
- [38] R. Hill. "A self-consistent mechanics of composite materials." In: *J. Mech. Phys. Solids* 13 (1965), pp. 227–240.
- [39] R. Hill. "The essential structure of constitutive laws for metal composites and polycrystals." In: *J. Mech. Phys. Solids* 15 (1967), pp. 19–95.
- [40] T. Jiang, J.F. Shao, and W.Y. Xu. "A micromechanical analysis of elastoplastic behavior of porous materials." In: *Mechanics Research Communications* 38 (2011), pp. 437–442.
- [41] D. Klusemann and B. Svendsen. "Homogenization methods for multi-phase elastic composites: Comparisons and benchmarks." In: *Technische Mechanik* 30 (2010), pp. 374–386.
- [42] N. Lahellec and P. Suquet. "On the effective behavior of nonlinear inelastic composites: I. Incremental variational principles." In: *Journal of the Mechanics and Physics of Solids* 55.8 (2007), pp. 1932–1963.
- [43] N. Lahellec and P. Suquet. "Effective response and field statistics in elasto-plastic and elasto-viscoplastic composites under radial and non-radial loadings." In: *International Journal of Plasticity* 42 (2013), pp. 1–30.
- [44] C. MAREAU and S. BERBENNI. "An affine formulation for the self-consistent modeling of elasto-viscoplastic heterogeneous materials based on the translated field method." In: *International Journal of Plasticity* 64 (2015), pp. 134–150.
- [45] S. Marfia and E. Sacco. "Micromechanics and Homogenization of SMA-Wire-Reinforced Materials." In: *Journal of Applied Mechanics* 72 (2005), pp. 259–268.
- [46] S. Marfia and E. Sacco. "Multiscale damage contact-friction model for periodic masonry walls." In: *Computer Methods in Applied Mechanics and Engineering* 205-208 (2012), pp. 189–203.

- [47] J.C. Michel and P. Suquet. "Nonuniform transformation field analysis." In: *International Journal of Solids and Structures* 40 (2003), pp. 6937–6955.
- [48] J.C. Michel and P. Suquet. "Computational analysis of nonlinear composite structures using the nonuniform transformation field analysis." In: *Computer Methods in Applied Mechanics and Engineering* 193 (2004), pp. 5477–5502.
- [49] T. Mori and K. Tanaka. "Average stress in matrix and average elastic energy of materials with misfitting inclusions." In: *Acta Metall.* 21 (1973), pp. 571–574.
- [50] T. Nakamura and S. Suresh. "Effects of thermal residual stresses and fiber packing on deformation of metal-matrix composites." In: *Acta Metallurgica et Materialia* 41.6 (1993), pp. 1665–1681. ISSN: 0956-7151. DOI: [https://doi.org/10.1016/0956-7151\(93\)90186-V](https://doi.org/10.1016/0956-7151(93)90186-V). URL: <http://www.sciencedirect.com/science/article/pii/095671519390186V>.
- [51] R. P. Nimmer, R.J. Bankert, E.S. Russell, Smith G.A., and P.K. Wright. "Micromechanical Modeling of Fiber/Matrix Interface Effects in Transversely Loaded SiC/Ti-6-4 Metal Matrix Composites." In: *Journal of Composites Technology and Research* 13.1 (1991), pp. 3–13.
- [52] J. Osher and F. Mücklich. *Statistical Analysis of Microstructures in Materials Science*. Wiley, 2000.
- [53] D. Peric. "On a class of constitutive equations in viscoplasticity: formulation and computational issues." In: *International Journal for Numerical Methods in Engineering* 36 (1993), pp. 1365–1393.
- [54] P. Perzyna. "Fundamental problems in viscoplasticity." In: *Advances in Applied Mechanics* 9.1 (1968), pp. 243–377.
- [55] O. Pierard, C. Friebel, and I. Doghri. "Mean-field homogenization of multi-phase thermo-elastic composites: a general framework and its validation." In: *Composites Science and Technology* 64.10 (2004), pp. 1587–1603. ISSN: 0266-3538. DOI: <https://doi.org/10.1016/j.compscitech.2003.11.009>. URL: <http://www.sciencedirect.com/science/article/pii/S0266353803004494>.
- [56] P. Ponte-Castañeda. "New variational principles in plasticity and their application to composite materials." In: *Journal of the Mechanics and Physics of Solids* 40.8 (1992), pp. 1757–1788.
- [57] Alfio Quarteroni, Andrea Manzoni, and Federico Negri. *Reduced Basis Methods for Partial Differential Equations: An Introduction*. La matematica per il 3 + 2, vol. 92. Springer, 2016. ISBN: 978-3-319-15431-2. DOI: [10.1007/978-3-319-15431-2](https://doi.org/10.1007/978-3-319-15431-2).
- [58] A. Reuss. "Berechnung der Fließgrenze von Mischkristallen auf Grund der Plastizität Bedingung für Einkristalle." In: *Z Angew Math Mech* 9 (1929), pp. 49–58.

- [59] S. Roussette, J.C. Michel, and P. Suquet. "Nonuniform transformation field analysis of elastic-viscoplastic composites." In: *Composites Science and Technology* 69 (2009), pp. 22–27.
- [60] E. Sacco. "A nonlinear homogenization procedure for periodic masonry." In: *European Journal of Mechanics, A/Solids* 28 (2009), pp. 209–222.
- [61] V. Sepe, S. Marfia, and E. Sacco. "A nonuniform TFA homogenization technique based on piecewise interpolation functions of the inelastic field." In: *International Journal of Solids and Structures* 50 (2013), pp. 725–742.
- [62] J.C. Simo and T. J. R. Hughes. *Computational inelasticity*. engl. Corr. 2. print. Springer, 2000. ISBN: 0-387-97520-9.
- [63] E.A. de Souza Neto, D. Perić, and D.R.J. Owen. *Computational Methods For Plasticity: Theory and Applications*. Wiley, 2008.
- [64] P. Suquet. *Plasticité et Homogénéisation*. Université Pierre et Marie Curie.
- [65] P. Suquet. "Effective behavior of non linear composites." In: *In: Suquet, P. (Ed.), Continuum Micromechanics, CISM course and lecture 377* (1997), pp. 220–259.
- [66] C.C. Swan. "Techniques for stress- and strain-controlled homogenization of inelastic periodic composites." In: *Comput. Methods Appl. Mech. Engrg* 117 (1993), pp. 249–267.
- [67] F. Ubertini. "Patch recovery based on complementary energy." In: *International Journal for Numerical Methods in Engineering* 59 (2004), pp. 1501–1538.
- [68] W. Voigt. "Über die Beziehung zwischen den beiden Elastizitätskonstanten isotroper Körper." In: *Wied Ann* 38 (1929), pp. 573–587.
- [69] L.J. Walpole. "On bounds for the overall elastic moduli of inhomogeneous systems—II." In: *Journal of the Mechanics and Physics of Solids* 14.5 (1966), pp. 289–301. ISSN: 0022-5096. DOI: [10.1016/0022-5096\(66\)90025-1](https://doi.org/10.1016/0022-5096(66)90025-1). URL: <http://www.sciencedirect.com/science/article/pii/0022509666900251>.
- [70] J.R. Willis. "Average stress in matrix and average elastic energy of materials with misfitting inclusions." In: *Acta Metall.* 25 (1977), pp. 185–202.
- [71] Hashin Z. and Shtrikman S. "A variational approach to the theory of the elastic behaviour of polycrystals." In: *J Mech Phys Solids* 10 (1962), pp. 343–352.
- [72] Hashin Z. and Shtrikman S. "On some variational principles in anisotropic and nonhomogeneous elasticity." In: *J Mech Phys Solids* 10 (1962), pp. 335–342.